2010

# Numerical and Experimental Studies on Transport Phenomena of Proton Exchange Membrance Fuel Cells.

Anh Le Dinh
*University of Windsor*

# NUMERICAL AND EXPERIMENTAL STUDIES ON TRANSPORT PHENOMENA OF PROTON EXCHANGE MEMBRANE FUEL CELLS

by

**ANH DINH LE**

A Dissertation
Submitted to the Faculty of Graduate Studies
through Mechanical, Automotive and Materials Engineering
in Partial Fulfilment of the Requirements for
the Degree of Doctor of Philosophy at the
University of Windsor

Windsor, Ontario, Canada
2010

**NUMERICAL AND EXPERIMENTAL STUDIES ON TRANSPORT PHENOMENA OF PROTON EXCHANGE MEMBRANE FUEL CELLS**

by

**ANH DINH LE**

APPROVED BY:

---

E. Croiset, External Examiner
Chemical Engineering, University of Waterloo

---

C. Chen
Electrical and Computer Engineering

---

D. Ting
Mechanical, Automotive and Materials Engineering

---

N. Zamani
Mechanical, Automotive and Materials Engineering

---

B. Zhou, Advisor
Mechanical, Automotive and Materials Engineering

---

M. Sid-Ahmed, Chair of Defense, Chair of Defense
Electrical and Computer Engineering

January, 2010

# Author's Declaration of Originality

I hereby certify that I am the sole author of this dissertation and that no part of this dissertation has been published or submitted for publication.

I certify that, to the best of my knowledge, my dissertation does not infringe upon anyone's copyright nor violate any proprietary rights and that any ideas, techniques, quotations, or any other material from the work of other people included in my dissertation, published or otherwise, are fully acknowledged in accordance with the standard referencing practices. Furthermore, to the extent that I have included copyrighted material that surpasses the bounds of fair dealing within the meaning of the Canada Copyright Act, I certify that I have obtained a written permission from the copyright owner(s) to include such material(s) in my dissertation and have included copies of such copyright clearances to my appendix.

I declare that this is a true copy of my dissertation, including any final revisions, as approved by my dissertation committee and the Graduate Studies office, and that this dissertation has not been submitted for a higher degree to any other University or Institution.

# Abstract

This dissertation presents a novel numerical approach to investigate the water management that is a critical issue in high-performance PEM fuel cell design and optimization. By incorporating the phase change and VOF method to investigate the liquid water transport, a general, three-dimensional, unsteady, multi-phase numerical model has been developed to simulate and examine the fluid flow, heat and mass transfer, species transport, electrochemical reaction, and current density distribution as well as to numerically visualize a real-time operation of a PEMFC. Several topics regarding to single fuel cell and fuel cell stack modeling, numerical and experimental visualization of liquid transport in the PEMFC, and model validation are explored in this study:

Firstly, the development of a general model of proton exchange membrane fuel cell (PEMFC) is presented. The incorporation of VOF method and fuel cell mathematical model is to investigate liquid water transport in PEMFCs by performing the formation and motion of liquid water in terms of volume-of-fluid. The general model was implemented into the commercial computational fluid dynamics (CFD) software package FLUENT®v6.3, with its user-defined functions (UDFs) written in C language in our own.

Secondly, application of the general model concretized in three specific cases including a single PEMFC with interdigitated channel, a single PEMFC with serpentine channel and a PEMFC stack is discussed. In the interdigitated PEMFC case, the numerical results show several effects of flooding on the fuel cell performance: the presence of liquid water blocks the gas transport in the fuel cell, resulting in a degradation of local current density. Those will severely affect the cell performance, especially when the flooding is significant. In addition, in the serpentine PEMFC case, the possibility of this numerical model approach demonstrates that the formation, motion and removal of liquid water in the channels and porous media can be numerically visualized in a real-time operation. In the fuel cell stack case, by adding liquid water droplets in different single cells in the stack to simulate the flooding phenomenon, the numerical results explain how liquid drops influence physical and transport characteristics of each single cell in the stack and how performance of each single cell impacts on the stack performance.

Finally, an experimental visualization on liquid droplet motion in a PEMFC channel is described. By employing direct optical visualization method into a transparent serpentine-channel fuel cell, the experimental data quantitatively and qualitatively show a good agreement with the numerical results obtained from the VOF model. Again, the success in the model comparison proves the confidence and applicability of the numerical model proposed in this dissertation.

# Dedication

To my parents, my wife and my dear daughter

# Acknowledgements

I would like to express my sincere gratitude to my supervisor, Professor Biao Zhou, who gave me this great opportunity to study in his research group, advised me throughout my time at the University of Windsor, constantly supported funding for my research. I am deeply grateful for his encouragement, motivation, efforts as well as his constructive suggestions and patient guidance throughout this work. Besides of being an excellent supervisor, he also provided me a lot of help to my personal issues, gave me valuable lessons about experience of life and facilitated my research and study.

I would like to extend my thanks to Professor Eric Croiset, Professor Chunhong Chen, Professor David S. K. Ting and Professor Nader Zamani for serving in my dissertation committee. I highly appreciate their time and effort as well as their insightful comments to provide detailed review and constructive criticism during the preparation of this dissertation.

I specially thank all my friends among faculty, staff, and students at the University of Windsor. It has been an honor to work in the department's friendly, supportive, and cooperative environment.

I am delighted to thank all my Vietnamese friends living in Windsor and studying at the University of Windsor, who give great supports to my family and stay around me outside working hours.

I would like to thank Professor Vu Duy Quang, Professor Ngo Sy Loc and Professor Le Quang in the Department of Technical Fluid and Aeronautical Engineering, Hanoi University of Technology, who led me towards a professional career and encouraged me to pursuit PhD degree at the University of Windsor.

Thanks to my sisters and especially to my parents, Professor Le Dinh Quang and Nguyen Thi Son, for their tireless dedication, physical care and spiritual support throughout my life.

At last but not least, I am also in debt to my loving wife Hoai who supports me with all her love, devotion, patience and consistent confidence in me. She has always looked after my family, shared weal and woe with me and taken care of my child while her husband glued with his computer and research papers. Finally, I would like to thank very much to my little girl Emily who has made my life so happy and joyful just by being her.

# Contents

# List of Figures

# List of Tables

# Nomenclature

| Latin symbol | Description | Units |
|---|---|---|
| a | Water activity | dimensionless |
| $A_{surf}$ | Active surface area | $m^2$ |
| $A_s$ | Heat transfer surface area | $m^2$ |
| $c_p$ | Specific heat capacity | J $kg^{-1}$ $K^{-1}$ |
| $C_i$ | Concentration of species i | kmol $m^{-3}$ |
| $D_i$ | Diffusion coefficient of species i in gas mixture | $m^2$ $s^{-1}$ |
| F | Faraday constant, $9.6487 \times 10^7$ | C $kmol^{-1}$ |
| g | Gravitational acceleration, 9.81 | m $s^{-2}$ |
| h | Convective heat transfer | W $m^{-2}$ $K^{-1}$ |
| $h_L$ | Enthalpy of formation of water vapor | N m $K^{-1}$ |
| I | Current density | A $m^2$ |
| J | Mass flux | kg $m^{-2}$ $s^{-1}$ |
| $k_{eff}$ | Effective thermal conductivity | W $m^{-1}$ $K^{-1}$ |
| $M_i$ | Molecular weight of species i | kg $kmol^{-1}$ |
| $n_d$ | Electro-osmotic drag coefficient | dimensionless |
| $n_f$ | Charge number of the sulfonic acid ion | dimensionless |
| P | Pressure | N $m^{-2}$ |
| $P_i$ | Partial pressure of species i | N $m^{-2}$ |
| $\dot{Q}$ | Heat rate | J $s^{-1}$ |
| R | Volumetric current density | A $m^{-3}$ |
| S | Source term of governing equations | |
| t | time | s |
| T | Temperature | K |
| u, v, w | Velocity components in x, y, and z directions | m $s^{-1}$ |
| $V_{oc}$ | Open-circuit potential | V |
| $V_{cell}$ | Cell potential | V |
| V | Volume | $m^{-3}$ |

| | | |
|---|---|---|
| $X_i$ | Mole fraction of species i | dimensionless |
| $Y_i$ | Mass fraction of species i | dimensionless |

| **Greek symbol** | **Description** | **Units** |
|---|---|---|
| $\alpha$ | Transfer coefficient | dimensionless |
| $\beta$ | The factor accounts for energy release | dimensionless |
| $\gamma$ | Concentration dependence | dimensionless |
| $\gamma_p$, $\gamma_T$ | Exponent factors | dimensionless |
| $\varepsilon$ | Porosity | dimensionless |
| $\eta$ | Overpotential | V |
| $\theta_w$ | Contact angle | $\circ$ |
| $\kappa$ | Surface curvature | $m^{-1}$ |
| $\lambda$ | Water content | dimensionless |
| $\mu$ | Dynamic viscosity | kg $m^{-1}$ $s^{-1}$ |
| $\rho$ | Density of gas mixture | kg $m^{-3}$ |
| $\rho_i$ | Density of species i | kg $m^{-3}$ |
| $\sigma$ | Phase conductivity | $\Omega^{-1}$ $m^{-1}$ |
| $\tau_g$ | Gaseous permeability | $m^2$ |
| $\tau_p$ | Hydraulic permeability | $m^2$ |
| $\tau_\phi$ | Electrokinetic permeability | $m^2$ |
| $\upsilon$ | Reaction rate | kmol $m^2$ $s^{-1}$ |
| $\phi$ | Phase potential | V |
| $\chi$ | Surface tension coefficient | N $m^{-1}$ |
| $\omega$ | Excess coefficient | Dimensionless |

| **Subscript** | **Description** |
|---|---|
| *an* | Anode |
| *cat* | Cathode |
| *cond* | Condensation |
| *e* | Electrochemical reaction |
| *eff* | Effective |
| *evap* | Evaporation |
| *g* | Gas phase |
| *i* | Species i |
| *in* | Inlet |
| *l* | Liquid phase |
| *m* | Membrane phase |
| *out* | Outlet |
| *ref* | Reference |

| | |
|---|---|
| *s* | Solid phase |
| *sat* | Saturated |
| *w* | Water vapor |

| **Abbreviation** | **Description** |
|---|---|
| CL | Catalyst layer |
| CFD | Computational Fluid Dynamic |
| DOE | US Department of Energy |
| GDL | Gas Diffusion Layer |
| $M^2$ | Multiphase Mixture |
| MEA | Membrane Electrode Assembly |
| MRI | Magnetic Resonance Imaging |
| PEM | Proton Exchange Membrane |
| PEMFC | Proton Exchange Membrane Fuel Cell |
| R&D | Research and Development |
| VOF | Volume of Fluid |

# Chapter 1

# Introduction

## 1.1 General introduction to hydrogen energy

World energy demand in 2006 was reported to be 472 quadrillions Btu and it will increase up to 508 quadrillions Btu in 2010 (DOE/EIA 2009 [1]). The US Department of Energy (DOE) predicts that total demand will reach 678 quadrillions Btu by 2030, a further 43.6% increase compared with the energy demand in 2005. Currently, fossil fuels including liquid fuels and other petroleum, natural gas, and coal supplied the largest share and are expected to continue supplying much of the energy used worldwide. World use of liquids and other petroleum will grow from 85 million barrels per day in 2006 to 91 million barrels per day in 2015 and 107 million barrels per day in 2030 [1]. Meanwhile, the projected average world oil prices may increase each year between 2006 and 2030. The oil price reached $70 per barrel (2007 US dollars per barrel) in 2006 and it will reach $130 per barrel in 2030 as projected in IEO 2009 [1].

Energy security is also a major issue. Disturbances in any of the major oil-producing countries such as the countries in The Organization of the Petroleum Exporting Countries (OPEC) can increase oil prices, severely influencing economic growth and political stability. Six Persian Gulf countries including Saudi Arabia, Iran, Iraq, Kuwait, the United Arab Emirates, and Qatar and Russia hold 69% of the worlds proven oil reserves. These seven countries have 68% of the worlds proven natural gas reserves (Russia, Iran, and Qatar alone have 57%) [2]. Caspian countries including Russia, Azerbaijan, Iran, Kazakhstan and Turkmenistan oil production will achieve a peak of between 3 and 5 million barrels per day in the decade 2010 to 2020. As the global economy thrives along with the growth of oil and natural gas demands, the world will become more dependent on unstable regions or oil producing countries at risk of political instability for its oil and natural gas, resulting in increased risks of supply interruptions.

In addition to global energy demand and energy security, the environmental issue caused by the combustion of fossil fuels is also a big challenge. The burning of fossil fuels is the main source of greenhouse gases causing significant changes to the global climate system. Atmospheric concentrations of the main greenhouse gas

carbon dioxide ($CO_2$) released during the combustion of fossil fuels have increased exponentially from 280 parts per million (ppm) to just over 370 ppm since the Industrial Revolution (IPCC 2001) [2]. Moreover, the pollutants including $CO_2$, $NO_x$, $SO_2$ which are the products of energy consumption also severely influences the environment and human health such as impaired air quality, degradation of visibility, health damage, harm to sensitive forests and ecological systems.

While current energy consumption is mainly derived from the combustion of fossil fuels (from 80% to 90% [1]), the rapid increase in world energy prices in the next decades, the security energy issue, and potential effects of climate change by greenhouse gas emissions, world's interests on the development of alternatives to fossil fuels are more evident. Hydrogen energy and fuel cells have been considered as promising solutions to important problems as global energy demand and resource availability, energy security, and environmental considerations of the world in the 21$^{st}$ century. The hydrogen supply is endless and hydrogen itself is the most plentiful element in nature. Unlike primary energy sources as oil, natural gas and coal, hydrogen is an energy carrier and it must be produced from other substances such as hydrocarbons (oil, natural gas and coal) or water. Hydrogen will be produced by using both existing energy systems and renewable energy sources. Unless produced from fossil fuels like steam-reforming with emission of greenhouse gases, hydrogen produced from nuclear sources, water splitting (electrolysis) and fossil-based energy conversion systems with safe storage of $CO_2$ emissions, hydrogen is a carbon-free energy source. Moreover, since hydrogen can be produced at either large or small facilities and has a wide range of options for sources and converters in every country, it shows that the flexibility is one of the main advantages of hydrogen.

## 1.2 Basic concept, Applications and Classification of Fuel Cells

Hydrogen can be used in fuel cells to generate electricity or can be used in various combustion engines to produce useful mechanical energy. A fuel cell is a electrochemical conversion device. More evidently, fuel cells are electrochemical devices that directly convert chemical energy of fuel and oxidant to electrical energy by a process involving an essentially invariant electrode-electrolyte system. For a hydrogen/oxygen fuel cell such as Proton Exchange Membrane Fuel Cell (PEMFC), the inputs are hydrogen (fuel) and oxygen (oxidant) and the only outputs are DC power, heat and water. Electrochemical processes in fuel cells are not governed by a Carnot law and therefore high operating temperature is not necessary for achieving high efficiency. Moreover, contrary to internal combustion engines, the fuel cell efficiency is not strongly dependent on operating power. However, a fuel cell is a converter only and it can continue to operate as long as it is fed with fuel and oxidant because it does not consume materials that form an integral part of its structure.

Simplicity, quick start-up, fast response to charge of load, high efficiency and power density, no moving parts, reduced corrosion problems and especially most of all: zero emissions; make fuel cells an attractive option for a wide range of products, ranging from portable micro devices like cell phones, laptops, PDAs etc.; through mobile vehicles like commercial cars, buses, airplanes, ships and submarines; to distributed electricity and heat generators as a stationary fuel cell application. Figure 1.1 depicts the wide range of options of fuel cell sources, types and applications. Although there are many kinds of fuel cells, the basic concept and principle are quite similar. All fuel cells include two electrodes, cathode and anode and an

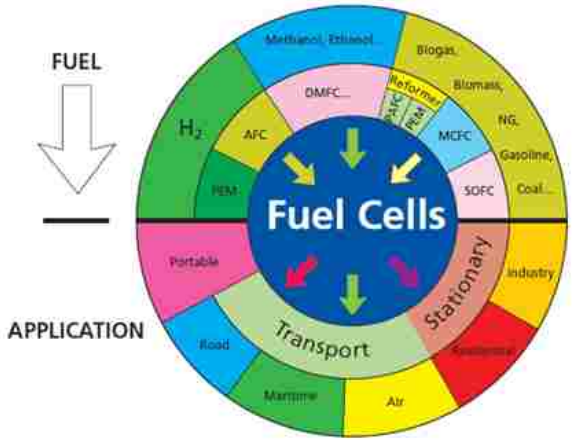


Figure 1.1: Fuel cell technologies and applications (*Source* : *EC*2003[3]).

electrolyte. The oxidation reaction takes place in the anode and the reduction reaction takes place in the cathode, while the ions transport through the electrolyte. Table 1.1 shows the main types of fuel cells with their classification, operating conditions and applications.

## 1.3 Proton Exchange Membrane Fuel Cell (PEMFC): A brief introduction

### 1.3.1 Operating description and electrochemical reactions

A PEM fuel cell consists of a positively charged electrode (anode), a negatively charged electrode (cathode) and a polymer electrolyte membrane. Hydrogen is oxidized on the anode and oxygen is reduced on the cathode. Protons are transported from the anode to the cathode through the polymer electrolyte membrane and electrons are carried to the cathode over an external circuit (current load). On the cathode, oxygen reacts with protons and electrons forming water and producing heat. Both the cathode and the anode contain a catalyst to speed up the electrochemical processes. Basic electrochemical reactions of a PEMFC are depicted in Figure 1.2 and electrochemical reactions occurring in a PEMFC are presented as in Table 1.2. Single fuel cell produces a limited voltage, usually less than one volt. In order to produce a useful voltage for practical applications, several unit cells are connected in series to form a fuel cell stack. The output voltage depends on the number of unit cells in the stack. A PEMFC stack and a unit cell are illustrated in Figure 1.3. The main advantages of the PEMFC compared to other kinds of fuel cells are compact and light-weight, high relative performance, low-temperature operation. PEMFCs can reach more than 1.3 kW/L fuel cell power density, 0.6 kW/L system power density, and 0.6 kW/kg mass specific power density [3]. Although working under low temperatures 20-90 °C, PEMFCs can start and operate in subfreezing temperature.

Table 1.1: Various types of Fuel Cells

| Fuel cell type | Electrolyte | Operating temperature (°C) | Fuel/Oxidant | Efficiency (%) | Applications |
|---|---|---|---|---|---|
| Akaline (AFC) | KOH, NaOH solution | 50 - 200 | $H_2/O_2$ | 60 - 70 | Up to 100 KW transport, space, military |
| Proton Exchange Membrane (PEMFC) | Proton Exchange Membrane | 50 - 120 | $H_2/O_2$, Air | 40 - 60 | Up to 500 KW transport, commercial applications, portable devices |
| Direct Methanol (DMFC) | Proton Exchange Membrane | 50 - 200 | $CH_3OH/O_2$, Air | 40 - 50 | Up to 10 KW transport, mobile, small, portable devices |
| Phosphoric acid (PAFC) | Phosphoric acid ($H_3PO_4$) | 170 - 210 | $H_2$, natural gas, Biogas/$O_2$, Air | 40 - 55 | Up to 10 MW power generation, co-generation |
| Molten Carbonate (MCFC) | Moltel $Na_2CO_3$, $Li_2CO_3$ $K_2CO_3$ | 600 - 700 | $H_2$, natural gas, Biogas, $H_2$ reforming gas, /$O_2$, Air | 50 - 65 | Up to 100 MW power generation, co-generation |
| Solid Oxide (SOFC) | Solid $ZrO_2$ | 650 - 1000 | $H_2$, natural gas, Biogas, $H_2$ reforming gas, /$O_2$, Air | 45 - 60 | Up to 100 MW power generation, co-generation |

Table 1.2: Fuel cell reactions

| | |
|---|---|
| Anode reaction | $H_2 \rightarrow 2H^+ + 2e^-$ |
| Cathode reaction | $^1/_2O_2 + 2H^+ + 2e^- \rightarrow H_2O$ |
| Total reaction | $H_2 + {}^1/_2O_2 \rightarrow H_2O$ |

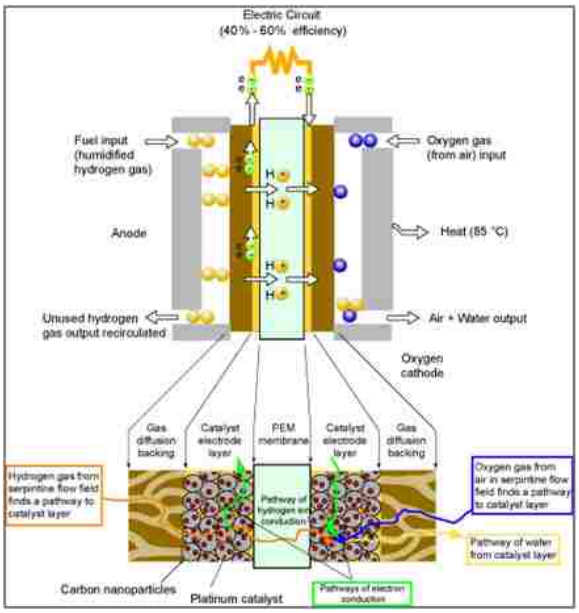


Figure 1.2: Schematic diagram of a PEMFC (Source: www.physics.nist.gov).

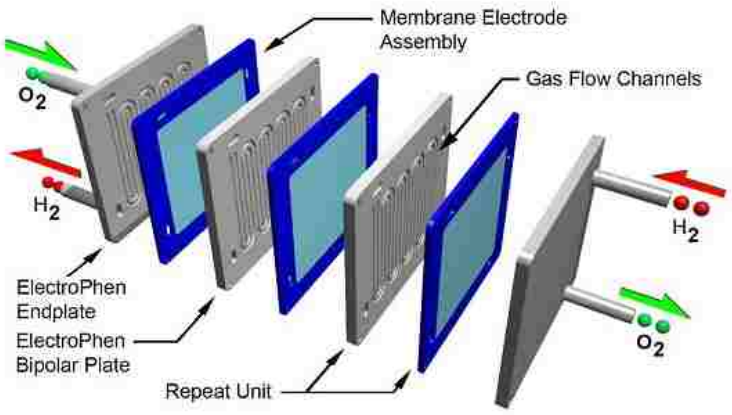


Figure 1.3: Structure of a PEMFC stack and a PEMFC unit (Source from: www.futureenergies.com).

### 1.3.2 Fuel cell materials and components

A single PEM fuel cell consists of current collectors (including gas channels), gas diffusion layers, and catalyst layers on the both anode and cathode; and proton exchange membrane shown in Figure 3.1.

***Proton Exchange Membrane (Polymer Electrolyte Membrane - PEM)***

The electrolyte membrane permits protons, but not electrons to pass through it to the cathode site, and separates hydrogen and oxygen molecules and therefore prevents direct combustion. Actually, the membrane also acts as an electronic insulator between the bipolar plates. A common theme for producing polymer electrolyte membranes is the use of sulphonated fluoro-polymers, usually Fluoroethylene. PEM consists of a polytetrafluoroethylene (PTFE) which is sulphonated aside chain is added, ending with sulphonic acid (-$HSO_3$). The acid molecules are fixed to the polymer, but the protons on these acid groups are free to migrate through the membrane. The requirements of PEMs are high proton conductivity, good electronic insulation, good separation of hydrogen in the anode side from oxygen in the cathode side, high chemical and thermal durability, and low production cost. A typical PEM is Nafion that is the most commonly used in PEMFCs. The membrane thickness ranges from 5 to 300 $\mu$m [4].

***Catalyst layers - Electrodes***

In order to speed up electrochemical reactions taking place on the electrode surfaces, the catalyst is formed into very small particles on the surface of somewhat larger particles of fine carbon powders and catalyst particles must have contact to both ionic (proton) and electronic conductors. The best catalyst material used for PEMFC electrodes is platinum (Pt). For the separate electrode method, the carbon-supported catalyst is fixed, using some techniques to a porous and conductive material such as carbon cloth or carbon paper. Porous materials are to achieve acceptable reaction rates, then the effective area of active catalyst sites must be several times higher than the geometrical area of the electrode. The catalyst layer materials are highly porous with porosity in a range of 0.4 to 0.6. The typical thickness of catalyst layers is in range of 10 to 50 $\mu$m [4].

***Gas diffusion layers (GDLs)***

In addition to supporting the mechanical structure for the electrodes, the carbon paper or cloth also is to diffuse the gas onto the catalyst and transport the water from or to the catalyst layers and so is often called the gas diffusion layer. Gas diffusion layers provide electrical contact between the electrodes and the bipolar plates and distribute reactants to the electrodes. They also allow reaction product water to exit the electrode surface and permit passage of water between the electrodes and the flow channels. GDLs are also to provide heat transport from the catalyst layer to the bipolar plates. To facilitate such requirements, GDLs are usually made of porous materials such as carbon paper or carbon cloth, and about 100 to 300 $\mu$m thick [4], as is used in the separate electrodes. GDLs can be coated with Teflon to reduce flooding which can inhibit the gas transport, severely affecting the fuel cell performance.

***Current collectors (bipolar plates)***

In a fuel cell stack, bipolar plates separate the reactant gases of adjacent cells and individual cells in the stack, connect the cells electrically, distribute the reactant gases to the GDLs, carry by-product water away from the cells, provide the cooling channels and act as a support structure. Bipolar plates have reactant flow

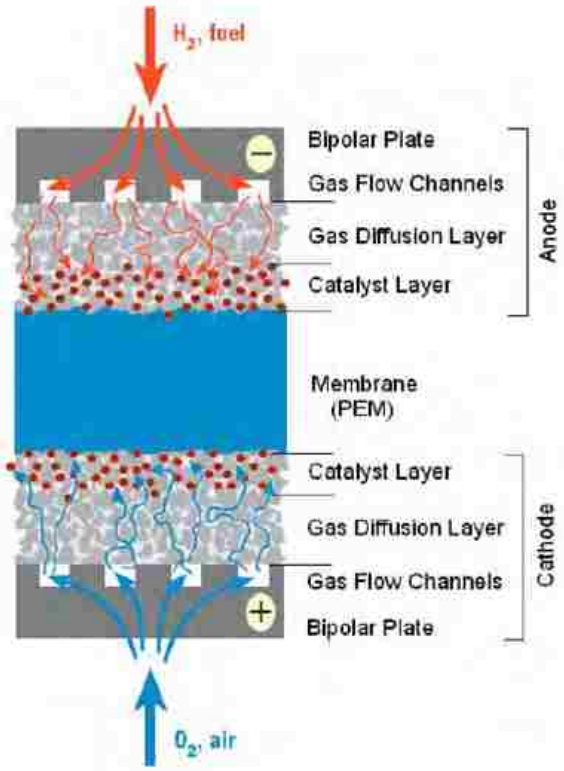


Figure 1.4: PEMFC components (*Source from book* : *Fuel Cell Research Trends*[4]).

channels on both sides, forming the anode and the cathode compartments of the unit cells on the opposing sides of the bipolar plate. In a unit cell, separate plates have flow channels only on one side. Flow channel geometry has an effect on reactant flow velocities and mass transfer and thus on fuel cell performance. Bipolar plate materials might be high electric and thermal conductivity, easy to fabricate and impermeability to gases. Besides, the material should be high corrosion resistant and chemically inert. For most applications, light weight and high strength are also important. Most of PEM fuel cell bipolar plates are made of graphite, but stainless steel and composite materials have also been used.

## 1.4 Water management – A critical issue for the performance of a PEMFC

Fuel cell performance is evaluated by the relationship between the cell voltage and current density. The voltage loss is mainly caused by the activation loss due to electrochemical reactions, the Ohmic loss due to resistance and fuel crossover and the mass transport loss due to limitation of gas transport inside the cell [5]. During fuel cell operation, by-product water is generated in the cathode catalyst layer in the form of liquid,

leading to a gas-liquid flow in the porous media and the channels. On the other hand, due to the low operating temperature of PEMFCs ($30 - 100\ ^{\circ}C$), excessive humidification could result in water vapor condensation. Liquid water could subsequently block the gas flow channels, resulting in a lower air flow rate on the cathode side and more severely, it hinders the mass transport of reactant gas in the GDLs and catalyst layer. These lead to an increase of voltage loss due to mass transport, thus decreasing fuel cell performance. In contrary, due to the special chemical structure of the PEM, the membrane must be well hydrated to ensure that a sufficient amount of hydrogen ions (protons) could cross the membrane. Water content is also an important factor that affects the Ohmic resistance since it is directly proportional to the ionic conductivity of the membrane. Therefore, keeping an appropriate amount of water content in the fuel cell to avoid both membrane dehydration and water vapor condensation has been a critical issue in improving fuel cell performance. In reality, however, it is almost impossible to manage water on both the anode and cathode sides without dehydration and condensation because water vapor condensation in the gas flow channels of practical fuel cell applications is unavoidable. In addition, the presence of liquid water may severely impact lifetime durability of the fuel cell. Therefore, water management, especially liquid water management, to which many engineers and scientists have recently paid particular attention, has been a critical challenge for a high-performance fuel cell design and optimization.

## 1.5 Topic and objectives of the dissertation

The overall aim of this dissertation is to investigate the liquid water transport and behaviors in PEMFCs, to understand the liquid water effect on the performance of PEM fuel cell and to numerically simulate and experimentally visualize real-time operations of liquid water formation, motion and removal in PEMFCs. The dissertation is divided into two main parts; numerical model and experimental study, as follows

### 1.5.1 Numerical investigation on liquid water transport of Proton Exchange Membrane Fuel Cell (PEMFC)

The objective of this numerical work is to develop a general mathematical model with all detailed physics included, e.g., multi-phase with Volume-of-Fluid (VOF) interface-tracking between gas-phase and liquid-water-phase, multi-components, heat and mass transfer, electrochemical reactions, and water-phase-change effects. With the development of high performance computing and advance numerical algorithm, a general numerical model of PEMFC has been introduced to characterize more fully the physical behavior, to aid our understanding of complex phenomena occurring in a fuel cell system and to provide powerful tools for fuel cell design and optimization. This new approach is capable of investigating liquid water transport that is critical to understanding and preventing the flooding phenomenon - one of the most important issues of water management in PEMFC. This model considered all the necessary components consisting of the membrane, catalyst layers, GDLs, gas flow channels and current collectors. By using VOF algorithm, the formation, motion and removal of the liquid water are illustrated along the time in numerical simulation. The effects

of presence of liquid water on flow field and transport parameters in the channel and porous media are also discussed. This numerical model explicitly elucidate that the liquid water would hinder the gas transport in the fuel cell, resulting in a high concentration loss and directly decreasing the current density, in other words, severely affecting a single PEM fuel cell performance. Furthermore, in a PEMFC stack, the degradation of a single fuel cell in series connection due to water flooding would reduce the overall stack performance. In addition, the model suggests that the phase change of water, namely water condensation and evaporation processes, is the main mechanism for liquid water formation and flooding occurring in PEMFCs.

### 1.5.2 Experimental investigation on liquid water motion and transport in transparent PEM fuel cells

The objective of experiment work is to examine the two-phase flow inside single PEMFCs, validate the simulation results obtained from the numerical model and investigate liquid water dynamics in a real PEM fuel cell by visualization methods. Various experimental methods have been developed to track the presence of liquid water and its behavior in PEMFCs. These techniques are known such as liquid water visualization, neutron radiography or tomography, and magnetic resonance image (MRI). Our present work focuses on liquid water visualization due to its high partial and temporal resolutions and especially, easy to use. In addition, the water visualization method was demonstrated as a powerful tool to capture and visualize liquid water distribution in transparent PEMFCs. To conduct the experimental visualization in transparent PEMFCs, an experimental fuel cell system has been built. It includes a fuel cell test bench, transparent fuel cells, data acquisition systems (DAQs) and an intensified camera supported with optical lenses and light source. The experimental results can elucidate the liquid water transport in various flow conditions in PEMFC channel and be used to validate the numerical results obtained from the simulation model.

## 1.6 Outline of the dissertation

The content of this work focuses on two main parts: development of a numerical simulation model for PEMFCs and implementation of experimental visualization on liquid water transport of a transparent PEMFC. Hence, the dissertation is organized into 8 chapters that are summarized as follows

***Chapter 1***: Introduction to the Hydrogen and Fuel Cell energy. This chapter gives brief concepts in Fuel Cell technology: how Fuel Cells work, application and classification of Fuel Cells, the basic structure of PEMFCs, what important issues in fuel cell operation and application, how importantly water management affects the PEMFC performance, the aim of this dissertation and the main parts this dissertation focuses on.

***Chapter 2***: A review of different numerical models and experimental approaches are surveyed to bring out the critical look at the fuel cell research, the challenges on PEMFC simulation and experimental works, the methodologies in development of PEMFC modeling and the different model approaches that the scientists and researchers have done to the PEMFC area.

***Chapter 3***: The theoretical and mathematical descriptions of PEMFC numerical model are presented in

details. The governing equations of fluid dynamics and transport phenomena representing the conservation of mass, momentum, energy, species and charge transports are given. The constitutive equations, source terms and boundary conditions to describe overall physical and electrochemical processes are explained. This part also expresses the main idea of the model development: the combination of a general PEMFC model with VOF interface tracking algorithm. The CFD algorithm and grid dependence check are introduced at the end of this chapter.

***Chapter 4***: Once the numerical model is successfully developed in terms of mathematical equations and numerical algorithm, it is implemented in a single PEMFC with interdigitated channel design. In this part, the computational grid of a single interdigitated PEMFC is first created. Then, in the next step, liquid droplets are numerically added into the fuel cell to investigate the liquid water transport in the channel and porous media. After performing the time evolution of liquid water motion by a series of pictures obtained from the numerical results, liquid water effects on physical and transport properties and especially the fuel cell performance are explained and discussed.

***Chapter 5***: This chapter introduces the incorporation between the phase change process and VOF method to investigate the liquid water transport to simulate a real-time operation of a PEMFC. Since the presence of liquid water in the fuel cell is established by phase change equilibrium condition, the numerical results show the real-time process of a liquid water transport inside a PEMFC: from the beginning when the fuel cell operation starts, how liquid water is formed, through the stage of droplets motion, to the time when liquid water is removed from the channel outlet. Again, the effects of liquid water to the reactant gas transport are investigated. Interestingly, the mechanism of phase change is also mentioned.

***Chapter 6***: The simulation of a fuel cell stack is performed by applying the numerical model. In practice, the single fuel cells are connected in serial/parallel into the stack with high current/voltage. In this part, the performance of three single cells in the fuel cell stack is examined according to the presence of liquid water in different cells. The numerical results from the stack model are discussed to elucidate how liquid water affects the performance of each single cell in the stack and how the performance of each single cell affects the stack performance.

***Chapter 7***: This chapter describes the development of a experimental system that can be used to visualize liquid droplets motion in the transparent flow channel of a PEMFC and validate the simulation results obtained from the numerical model using VOF method that are introduced from Chapters 3 to 6. Herein, descriptions of experimental devices and setup, the experimental procedures, experimental results and numerical data validation are presented and discussed in details.

***Chapter 8***: This chapter again indicates the main purposes of this work, summarizes the significant findings, draws the conclusions, and suggests some applications of this work to Fuel Cell R&D for the future.

## 1.7 Contributions to Fuel cell Research and Development

The advantages and contributions of our numerical simulation can be summarized as follows

- Multi-phase, three-dimensional PEMFC model available with gas-liquid interface tracking.
- Multi-phase, three-dimensional PEMFC model available with electro-chemical reactions.
- Capable of locating the presence of liquid water in certain regions of the fuel cell.
- Capable of investigating the effects of liquid water on physical, electro and transport properties.
- Capable of predicting the flooding in a local micro-scale region.
- Capable of predicting phase-change process inside the fuel cell.
- Enable to numerically simulate real-time operations of liquid water.
- Can be used to validate the experimental visualization.
- Can be applied for different geometries of PEMFCs.
- Can be applied in both single and multi-stack PEMFCs.

# Chapter 2

# Literature Review

## 2.1 Review of numerical simulation

A PEM fuel cell process is very complex. It involves flow dynamics, multi-phase, multi-component species transport, heat and mass transport mechanism and electrochemical reactions that do not easily carry out detailed investigation through experiments. Especially water management and flooding phenomenon, to which many engineers and scientists have recently paid particular attention, has been a critical challenge for fuel cell modeling. Therefore, a large number of mathematical modeling and simulation models with water transport and management-related studies have been developed in the last decade and recent years for different purposes and in different ways based on numerical approaches. In this literature review, in order to systematize fuel cell models with water transport, the models and discussion are categorized by their geometric dimensionality [6].

In the early 1990s, one-dimensional (1-D) models were first introduced by Springer and co-workers [7], Bernardi and Verbrugge [8], Nguyen and White [9]. Those are isothermal, one-dimensional and steady state models and considers water transport through the complete fuel cell. Springer and co-workers focused on a variety of physical parameters and operating conditions such as species mass fractions, anode stoichiometries, temperature, membrane thickness and porosity to examine the effect of water transport on the fuel cell performance. Water diffusion coefficient, electro-osmotic drag, water sorption and membrane conductivities that are considered as a function of water content were taken into account in water transport of the fuel cell. However, the model only considers the cathode reactions and over-potential and neglects the anode over-potential since it assumed that the anode catalytic activity is very high. The Bernardi and Verbrugge model employed governing equations used to solve hydrodynamics, species transport, electrochemical reactions and gas-phase transport. The water transport in the model considered as two-phase flow including liquid and gas phases was taken account in the diffusion media and the membrane. The model calculations showed in details how the fuel cell performance is affected by cathode pressure, the membrane thickness, gas porosity and some other physical and material properties. The numerical and experimental data were also compared with a good agreement. In contrary, the main limitations of the model are that the heat transport in the fuel

cell is considered to be isothermal, the membrane is assumed to be well-hydrated and the treating of liquid water phase is unevident. To overcome the limitations of Springer model and Bernardi and Verbrugge model, Nguyen and co-workers presented a pseudo-two dimensional mathematical model that considers the heat and mass transport in the fuel cell. In Nguyen model, water transport through the membrane caused by electro-osmotic drag effect and back diffusion is described as a function of water activity in the anode flow channel and gradient of water concentration across the membrane is assumed to be linear. The model results show the influences of various operating parameters and conditions on the fuel cell performance and the changes of current density, net water flux and electro-osmotic drag coefficient along the channel for different humidification circumstances. The voltage loss, current density, water and temperature profiles along the channel were also described. Out of these models, the degrees of the flooding in the cathode diffusion layer and catalyst layers were investigated in a one-dimensional, steady state fuel cell model developed by Baschuk and Li [10]. The model results demonstrated that the overpotential of the cathode catalyst layer is increased as the oxygen concentration decreases and at the low current density, the maximum flooding will be reached as the cell pressure significantly increases. By introducing the fraction of electrode flooded, the polarization curves gained from the numerical model also show a good agreement with the experimental data from the literature. Zhou and co-workers [11] developed a one-dimensional, along-flow-channel model combined with catalyst layer model that consider the effects of pressure, temperature, anode inlet humidification, anode inlet water content and the membrane thickness on the fuel cell performance. Zhou also defines the presence of liquid water distribution along the channel by the local relative water content, water activity and relative humidity. Recently, the model of Falcao and co-workers [12] implemented a one-dimensional model incorporating heat transfer effects. Similar to previous 1-D models, the model results showed the influence of water content and net water transport coefficient on the current density. The species concentrations and temperature profiles along the cell were plotted and the polarization curve was compared with recent experimental data. On the other hand, in addition to general 1-D PEMFC models, the numerical models that considered liquid water in the porous mediums such as GDL were developed in more detail. Nam and Kaviany [13] introduced a two-phase numerical model by considering random carbon fiber mats as the GDL. Single- and two-layer diffusion mediums were both considered to investigate the effective diffusivity and water saturation. In the model, Nam and Kaviany determined the water saturation based on the description of water vapor condensation, mass diffusivities of the species, and capillary motion of the condensate in a fibrous diffusion media. They examined the effects of fiber diameter, porosity and capillary pressure on water saturation. Although the flow field, mass transport and chemical reactions in the fuel cell were not considered, the model was a pioneering study in developing and completing two-phase water transport models that came later on.

However, the main limitation of the 1-D models is that the species concentrations along the gas channels/GDLs/catalyst layers are assumed to be constant. In reality, these concentrations are variable depending on mass transport and electrochemical kinetics in the catalyst layers in which the reactions take place. More realistic than one-dimensional models, the two-dimensional models were developed after that by employing the 2-D governing equations to fuel cell modeling. One of the renowned two-dimensional models was introduced by Gurau and co-workers [14]. This model can be considered as one of the first 2-D fuel cell models that used CFD to solve the coupled continuity, momentum (Navier-Stokes), energy and species transport

equations. The model results showed the distributions of oxygen and water vapor mole fractions in two-dimensions of the cathode flow channel and GDL with different current densities. Although the liquid water transport was not given in the model, it includes the liquid water velocity distribution in the membrane. At the same time, Singh and co-workers [15] generated a 2D model that describes the liquid water transport in the electrodes by Darcys law and liquid water flow in the membrane by Schlogl equation. The effects of flow configurations, electrode porosity on the cell performance and 2-D effects on the water management were examined. The comparison of model polarization curve with experiment data was also well compared. Hsing and Futerko [16] derived a 2-D finite element- CFD approach model of coupled fluid flow, mass transport, and electrochemistry for a PEMFC. The model was used to predict the dependence of water fraction at the exit of anode flow channel on hydrogen and oxygen stoichiometries, current density and cell temperature. Again, liquid water saturation was introduced in a 2-D, multi-phase mixture model by Wang and co-workers [17]. Taking the existence of liquid water into account, the phase change was treated of water within the cathode electrode and gas channel. They developed a two-phase flow and transport model to predict the liquid water formation and its effects on the performance of the PEMFC cathode. First taken into account in a 2-D model, the pore size distribution of GDLs showed its important influence to the fuel cell performance in Liu and co-workers study [18]. As the liquid water occurring in fuel cell is set based on phase equilibrium, the partial flooding at different operating conditions are investigated. In another 2-D model, Jeng and co-workers [19] showed that the 2-D model could be used to predict the presence of liquid water in the channel. This conclusion was demonstrated with experimental verification on a 3-D transparent PEM fuel cell. Out of those studies, 2-D simulations that incorporate multi-phase mixture approach to model the two-phase flow and transport were introduced by You and Liu [20] and more recently, Baboli and Kermani [21]. In these models, the multi-phase mixture was assumed to be single fluid with different phase composition.

With state-of-art of computational resources and numerical algorithm, the three-dimensional (3-D) CFD models are capable of simulating simultaneously fluid dynamics, heat and mass transport coupled with electrochemical effects for multi-phase, multi-component flows in multiple dimensions throughout the fuel cell. 3-D models are realistic to describe detailed physical and electrochemical phenomena in practical PEMFCs. In recent years, therefore, numerous three-dimensional CFD models have been developed and adopted, especially using different commercial CFD software packages such as Fluent®, CFX®, Star-CD®, CFDRC®, FEMLAB®and COMSOL®, etc. In general, the 3-D fuel cell models can be classified into two subjects: single phase and multi-phase. The 3-D, single-phase models that take water vapor as only the gas phase in the cell into account were earlier presented. A three-dimensional numerical simulation of a straight gas flow channel in a PEMFC was performed by Dutta and co-workers [22] using Fluent code. It showed the distributions of current density and rate of water transport in the axial direction affected by various operating conditions. The later 3-D model of Dutta and co-workers [23] more introduced the mass-exchange on the Membrane Electrode Assembly (MEA) surfaces. Other fuel cell CFD model used Star-CD package was developed by Wang's group [24]. This model based on the previous model from Wang and his co-workers [25] is a non-isothermal model coupled with electrochemical transport and thus it considers the heat transport and thermal effects in a PEMFC. The water transport in a 3-D fuel cell was also discussed in another study of Um and Wang [26]. It is a significant effort since various characteristics of water transport such as equilibrium

conditions, humidification, cathode flooding were examined and the effects of flow field, membrane thickness and inlet humidified regimes on the cell performance were investigated in a three-dimension PEM fuel cell.

In fact, however, it is difficult to investigate the water management on both the anode and cathode sides without considering phase change (condensation and evaporation); this is because water vapor condensation in the gas flow channels of practical fuel cell applications is unavoidable and the flooding phenomenon in the fuel cell is mainly caused by liquid water - water in terms of liquid phase. For these reasons, the single-phase model is no longer suitable to fuel cell modeling with water transport. To model the liquid water transport more efficiently and precisely, multi-phase namely, two-phase flow models are imperative. In recent years, there have been many modeling studies that focus on two-phase flow in the fuel cell channels and porous media developed using different approaches. Usually, the multi-phase model is divided to three modeling groups: the multi-phase mixture model ($M^2$ model), the multi-fluid (two-fluid) model and the Volume-of-Fluid (VOF) model. $M^2$ model introduces the liquid water saturation as the volume fraction of liquid water and the multi-phase mixture is essentially considered as a single-phase fluid that has varying phase composition. It denotes that the mixture in $M^2$ model does not have separate phases like liquid and gas and the multi-phase flow is calculated by a mass-averaged mixture velocity. Wang and Cheng [27] are the pioneering authors who proposed the $M^2$ approach to fuel cell modeling. The later $M^2$ models had been developed by Wang and co-workers [28, 29], Mazumder and Cole [30], Ju [31]. The general idea to develop these $M^2$ models is that the two-phase channel flow is solved based on two-phase Darcys law and the two-phase transport inside the porous media is assumed to be governed by capillary effect between the liquid and gas phases. In these models, the mathematical governing equations and numerical algorithm are also solved by commercial CFD software like Fluent®6.0 [28], Fluent®6.1 [29] and CFDRC®[30].

While the $M^2$ models deal with the two-phase flow by single fluid dynamics equations with averaged properties, the two-fluid models analyze the two-phase water transport by solving a separate set of mass and momentum equations for each phase. By introducing one more equation for liquid water in terms of liquid saturation, the two-fluid model looks more realistic. Moreover, the phase transfer equilibrium between liquid and gas phases was also taken into account, describing the condensation and evaporation processes. Typical two-fluid models for two-phase transport in PEMFCs have been developed by Berning and Djilali [32], Ye and Nguyen [33], He and co-workers [34], Berning [35], Gurau and co-workers [36]. In these models, the liquid water transport through GDLs, catalyst layers, the membrane is modelled using viscous forces, gravity and capillary pressure effects. They are capable of describing the three-dimensional nature of the physical transport, and distributions of two-phase flow, pressure, temperature and species concentrations. The simulation results concluded that the presence of liquid water in GDLs is strongly determined by material properties (pore size, porosity), relative permeability and capillary pressure of the porous media. However, the calculations of saturated permeability, relative permeability, and capillary pressure in diffusion medium are various depending on different models that have different ways to calculate them. It would affect the accuracy of models' results if the approach is incorrect.

Although multi-phase mixture and multi-fluid models take into account the two-phase transport with liquid and gas phases and introduces the liquid water saturation as liquid water volume fraction, those are not capable of locating the presence of liquid water in terms of liquid droplets or water slugs locally concen-

trated, dispersed or accumulated in the channels and porous media. Thus, the formation and motion of liquid water could not be observed in micro-scale as presented in experimental investigations. In order to overcome these limitations, a powerful approach to deal with liquid water behaviors in the cathode of single PEMFCs or fuel cell stacks by incorporating volume-of-fluid (VOF) technique to track the dynamic airwater interface was developed by Zhou and co-workers [37, 38, 39, 40, 41]. The results showed that different designs of GDLs will affect the liquid water flow patterns significantly, thus influencing the performance of PEM fuel cells. The detailed flow patterns of liquid water and the droplet motion and removal were shown. Following the work of Zhou and co-workers, the two-phase flow models with VOF algorithm studying on characteristics of water liquid behavior in the flow channels and/or GDL were developed by Djilali and co-workers [42, 43, 44], Zhan and co-workers [45], Cai and co-workers [46], Golpaygan and co-workers [47]. These models, however, have not taken the electrochemical reaction, heat and mass transport and phase change processes in practical PEMFCs. It denotes that although including VOF technique to investigate the dynamic behavior of two-phase flow, these models eliminate the source to form water vapor and the phase change process that transform water vapor to liquid phase or liquid to vapor phase and further do not consider the effects of presence of liquid water on physical and electrochemical transports. With further improvements, Le and Zhou [48, 49, 50] have developed a general PEMFC model to associate the electrochemical reactions, fluid dynamics and the transport processes with VOF technique for solving the two-phase problem. The aim of the model is to understand the liquid water motion and its effects on the performance of fuel cell, thus liquid water was supplied by water injection to shorten the computing time, although the water droplet injection is somewhat arbitrary. Later studies of Le and Zhou [51] that are presented in this dissertation numerically simulate a real-time operation of liquid water formation and removal in a Proton Exchange Membrane Fuel Cell. Without injecting water liquid droplets at initial time, the transition of liquid-vapor would be investigated by applying the phase change effects into the channel and voids of porous media. Liquid water may be formed due to condensation at certain regions depending on local temperature and pressure. On the other hand, water vapor may also be formed due to evaporation if liquid water exists. Thus, the coupling of VOF method and phase change process promises an effective method to visualize transport mechanism of liquid water in a PEMFC. The characteristics of liquid water transport and its effects on flow dynamics and physical transports are elucidated. The numerical results are qualitatively validated against experimental visualization.

## 2.2 Review of experimental visualization

To date, most of the investigations on liquid water behavior in PEMFCs have been conducted in experiments by using various imaging visualization techniques [52]. The direct optical visualization technique has been used to observe the liquid water formation and transport in the channels of transparent fuel cells [53, 54, 55, 56, 57, 58] or the surface of the gas diffusion layer (GDL) [59]. The optical method is capable of operating at high time resolution modes with the time intervals that could reach milliseconds per frame and at various length scales from channel size (in mm-scale) to porous media void regions (in $\mu$m-scale). Despite the advantages mentioned above, the most significant disadvantage of the optical visualization is that

it is unable to capture the invisible water in terms of liquid and vapor phases remaining in the flow channels or inside of the porous media layers. To overcome the limitation of optical method, the neutron imaging technique has been employed in many literatures recently [60, 61, 62, 63, 64, 65, 66, 67, 68]. By using the neutron radiographs to detect the invisible water in opaque objects, this technique is very suitable for observing the transport properties of water inside the GDLs and the membrane of PEMFCs. Contrary to the optical technique, the neutron image technique has average ranges of time and spatial resolutions and it requires expensive modern equipments such as neutron sources and other experiment utilities. In addition, another technique similar to the neutron imaging is Magnetic Resonance Imaging (MRI) that can detect and visualize the liquid water under the gas channels and collector ribs of PEM fuel cells [69, 70, 71, 72]. Each method mentioned above has its advantages and disadvantages, in general, they play a significant role in understanding of water management in PEMFCs and investigating the effects of water transport on the fuel cell performance.

# Chapter 3

# Development of Numerical Model of Transport Phenomena of Proton Exchange Membrane Fuel Cells

## 3.1 Model domain and assumption

The computational domain for a single PEM fuel cell comprises nine sub-domains: anode collector, anode channel, anode GDL, anode catalyst layers, the membrane, cathode catalyst layer, cathode GDL, cathode channel and cathode collector. For a PEMFC stack model in which the single fuel cells are connected in series, the computational domain includes the domains of each single fuel cells of the stack. To reduce the number of grids for saving calculation time in a large computational domain of a serpentine PEMFC, the cooling channels are not taken into account in the computational domain. However, it is necessary to control the heat generated and accumulated inside the fuel cell due to chemical reactions and Ohmic resistance, thus the fuel cell is assumed to be cooled by a surrounding air stream whose heat transfer coefficient can be adjusted. The fluid flow in the fuel cell is assumed to be laminar since the Reynold numbers were calculated to satisfy the laminar flow condition due to milli-scale and micro-scale of the fuel cell channels and porous media. All things considered, the main assumptions in developing the model are as follows:

1. Ideal gas law was employed for gas mixture.
2. Laminar fluid flow was considered in the fuel cell.
3. The porous media including membrane, catalyst layers and GDLs were assumed to be isotropic.
4. The cooling process was controlled by forced convective heat transfer surrounding the fuel cell.

## 3.2 Governing equations

Fluid flow, heat and mass transport, electrochemical reaction and current transport processes in the PEMFC are mathematically described by a set of conservation laws for mass, momentum, energy, species transport and charges. The gas and liquid phases are considered as a two-phase mixture. In order to treat two-phase transport including liquid and gas phases, the water vapor is implemented as a gaseous species in the species transport equations and the liquid water is tracked by using volume fraction equation. For different layers and different zones, the appropriate equations are numerically solved with various source terms to have a set of solutions for physical and electrochemical parameters describing overall phenomena and characterization in the fuel cell.

### 3.2.1 Mass conservation equation

The mass (continuity) equation is expressed as follows:

$$\frac{\partial \varepsilon \rho}{\partial t} + \nabla \cdot (\varepsilon \rho \vec{v}) = S_m \tag{3.1}$$

The transient term represents the change of mass with time, the second term represents the change in mass flux, and this is also known as the convection term. The velocity and density of flow mixture including gas and liquid phases are considered as the variable and property in the continuity equation. As the VOF method that will be described in the next sections is employed, the volume fraction for different phases in the mixture would be defined. The variables and properties are shared by the phases and defined by volume-average calculation since the volume fractions of liquid phase $s_l$ and gas phase $s_g$ are known. The density in each computational cell then is given [73]

$$\rho = s_l \rho_l + s_g \rho_g \tag{3.2}$$

where $\rho$ is the mixture density, which is considered as the volume-averaged density between liquid phase density $\rho_l$ and liquid phase density $\rho_g$. By definition, the sum of volume fraction of each phase in the mixture is unity.

$$s_l + s_g = 1 \tag{3.3}$$

The mass source term $S_m$ is available only for the anode and cathode catalyst layers in which the mass generation, consumption and transport of the species take place. Other mass source terms are set to be zero due to the conservation of mass for the whole fuel cell. For the anode catalyst layer:

$$S_m = -\underbrace{\left(\frac{M_{H_2}}{2F}\right) R_{an}}_{\text{Hydrogen consumption}} \tag{3.4}$$

For the cathode catalyst layer:

$$S_m = -\underbrace{\left(\frac{M_{O_2}}{4F}\right)R_{cat}}_{\text{Oxygen consumption}} + \underbrace{\left(\frac{M_{H_2O}}{2F}\right)R_{cat}}_{\text{Water generation}} \tag{3.5}$$

For other layers:

$$S_m = 0 \tag{3.6}$$

### 3.2.2 Momentum conservation equation

A single momentum equation is solved throughout the domain and the resulting velocity field is shared between gas and liquid phases [73]

$$\frac{\partial}{\partial t}(\varepsilon\rho\vec{v}) + \nabla(\varepsilon\rho\vec{v}\vec{v}) = -\varepsilon\nabla p + \nabla[\varepsilon\mu\nabla\vec{v}] + S_v \tag{3.7}$$

In the momentum equation, the transient term represents the change of momentum with time, and the second term describes advection momentum flux. The first two terms on the right hand side of the momentum equation represent momentum impacted due to pressure and viscosity effects, respectively. The mixture properties including mixture viscosity $\mu$ are dependent on the volume fraction of each phase, defined as

$$\mu = s_l\mu_l + (1 - s_l)\mu_g \tag{3.8}$$

For the momentum equation, the gravity effect is taken into account in the source terms. In the different layers of the porous media, the other source terms are added to describe the flow of the fluid through a porous zone by using viscous loss - Darcy drag force. The use of Darcy law to represent the source terms of momentum equation in porous media is valid because the flow is laminar, viscous with very low velocity. The source terms are different for different regions of the fuel cell. In the flow channel, only gravity force is considered. Meanwhile, the viscous loss (Darcy drag force) and the surface tension force are taken into account along with gravity force in the GDLs and catalyst layers. In the membrane, the source term that accounts for the electrokinetic permeability is added.
For flow channel,

$$S_v = \underbrace{\rho\vec{g}}_{\text{Gravity force}} \tag{3.9}$$

For GDLs and void of catalyst layers,

$$S_v = \underbrace{\rho\vec{g}}_{\text{Gravity force}} - \underbrace{\frac{\mu}{\tau_g}\varepsilon^2\vec{v}}_{\text{Darcy force}} + \underbrace{\chi\kappa\frac{2\rho\nabla s_l}{(\rho_l + \rho_g)}}_{\text{Surface tension force}} \tag{3.10}$$

For the membrane,

$$S_v = \underbrace{\rho\vec{g}}_{\text{Gravityforce}} - \underbrace{\frac{\mu}{\tau_g}\varepsilon^2\vec{v}}_{\text{Darcy force}} + \underbrace{\chi\kappa\frac{2\rho\nabla s_l}{(\rho_l+\rho_g)}}_{\text{Surface tension force}} + \underbrace{\frac{\tau_\varphi}{\tau_p}c_f n_f F\nabla\varphi_m}_{\text{Electrokinetic force}} \tag{3.11}$$

where ε is porosity of the porous media and κ is permeability of the porous media (for each zone such as membrane, GDL or catalyst layer, and the values of ε and κ are different). $c_f$ is the concentration of sulfonic acid ions ($HSO_3$-) inside the membrane, $n_f$ is the charge number of the sulfonic acid ions ($HSO_3$-), $\varphi_m$ stands for the membrane phase potential, $\tau_p$ and $\tau_\varphi$ are the hydraulic and electrokinetic permeability, respectively.

### 3.2.3 Energy conservation equation

The energy balance in terms of temperature change is also presented in the numerical model. Analogous to the momentum equation solved in the multi-phase model using VOF method, the energy equation is also shared between gas and liquid phases [73, 74]

$$(\rho c_p)_{eff}\frac{\partial T}{\partial t} + (\rho c_p)_{eff}(\vec{v}\nabla T) = \nabla\left(k_{eff}\nabla T - \sum_i h_i\vec{J_i} + (\tau\cdot\vec{v})\right) + S_T \tag{3.12}$$

where $c_p$ stands for the mixture-averaged specific heat capacity, $k$ is the thermal conductivity, $h_i$ the enthalpy of ideal gases, $J_i$ is the diffusion flux of species $i$, τ is the tress tensor and T is the temperature (Kelvin). To specify these parameters in porous media, the effective properties were determined as follows [74]

$$(\rho c_p)_{eff} = \varepsilon\rho_f c_{p,f} + (1-\varepsilon)\rho_s c_{p,s} \tag{3.13}$$

$$k_{eff} = \varepsilon k_s + (1-\varepsilon)k_f \tag{3.14}$$

The first three source terms of Eq. 3.12 represent energy transfer due to heat conduction taking place in both solid and fluid zones, heat diffusion, and heat caused by viscous dissipation, respectively. In addition, other source terms would be considered including the heat from chemical reactions (only in the catalyst layers), Ohmic heat due to Ohmic resistance of solid zones, and the heat due to phase change processes (condensation/evaporation). In solid zone as the current collectors, the heat source is only due to resistance of the solid materials. In the flow channel, only phase change is considered as the source of heat transfer. In porous zone such as the GDLs and the membrane, a solid permeated by an interconnected network of voids filled with a fluid, the heat source term includes Ohmic heat and phase change heat. In catalyst layers in which the chemical reactions occur, in addition to the heat source due to Ohmic resistance and phase change,

the energy source term considers the heat released by the electrochemical reaction. For current collectors,

$$S_T = \underbrace{\frac{I^2}{\sigma_s}}_{\text{Ohmic heat}} \tag{3.15}$$

where $I$ is the current density and $\sigma_s$ is electrical conductivity of collector. For gas flow channel,

$$S_T = \underbrace{r_w h_L}_{\text{heat due to phase change}} \tag{3.16}$$

For GDLs,

$$S_T = \underbrace{\frac{I^2}{\sigma_s^{eff}}}_{\text{Ohmic heat}} + \underbrace{r_w h_L}_{\text{heat due to phase change}} \tag{3.17}$$

For the membrane,

$$S_T = \underbrace{\frac{I^2}{\sigma_m^{eff}}}_{\text{Ohmic heat}} + \underbrace{r_w h_L}_{\text{heat due to phase change}} \tag{3.18}$$

For catalyst layers,

$$S_T = \underbrace{\eta R_{an,cat}}_{\text{heat due to electrochemical reaction}} \underbrace{+ I^2 \left( \frac{1}{\sigma_s^{eff}} + \frac{1}{\sigma_m^{eff}} \right)}_{\text{Ohmic heat}} + \underbrace{r_w h_L}_{\text{heat due to phase change}} \tag{3.19}$$

where $\sigma_s^{\text{eff}}$ and $\sigma_m^{\text{eff}}$ are the effective electrical conductivity and the effective ionic conductivity of porous media, $\eta$ is the activation overpotential, $R_{an,cat}$ is the volumetric current density on the anode or cathode side depending on which sides the source term is taken into account, $r_w$ stands for phase change rate and $h_L$ is the latent heat.

### 3.2.4 Species transports equations

The conservation equations for species transport are solved in the two-phase flow by taking into account hydrogen, oxygen, water vapor and nitrogen in gas mixture. In this two-phase flow model, homogeneous gas phase chemical reactions are treated the same as a single-phase chemical reaction [73]. The reactants consumed and the products generated from the reactions are considered in the gas mixture and hence the same gas phase. Based on solving the equations, it predicts the local mass fraction of each species, $Y_i$, through the solution of a convection-diffusion equation for the $i^{th}$ species. Since the mass fraction of the species must sum to unity, the nitrogen mass fraction is determined as one minus the sum of the three solved mass fractions.

$$\frac{\partial}{\partial t}(\varepsilon \rho Y_h) + \nabla \cdot (\varepsilon \rho \vec{v} Y_h) = D_{h,m} \nabla^2 (\rho Y_h) + S_h \tag{3.20}$$

$$\frac{\partial}{\partial t}(\varepsilon\rho Y_o) + \nabla\cdot(\varepsilon\rho\vec{v}Y_o) = D_{o,m}\nabla^2(\rho Y_o) + S_o \tag{3.21}$$

$$\frac{\partial}{\partial t}(\varepsilon\rho Y_{wv}) + \nabla\cdot(\varepsilon\rho\vec{v}Y_{wv}) = D_{wv,m}\nabla^2(\rho Y_{wv}) + S_{wv} \tag{3.22}$$

where $D_{h,m}$, $D_{o,m}$, $D_{wv,m}$ are the diffusion coefficients for hydrogen, oxygen and water vapor in the mixture. In order to account for the effect of the porous media, fuel cell temperature and pressure, the modification of the diffusivity for porous regions is defined as [75]

$$D_{i,m} = \varepsilon^{1.5} D^0_{i,m}\left(\frac{P_0}{P}\right)^{\gamma_p}\left(\frac{T}{T_0}\right)^{\gamma_T} \tag{3.23}$$

where $D^0_{i,m}$ is the diffusion coefficient for species i (hydrogen, oxygen or water vapor) in the mixture at reference temperature and pressure, $\gamma_P$ and $\gamma_T$ are the exponential factors.

The source term in the species transport equation is equal to zero everywhere except in the catalyst layers where the species are consumed or generated in the electrochemical reactions. The source term used for the anode and cathode catalyst layers are various and dependent on the transfer current generated by electrochemical reactions. If the hydrogen and oxygen are always consumed in the anode and cathode sides, then the by-product water in terms of vapor is generated in the cathode. Moreover, the protons move from the anode to the cathode and also pull water molecules with their movement what is known as the electro-osmotic drag effect. Physically, the water transport rate through the Nafion membrane from anode to cathode by the electro-osmotic drag that is computed as a function of volumetric current density and the drag coefficient proposed by Springer and co-workers [7].

$$\dot{m}_{H_2O} = \frac{n_d M_{H_2O}}{F} R_{cat} \tag{3.24}$$

In Springers formulations, the drag coefficient is defined to be a function of the water content inside the polymer membrane, as follows

$$n_d = \frac{2.5}{22}\lambda \tag{3.25}$$

where $\lambda$ is the water content inside the polymer membrane, which is defined as the ratio of the number of water molecules to the number of the sulfonic acid ions. In other words, water would transfer from anode side to cathode side along with an amount of water generated in the cathode. The other source term due to phase change would also be considered in Eq. 3.22 since it stands for water vapor transport. If an amount of water transfers from water vapor to liquid water or vice versa, this amount is taken into account as the product (liquid to vapor phase) or as the consumption (vapor to liquid phase) in the source term of water vapor transport equation. For the anode catalyst layer,

$$S_{H_2} = -\underbrace{\left(\frac{M_{H_2}}{2F}\right)R_{an}}_{\text{Hydrogen consumption}} \tag{3.26}$$

$$S_{H_2O} = \underbrace{\left(\frac{n_d M_{H_2O}}{F}\right)\nabla I_m}_{\text{Water transport due to electro - osmotic drag}} - \underbrace{r_w}_{\text{Water phase change}} \tag{3.27}$$

For the cathode catalyst layer,

$$S_{O_2} = -\underbrace{\left(\frac{M_{O_2}}{4F}\right)R_{cat}}_{\text{Oxygen consumption}} \tag{3.28}$$

$$S_{H_2O} = \underbrace{\left(\frac{M_{H_2O}}{2F}\right)R_{cat}}_{\text{Water generation}} + \underbrace{\left(\frac{n_d M_{H_2O}}{F}\right)\nabla I_m}_{\text{Water transport due to electro - osmotic drag}} - \underbrace{r_w}_{\text{Water phase change}} \tag{3.29}$$

For the membrane,

$$S_{H_2O} = \underbrace{\left(\frac{n_d M_{H_2O}}{F}\right)\nabla I_m}_{\text{Water transport due to electro - osmotic drag}} - \underbrace{r_w}_{\text{Water phase change}} \tag{3.30}$$

### 3.2.5 Volume fraction equation of liquid

The tracking of the interface between the phases was accomplished by the solution of a continuity equation for the volume fraction of one of the phases for two-phase model by using VOF method

$$\frac{\partial}{\partial t}\left(\varepsilon s_l \rho_l\right) + \nabla\left(\varepsilon s_l \rho_l \vec{v}_l\right) = S_{s_l} \tag{3.31}$$

The motion of the interface between gas and liquid of different density and viscosity was defined by volume fraction of liquid water $s_l$ and volume fraction of the gaseous phase $s_g$[73]. Eq. 3.31 is employed to track the volume fluid of liquid phase and it is solved for entire domain. The volume fraction of the gas phase is automatically computed based on the relative equation Eq. 3.3. The source term of liquid volume fraction is the source of liquid water for all layers except the solid zone (the collectors) as liquid water is formed by phase change process in the fuel cell.

$$S_{s_l} = r_w \tag{3.32}$$

### 3.2.6 Conservation equations of Charge

The current transport of electrons through the solid phase and protons through the membrane phase was conducted by conservation equations of charges:

$$\nabla \cdot \left(\sigma_s \nabla \phi_s\right) = S_{es} \tag{3.33}$$

$$\nabla \cdot \left(\sigma_m \nabla \phi_m\right) = S_{em} \tag{3.34}$$

$\sigma_s$ and $\sigma_m$ are the electronic conductivity in the solid phase and ionic conductivity in the membrane phase, respectively. $\phi_s$ represents the solid phase potential and $\phi_m$ represents the membrane phase potential. The volumetric source terms $S_{es}$ and $S_{em}$ are defined as volumetric transfer currents. Theoretically, the volumetric transfer currents are driven by the activation overpotential $\eta$, which is the potential difference between solid and membrane phases [73]. The electronic conductivity of solid materials is constant depending on the material property and the protonic conductivity of Nafion membrane used in the model is calculated by using the formulation described by Springer and co-workers [7]. The source terms for the solid phase and the membrane phase represent the electron and proton generation, respectively, and are determined by Butler-Volmer equation [76]

$$R_{an} = R_{an}^{ref} \left( \frac{C_{H_2}}{C_{H_2}^{ref}} \right)^{\gamma_{an}} \left[ \exp\left( \frac{\alpha_{an,an} F \eta_{an}}{RT} \right) - \exp\left( -\frac{\alpha_{cat,an} F \eta_{cat}}{RT} \right) \right] \tag{3.35}$$

$$R_{cat} = R_{cat}^{ref} \left( \frac{C_{O_2}}{C_{O_2}^{ref}} \right)^{\gamma_{cat}} \left[ \exp\left( -\frac{\alpha_{cat,cat} F \eta_{cat}}{RT} \right) - \exp\left( \frac{\alpha_{an,cat} F \eta_{an}}{RT} \right) \right] \tag{3.36}$$

$R_{an}^{ref}$, $R_{cat}^{ref}$ are the volumetric reference exchange current density ($A/m^3$) in the anode and cathode, respectively, $F$ is the Faraday constant, $C_i$ and $C_i^{ref}$ are the species concentration and reference species concentration. $\gamma$ stands for the concentration dependence and $\alpha$ represents the exchange coefficient.

The relation between species concentration and species mass fraction is expressed as

$$C_i = \frac{Y_i \rho}{M_i} \tag{3.37}$$

The volumetric transfer current $R$ is driven by the activation overpotential $\eta$, which is the potential difference between solid and membrane phases

$$\eta = \phi_s - \phi_m - V_{ref} \tag{3.38}$$

The cell potential is the difference between the cathode and anode solid phase at the terminal collectors (two ends of the cell collectors which are connected to the external electric circuit). Following the conservation of charge, the total current of either electrons or protons coming out from the anode catalyst layer must be equal to the total current coming into the cathode catalyst layer and must be equal to the total current caused by the proton movement through the membrane

$$\int_{V_{an}} R_{an} V_{an} = \int_{V_{cat}} R_{cat} V_{cat} \tag{3.39}$$

## 3.3 transport through the membrane and its effects on the properties of porous media

### 3.3.1 Water transport through the Proton Exchange Membrane

Water is transported through the membrane by two main mechanisms: electro-osmotic drag and diffusion [76]. Because the proton movement is always from the anode to the cathode through the membrane, water molecules are pulled with the protons by a force called electro-osmotic drag. In addition, water may diffuse through the membrane due to the concentration gradient driven mechanism according to the Fick law [75]. Hence, the net water flux through the membrane results in a water balance between the electro-osmotic drag (from anode to cathode) and back diffusion (from cathode to anode) as follows

$$J_w = J_w^{os} + J_w^{diff} = n_d \frac{M_{H_2O}}{F} \vec{I} - D_{i,m} \nabla (\rho Y_i) \tag{3.40}$$

### 3.3.2 Membrane water diffusivity

The membrane water diffusivity is strongly dependent on the water amount remaining in the membrane. In Eq. 3.22, the membrane water diffusivity were experimentally measured by Motupally and co-workers [77], as follows

$$D_{w,m} = \begin{cases} 3.10 \times 10^{-3} \lambda \left(-1 + e^{0.28\lambda}\right) \exp\left(\frac{-2436}{T}\right) & 0 < \lambda \leq 3 \\ 4.17 \times 10^{-4} \left(1 + 161 e^{-\lambda}\right) \exp\left(\frac{-2436}{T}\right) & 3 < \lambda < 17 \end{cases} \tag{3.41}$$

where the water content, $\lambda$, which is defined as the ratio of the number of water molecules to the number of the sulfonic acid ions , is given by [7]

$$\begin{aligned} &\lambda = 0.043 + 17.18a - 39.85a^2 + 36a^3 \, (0 \leq a \leq 1) \\ &\lambda = 14 + 1.4\,(a-1) \, (1 \leq a \leq 3) \\ &\lambda = 16.8\,(a > 3) \end{aligned} \tag{3.42}$$

The water activity a is defined as

$$a = \frac{P_{\mathrm{w}}}{P_{sat}} + 2s_l \tag{3.43}$$

where $P_{\mathrm{w}}$ is the water vapor pressure (Pa), $P_{\mathrm{sat}}$ is the saturated pressure (Pa), which is calculated by

$$P_{sat} = 101325 * 10^{\left(-2.1794 + 0.02953*(T-273.17) - 9.1837*10^{-5}*(T-273.17)^2 + 1.4454*10^{-7}*(T-273.17)^3\right)} \tag{3.44}$$

### 3.3.3 The membrane ionic conductivity

The membrane conductivity is highly dependent on its hydration state. During the operation of PEMFCs, the net water flux direction is from the anode to the cathode, this could lead to membrane dehydration on the anode side and flooding on the cathode side with additional water from reaction production. The membrane conductivity is a function of water content in the membrane and is empirically obtained [7],

$$\sigma_m = \varepsilon\,(0.514\lambda - 0.326)\,e^{1268\left(\frac{1}{303}-\frac{1}{T}\right)} \tag{3.45}$$

## 3.4 Volume of fluid (VOF) method

For solving the two-phase transport in this model, the VOF technique was selected to track immiscible interfaces between gas mixture and liquid water phases in the channels and the voids of the porous media. The VOF method, which uses the static grid to locate the fluids, are very popular for the simulation the multi-fluid flow problems with significant changes of the interface topology. Our purpose of applying VOF technique in a PEMFC model is to track the movement of interfaces and boundaries of liquid water in a mixture flow. Then, it can explicitly investigate the water liquid transport and behavior. Following this method, each phase in two-phase flow can be introduced by a variable: volume fraction of the phase in the computational cell volume. The model also includes the effects of surface tension and wall adhesion along the interfaces between gas and liquid phases.

### 3.4.1 Essential concepts of VOF method

The essential features of VOF interface tracking method are expressed as follows [78],

- An initial fluid volume is employed to compute fluid volume fractions in each computational cell from a prescribed interface topology. The fluid interface of each cell interface will truncate the calculations of volume. Then the exact interface information is taken off but the discrete volume fraction data is replaced.
- Interfaces are tracked by evolving fluid volume in time with solution of an advection equation as a velocity field is provided from the fluid solver.
- Instead of unknown exact interface location at any time of solution, interface geometry is inferred and its location is reconstructed from local volume fraction data.
- The reconstructed interface is then used to compute the volume fluxes necessary for the convective terms in the volume evolution equation.

In this method, the volume of $m^{th}$ fluid $f_m$ is defined as:

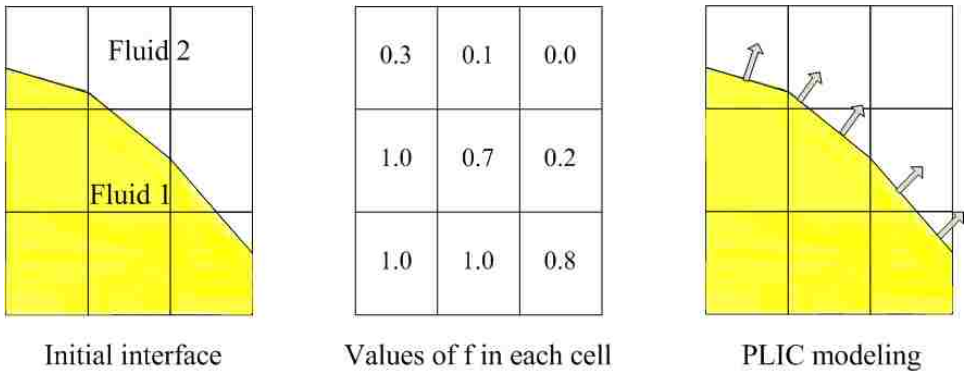


Figure 3.1: Basic concept of VOF method

- $f_m = 0$ if cell is empty (of the $m^{th}$ fluid)
- $f_m = 1$ if cell is full (of the $m^{th}$ fluid)
- $0 < f_m < 1$ if cell contains the interface between the fluids.

### 3.4.2 Interface tracking algorithm

**The Interface (Geometric) Reconstruction scheme**

As described above, it can be seen that the principle steps of VOF methods are reconstructed interface geometry and time integration algorithms. The geometric reconstruction piecewise linear interface construction (PLIC) scheme was chosen because of its accuracy and applicability for general unstructured meshes, compared to other methods such as the donoracceptor, Euler explicit, and implicit schemes [79]. Basically, a VOF geometric reconstruction scheme is divided into two parts: a reconstruction step and a propagation step. Due to the limitation of this dissertation, the interface tracking algorithm is not depicted here. More details describing this approach can be found in previous numerical studies on VOF [73, 78, 79].

**The fluid advection algorithm**

The advection algorithm consists of three steps as follows

- Step 1. Construct/reconstruct the fluid interface with planar surface.
- Step 2. Solve for the velocity field. Move the fluid volume according to the local velocity
- Step 3. Update new volume fractions values in the computational cells.

**Implementation of surface tension**

Surface tension along an interface arises as the result of attractive forces between molecules in a fluid. The net force is radially inward in a droplet and the combined effect of the radial components of forces across the entire spherical surface is to make the surface contact, thereby increasing the pressure on the concave side of the surface. At equilibrium in this situation, the opposing pressure gradient and cohesive forces balance to form spherical drops. Surface tension acts to balance the radially inward inter-molecular attractive force with the radially outward pressure gradient across the surface. The addition of surface tension to the VOF method is implemented in the source term in the momentum equation. The pressure drop across the surface depends upon the surface tension coefficient $\chi$ [73]

$$\Delta p = \chi\kappa = \chi\left(\frac{1}{R_1}+\frac{1}{R_2}\right) \tag{3.46}$$

where, $\chi$ denotes the surface tension coefficient, $\kappa$ is the surface curvature; $R_1$ and $R_2$ are the two radii, in orthogonal directions, to measure the surface curvature. The surface tension force can be written in terms of the pressure jump across the interface, which is expressed as a volumetric force F added to the momentum equation

$$\vec{F} = \chi\kappa\frac{\rho\nabla s_l}{(\rho_l+\rho_g)/2} \tag{3.47}$$

where, the term of ratio of density is used to improve the Continuum Surface Force (CSF) methods capability of modeling surface tension in the case for fine meshes at high density ratio interfaces. This method is called density-scaling of the CFS. It helps to maintain a constant interface thickness when the interface between a dense phase (namely, liquid water) and a light phase (namely, air) is tracked by using VOF algorithm [78]. The surface curvature $\kappa$ can be defined in terms of the divergence of the normal unit vector of the interface $\hat{n}$

$$\kappa = \nabla\cdot\hat{n} = \nabla\cdot(\hat{n}_{ss}\cos\theta_{ss}+\hat{t}_{ss}\sin\theta_{ss}) \tag{3.48}$$

where $\hat{n}$ is the unit vector normal to the interface between two phases near the solid surfaces, $\hat{n}_{ss}$ is the unit vector normal to the solid surfaces, $\hat{t}_{ss}$ is the unit vector tangential to the solid surfaces, and $\hat{\theta}_{ss}$ is the static contact angle at the solid surfaces. For the electrode surfaces with different wetabilities, different static contact angles could be assigned as shown in Figure 3.2, and different contact angles could result in different surface tensions, thus influencing the water transport.

## 3.5 Mass transfer Phase change process

Vapor-liquid phase change or namely, water condensation/evaporation would be considered in this model since it plays a very important role in multi-phase transport and water management of the PEMFC. Liquid water occurs in the fuel cell when the water vapor pressure reaches or over its saturated value at the cell operating temperature. In contrary, liquid water is evaporated when the water vapor pressure is smaller than its saturated value. Therefore, it could be said that the presence of liquid water would be determined by

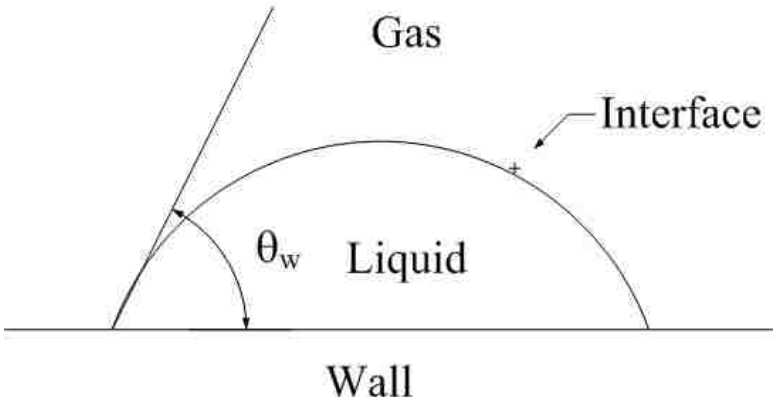


Figure 3.2: Static contact angle at the wall

vapor-liquid phase change. Physically, condensation/evaporation condition is determined by thermodynamic equilibrium $\Delta P = P_{wv} - P_{sat}$. The phase change rate is defined as follows [33]

$$r_w = \begin{cases} c_r (1 - s_l) \frac{P_{wv} - P_{sat}}{RT} M_{H_2O} & P_{wv} \geq P_{sat} \\ -c_r s_l \rho_l & P_{wv} < P_{sat} \end{cases} \tag{3.49}$$

In Eq. 3.49, the phase change rate is positive as the phase change is condensation and the phase change rate is negative as evaporation occurs. The phase change rate also plays an important role in determining the mass and energy transfers in PEMFC since it appears in the source terms of mass, species and energy equations.

## 3.6 Boundary conditions

To close the equation system including conservation equations of continuity, momentum, energy, species, volume fraction and charge with unknowns: $\rho$, $u$, $v$, $w$, $p$, $T$, $Y_i$, $s_l$ and $\phi$, some physical conditions are required to apply on external boundaries of the fuel cell domain. The boundary conditions are applied to both internal interfaces between various layers and external walls. In this study, the unified-domain approach is employed thus it is not necessary to declare the internal boundary conditions. However, the external boundary conditions for the single fuel cell and fuel cell stack models have to be prescribed.

### 3.6.1 Boundary conditions for single PEM fuel cells

A single cell includes couples of channels, collectors, GDLs, catalyst layers and a membrane in between. The electric terminals are considered as the anode connector from a single anode outside wall and the cathode connector from a single cathode outside wall. Hence, the boundary conditions for a single fuel cell are given as follows,

**Inlet of flow channels**

Inlet velocities and temperatures, mass concentrations of species were set as fuel cell operating parameters. Inlet velocities can be preliminarily calculated from the inlet flow rates based on the average current density $I_{avg}$ and excess coefficient $\omega$

$$U_{H_2,in} = \omega_{H_2} M_{H_2} \frac{I_{ave} A_{surf}}{2F\rho_{H_2} A_{in}} \tag{3.50}$$

$$U_{O_2,in} = \omega_{O_2} M_{O_2} \frac{I_{ave} A_{surf}}{4F\rho_{O_2} A_{in}} \tag{3.51}$$

where, the excess coefficient is defined as the ratio of the number of total hydrogen/oxygen supplied to the number of hydrogen/oxygen consumed.

$$\omega = \frac{\sum m_{\text{i,supply}}}{m_{\text{i,consumption}}} \tag{3.52}$$

**Outlet of flow channels**

At the outlet of the flow channels, fully developed condition was assumed to be applied for the velocity and temperature fields and species concentrations

$$\frac{\partial \vec{u}}{\partial n} = 0, \frac{\partial T}{\partial n} = 0, \frac{\partial Y_i}{\partial n} = 0 \tag{3.53}$$

**The terminal collectors**

There were two terminal collectors in which the anode and cathode collectors were connected to the external electric circuit. It was necessary to determine the boundary conditions for phase potentials on these interfaces

Anode terminal

$$\phi_s = 0, \frac{\partial \phi_m}{\partial n} = 0 \tag{3.54}$$

Cathode terminal

$$\phi_s = V_{\text{cell}}, \frac{\partial \phi_m}{\partial n} = 0 \tag{3.55}$$

**External boundaries**

External boundaries are defined as all outside surfaces of PEMFC except the terminals (the outside surfaces of the current collectors where the current enters or departs from). The zero-current-flux condition was applied for the external boundaries due to no currents coming or leaving

$$\frac{\partial \varphi_s}{\partial n} = 0; \frac{\partial \varphi_m}{\partial n} = 0 \tag{3.56}$$

### 3.6.2 Boundary conditions for PEM fuel cell stacks

As mentioned above, the fuel cell stack comprises of a number of single fuel cell connected in serial. The voltage of the stack is the sum of each single fuel cell voltage. The cathode and anode channels of each fuel cell are connected to the inlet and outlet manifolds that play a role as flow distribution. Therefore, boundary conditions of the stack can be obtained from those of single PEM fuel cell except that the voltage applied in the stack terminals is the stack potential.
Anode terminal of the stack

$$\phi_s = 0 \tag{3.57}$$

Cathode terminal of the stack

$$\phi_s = V_{\text{stack}} = \sum_i V_{\text{singlecell}i} \tag{3.58}$$

### 3.6.3 Thermal condition for external boundaries

For both the single fuel cell and fuel cell stack models, the cooling channels are needed to control the temperature rising due to the heat from the reactions and Ohmic resistance of solid materials in fuel cell. To reduce the computational quantity amount and calculation time, the cooling channels were not included in this numerical model. Heat transfer, however, was assumed to take place between all outside surfaces and the ambient environment by forced convection. Inside the fuel cell, heat is produced during its operation. Heat generation rate is assumed to be a product of the total current and potential loss [80]. To ensure that the forced convection dissipates the heat converted from electricity, the following condition must be satisfied,

$$\dot{Q}_{convection} = \dot{Q}_{generated} \tag{3.59}$$

then the convective coefficient $h$ was chosen as

$$h = \frac{I(1.25 - V_{cell})}{A_s (T_{surf} - T_\infty)} \tag{3.60}$$

It should be noticed that it is necessary to have an estimated value of surface temperature, $T_{surf}$, of the fuel cell to calculate the convective heat transfer coefficient in Eq. 3.60. It was assumed in this study that the temperature difference between the fuel cell surface and the ambient is about 50 °C when estimating the convective heat transfer coefficient.

## 3.7 CFD algorithm and solution procedure of the numerical model

### 3.7.1 CFD algorithm and solution procedure

The computational domain consists of all parts of an entire fuel cell such as the membrane, GDLs, catalyst layers, flow channels and collectors. It also includes the bipolar plates and the manifolds if the modeling domain is applied on a fuel cell stack. The computational grids are implemented by using Gambit®2.3 mesh

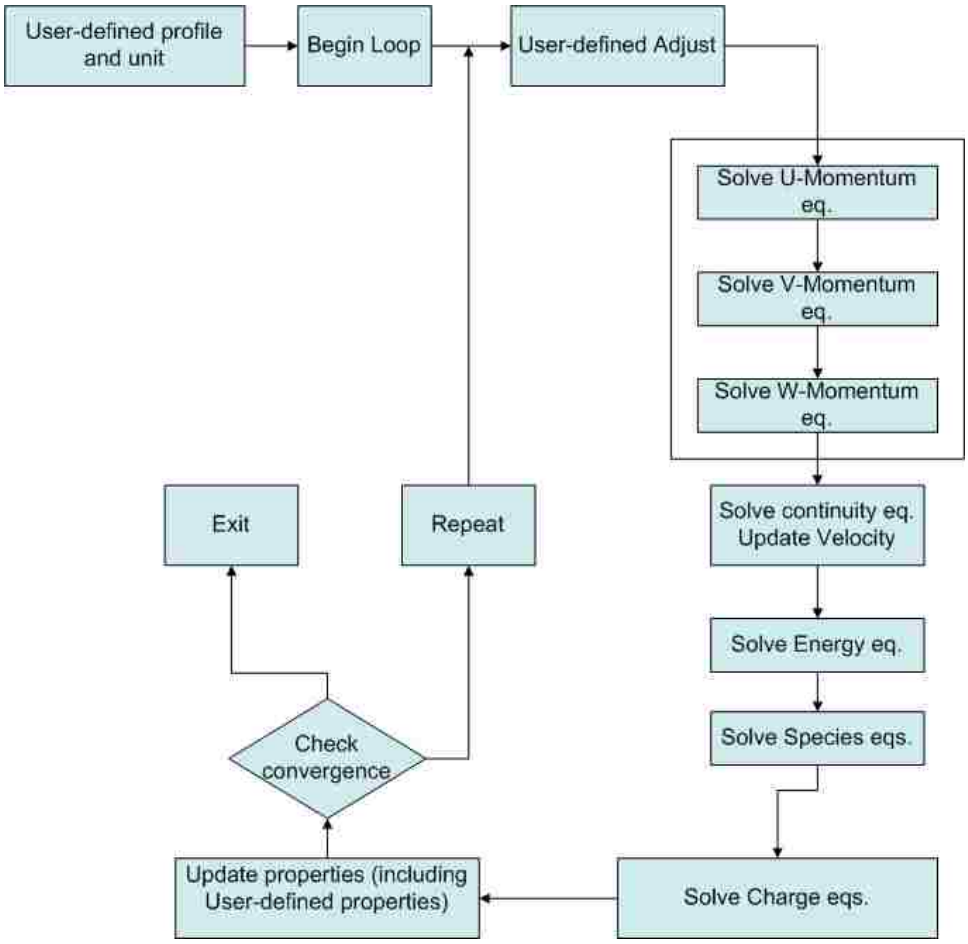


Figure 3.3: Solution Procedure for the Pressure-Based Segregated Solver

generation software. The coupled set of governing and constituent equations is descritized by Finite Volume Method (FVM) in Fluent®6.3 software [73]. The physical and material properties, source terms and boundary conditions are developed in our own User-Defined-Functions (UDFs) based on the general Fluent®6.3 environment. The developed UDFs are written in C language with about 2000 statements. The VOF algorithm was incorporated with flow field, heat transport and electrochemical reactions solver to track the gas-liquid interface. The solution procedure for Pressure-Based Segregated Solver [73] shown in Figure 3.3 incorporates with PISO algorithm [81] and the residual criteria of solved parameters are set to be smaller than $10^{-5}$.

Table 3.1: Different cases for validation of grid dependency

| Case No. | Type of channel | Geometrical dimensions of the channel (m × m × m) | Number of grid cells | Grid size in the channel (m) |
|---|---|---|---|---|
| 1 | straight | 0.001 × 0.001 ×0.006 | 378,750 | 0.00004 |
| 2 | straight | 0.001 × 0.001 ×0.006 | 42,000 | 0.0001 |
| 3 | straight | 0.001 × 0.001 ×0.006 | 9,750 | 0.0002 |

### 3.7.2 Validation of grid dependency

The size of the mesh (grid resolution) evidently affects the accuracy of numerical solution. In other words, it was said that the results are related to the resolution of the numerical grid. Therefore, grid dependency would be done to check the solution at different grid sizes and get a range of the grid size in which the solutions are reasonably independent on the size of grid. In order to validate the grid dependency in this study, a very fine mesh with high resolution was applied to a straight channel fuel cell that has dimensions of 0.001 m × 0.001 m for channel cross-section and 0.006 m length of the channel and each cell in the straight channel has the same sizes with 0.00004 m for three dimensions (Case 1 in Table 3.1). The computational domain of this mesh contains 378,750 cells. The other two coarser meshes were also generated on the same geometry of the straight channel with the number of computational cells of 42,000 (Case 2 in Table 3.1) and 9,750 (Case 3 in Table 3.1). The geometrical and grid properties of the three cases are shown in Table 3.1 and Figure 3.4. The coupling among two-phase flow dynamics, VOF interface tracking process and electrochemical reaction has been taken into account in the three cases. For solving fluid, heat, and mass transports equations coupled with VOF model and testing the possibility of tracking liquid water inside the channel, a water droplet was initially added into the channel at the time t = 0 sec. The time step used in the simulation for the three cases is $\Delta t = 10^{-6}$s. The simulation is considered to be completed when the water droplet moves out from the channel. In the three cases, the numerical results show that the motion and dynamic behavior of the water droplet can be investigated while the mass transport and electrochemical reaction are simultaneously taking place in the fuel cell. The results from these cases are quite similar in terms of the big picture of liquid water behavior. It also demonstrates that these meshes with variation of number of grid cells (grid resolution) could be reasonable for solving the model.

However, it is noticeable that the maximum grid resolution that is practically feasible is limited by the available computational resource and time, especially if a large computational domain with complex geometry that is very popular in single fuel cell and fuel cell stack simulation is employed. For this reason, the coarser meshes are usually used if the solution is good enough to resolve the physical scales of the model. Hence, the grid size used in Case 3 would be applied on simulation of the fuel cell grids used in this work.

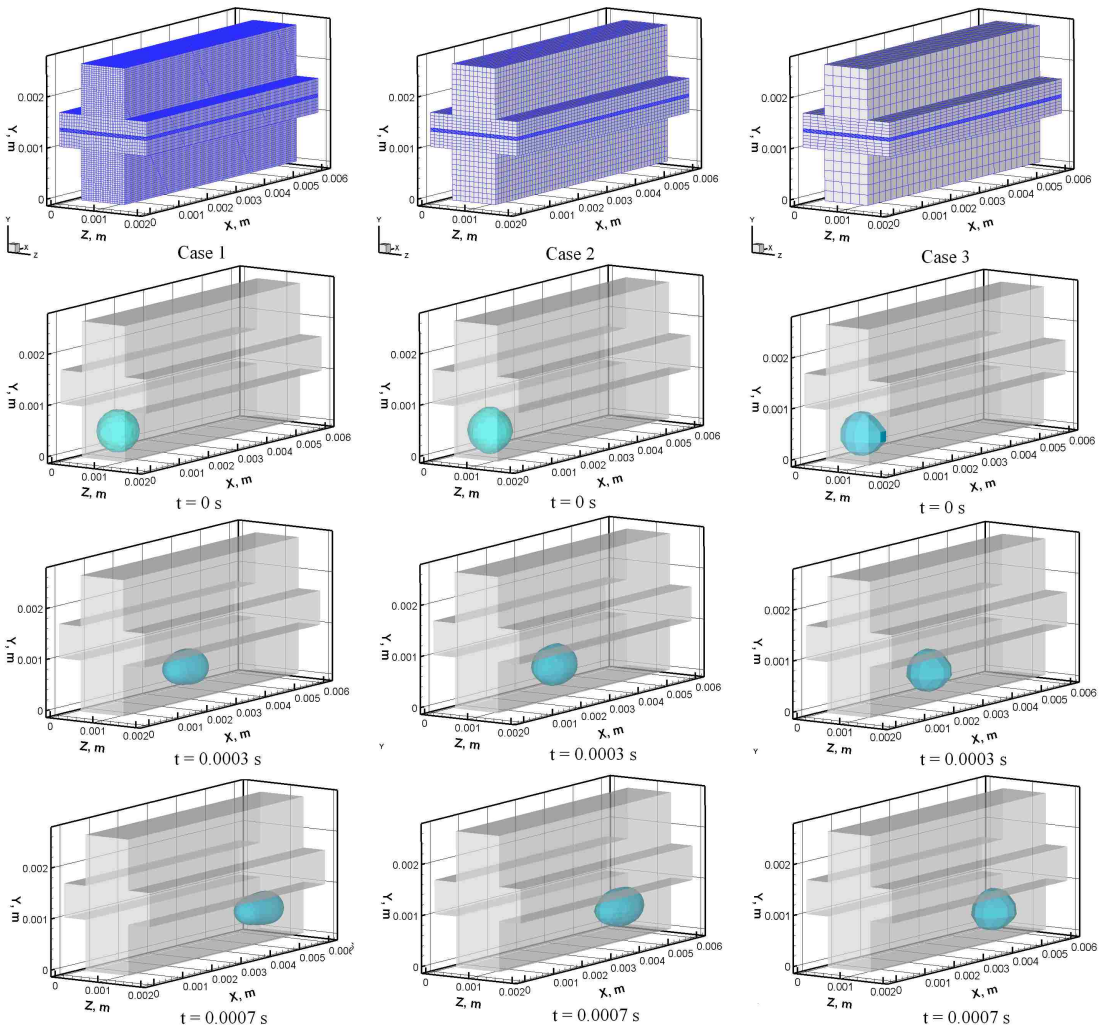


Figure 3.4: Computational grids and comparison of liquid water tracking among three cases

# Chapter 4

# Numerical Studies of Transport Phenomena in a PEMFC with Interdigitated Channel

## 4.1 Initial water drop injection into the flow channel - an effective way to examine the two-phase flow transport

The effects of liquid water do not appear immediately but instead require time. The liquid water effects will become observable as water accumulates. Based on the experimental results, it usually requires at least several physical minutes of operation to make liquid water effects observable by naked eyes. It is also noticeable that it takes a long time, even up to few months to years, to run fuel cell cases with a large number of cell grids in such few computational minutes with our present computer resource to have enough liquid water occurring in the fuel cell for investigation. In order to save the calculation time, a series of liquid water droplets was initially suspended on both the anode and cathode channels at a certain time to further examine two-phase flow behavior, especially the liquid water behavior across the porous media, together with the electrochemical reaction, heat and mass transfer.

## 4.2 Interdigitated channel design for PEMFCs - Basic concept and structure

The interdigitated flow-field channels have been widely applied to PEMFC due to its advantage that forces the reactant gas through the land in GDLs under the collectors ribs and into the electrode, driving the liquid water with the gas flow [31]. Therefore, liquid water transport and its effects would be entirely observed in

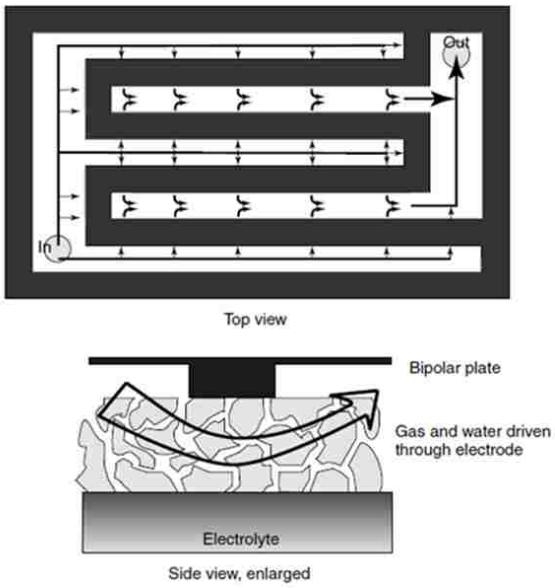


Figure 4.1: The basic principle of interdigitated flow fields (Source from book: Fuel Cell Systems Explained [80])

the flow channels and the porous media as well by implementing the VOF technique. Regarding the structure of a typical interdigitated channel PEMFC, the inlet channel shape may be serpentine or parallel without exits and the outlet channel does not have inlets, as shown in an example in Figure 4.1. Thus, the convection is dominant to help supply the reactant gases to the GDLs in short ways and remove the liquid water in the GDLs. For those reasons, an interdigitated channel-shaped PEMFC was used for simulation in this chapter.

## 4.3 Results and discussion

### 4.3.1 Analysis of liquid water transport in the channels and porous media

Figure 4.2 shows schematic diagram and computational domain of the interdigitated PEMFC used in this study with geometrical parameters listed in Table 4.1. Initially, the spherical droplets were suspended into the both anode and cathode flow channels at $t = 0.50\ s$ and $t = 0.501\ s$ (the positions of the initial droplets are shown in Figure 4.3a). The processes of motion, deformation, detachment and coalescence of water droplets versus time divided into sequential periods from $t = 0.50\ s$ to $t = 0.80\ s$ were numerically illustrated in a series of Figure 4.3.

**From t = 0.50 s to t = 0.5004 s (Figure 4.3a)**

Due to the droplet surface tension and shear stress from surrounding gas flow, the droplets were elongated downstream following the flow direction to the branches as time progressed. If the velocity gradients are large

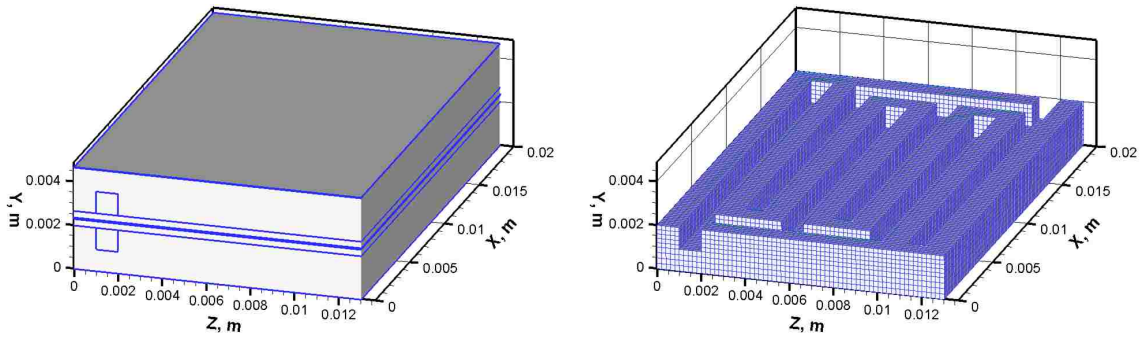


(a) Schematic diagram

(b) Geometry and computational mesh of the interdigitated channel

Figure 4.2: Geometrical structure of the interdigitated PEMFC

Table 4.1: Geometrical properties and operation conditions

| **Parameters** | **Value** |
|---|---|
| Channel width | 0.001 m |
| Channel height | 0.001 m |
| Membrane thickness | $50 \times 10^{-6}$ m |
| GDL thickness | $300 \times 10^{-6}$ m |
| Catalyst layer thickness | $10 \times 10^{-6}$ m |
| Anode and Cathode Inlet Temperature | 300 K |
| Anode inlet excess coefficient | 3 |
| Cathode inlet excess coefficient | 3 |
| Open-circuit voltage | 1.15 V |
| Gas Constant | 8,314 J kmol$^{-1}$ K$^{-1}$ |
| Anode volumetric reference exchange current density /Reference hydrogen concentration | $7 \times 10^{10}$ A kmol$^{-1}$ |
| Cathode volumetric reference exchange current density /Reference oxygen concentration | $7 \times 10^{5}$ A kmol$^{-1}$ |
| Anode transfer coefficient | 0.5 |
| Cathode transfer coefficient | 0.5 |
| Anode concentration dependence | 0.5 |
| Cathode concentration dependence | 1.0 |
| Factor accounts for energy release | 0.5 |
| Membrane porosity | 0.5 |
| Diffusion layer porosity | 0.5 |
| Catalyst layer porosity | 0.5 |
| Permeability of porous media | $1.76 \times 10^{-11}$ m$^2$ |
| Contact angle | 90° |
| Surface tension | 0.065 N m$^{-1}$ |

enough, the surface tension forces become unable to maintain the fluid particles intact, and thus it ruptures into smaller particles. Hence, after hitting the solid wall in the channels, these deformed droplets had the tendency to detach and then were broken into tiny deformed ones as slugs scattered on the wall surface. This period takes place in a short time due to high flow velocity in the channels.

**From t = 0.501 s to t = 0.504 s (Figure 4.3b)**

The small droplets sticking on the turning-wall would slowly move forward in the flow direction due to the effect of wall adhesion and surface tension while the other droplets from upstream are continuously approaching the turn, and further broken into the other smaller ones in the same way. At this moment, coalesce would be presented in the droplets, making a high concentration of liquid water in the turning area. Consequently, the water droplet grows bigger. The shear stress due to the increasing air velocity through the blocked channel would increases and then pushes the water droplets downstream and elongates the droplets into water bands at the corners.

**From t = 0.51 s to t = 0.54 s (Figure 4.3c)**

Due to strong shear stress of the main gas flow in the straight channel, the water bands and/or slugs are broken again into the smaller droplets. Those droplets disperse along the channel and some of them gradually move to the end of the channel branches along with gas flow motion. As mentioned above, although there are no exits of the inlet channels, the gas flow can pass through the GDL to the outlet channels and naturally, it tends to go to the exits of outlet channels by the shortest path. As a result, most of the droplets approach the dead end of the inlet channel close to the exit and enter the GDL region under the dead end.

**From t = 0.56 s to t = 0.62 s (Figure 4.3d)**

The slugs gradually moved to the end of the channels, then they were built up at the regions under the channel-ends in both the cathode and anode porous media. Initially, the water slugs were pushed to the porous media from the channel by the secondary flow (the flow in Y- direction from the channel to the porous media applied for both the cathode and anode). In the porous media, those slugs were also strongly influenced by the primary flow (the flow in X-Z planes that is distributed in the porous media). For slugs in the porous media of an interdigitated channel, shear force caused by flow velocity dominates the removal. Depending on the flow velocity, the slugs would be deformed and spread to annular films in the cathode porous media or would keep their shape unchanged as slugs in the anode porous media. In other words, it can be said that the different velocity distributions of the gases would influence the formation of liquid water in the porous media. Note that the inlet velocity in the cathode is higher than that in the anode so the liquid water transport in the anode and cathode are different.

**From t = 0.66 s to t = 0.82 s (Figure 4.3e and Figure 4.3f)**

In the cathode porous media, the water slugs were again elongated by a strong shear force as the time progressed. This elongation was continued until the surface tension and wall adhesion was small than the shear forces of the flow, then the slugs detached to smaller droplets (*t = 0.70 s*). Those droplets are removed to the outlet channels by the gas flow and no longer appear in the cathode catalyst layer and thereafter, the GDL. In fact, liquid water removal is feasible in the porous media of the interdigitated channel PEMFC in which the flow field was forced to pass through the porous media. In other types of flow channel such as serpentine, parallel or serpentine-parallel channels, the flow distribution in the porous media is usually much weaker when applying the same inlet mass flow rate or velocity. As a result, the liquid water is difficult to be removed in such types of channel PEMFCs. Even in the interdigitated channel with low inlet velocity (as the condition used for the anode channel of this PEMFC), the liquid water still remains unchanged in the porous media as shown in Figure 4.3e and Figure 4.3f from *t = 0.66 s* to *t = 0.82* s.

### 4.3.2 Velocity and pressure distributions under the presence of liquid water

**In the channels**

Figure 4.4a and Figure 4.4b present velocity vectors and pressure distributions on the middle-plane of the cathode and anode channels (at Y = 0.0015m and 0.00317 m), respectively, at the time *t = 0.5003 s*. In the interdigitated channels, the flow field shown in those figures is in a maze with no outlet. The reactant gases are driven by the channel pressure, forced under the collector ribs and into the electrode. It can be clearly seen that the velocity vectors in the X-Z plane are highly distributed at the inlet, decreasing along the main channel to branches and getting very small at the channel cut (the end of the branches). The red contours indicate the liquid water that was deformed due to a combination of droplet surface tension and shear stress from surrounding gas flow. Therefore, the position and shape of deformed droplets distributed at the specific time are quite different based on the inlet velocities at the cathode and anode channels. In other words, the presence and blockage of water droplets over the channel led to the flow field distributing in various ways, depending on where the droplets were located. In addition, pressure distributions in the interdigitated channels are insignificantly changed throughout the channel due to the fact that the flow resistance in the channel is very small compared with the resistance in the porous media. More interestingly, with the presence of droplets, the pressure drop reaches its highest values at around the location of the droplets due to the momentum resistance caused by the liquid water in the channel. It can be observed that the peaks of pressure coincided with the locations of droplets in the channel.

**In the porous media**

Liquid water is initially added into the channel, gradually moved in the channels and went through the porous media at the end of channel branches of both electrodes as shown in Figure 4.3e and Figure 4.3f. Similar to those in the channels, pressure and velocity distributions in the porous media are dramatically changed at the location where liquid water accumulates. Without the presence of liquid water, the velocity

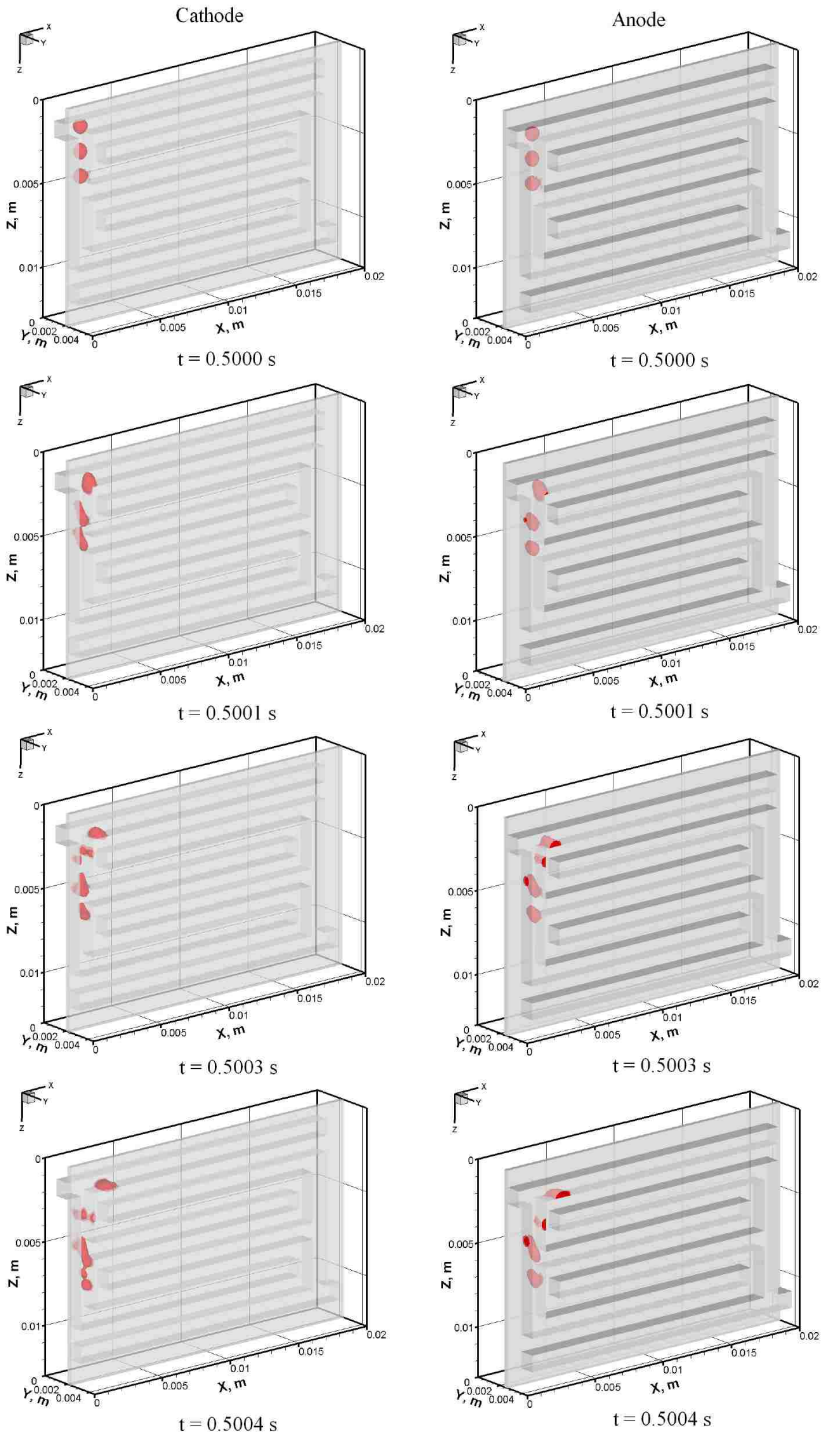


Figure 4.3a: Liquid water motion in the anode and cathode from t = 0.50 s to t = 0.5004 s

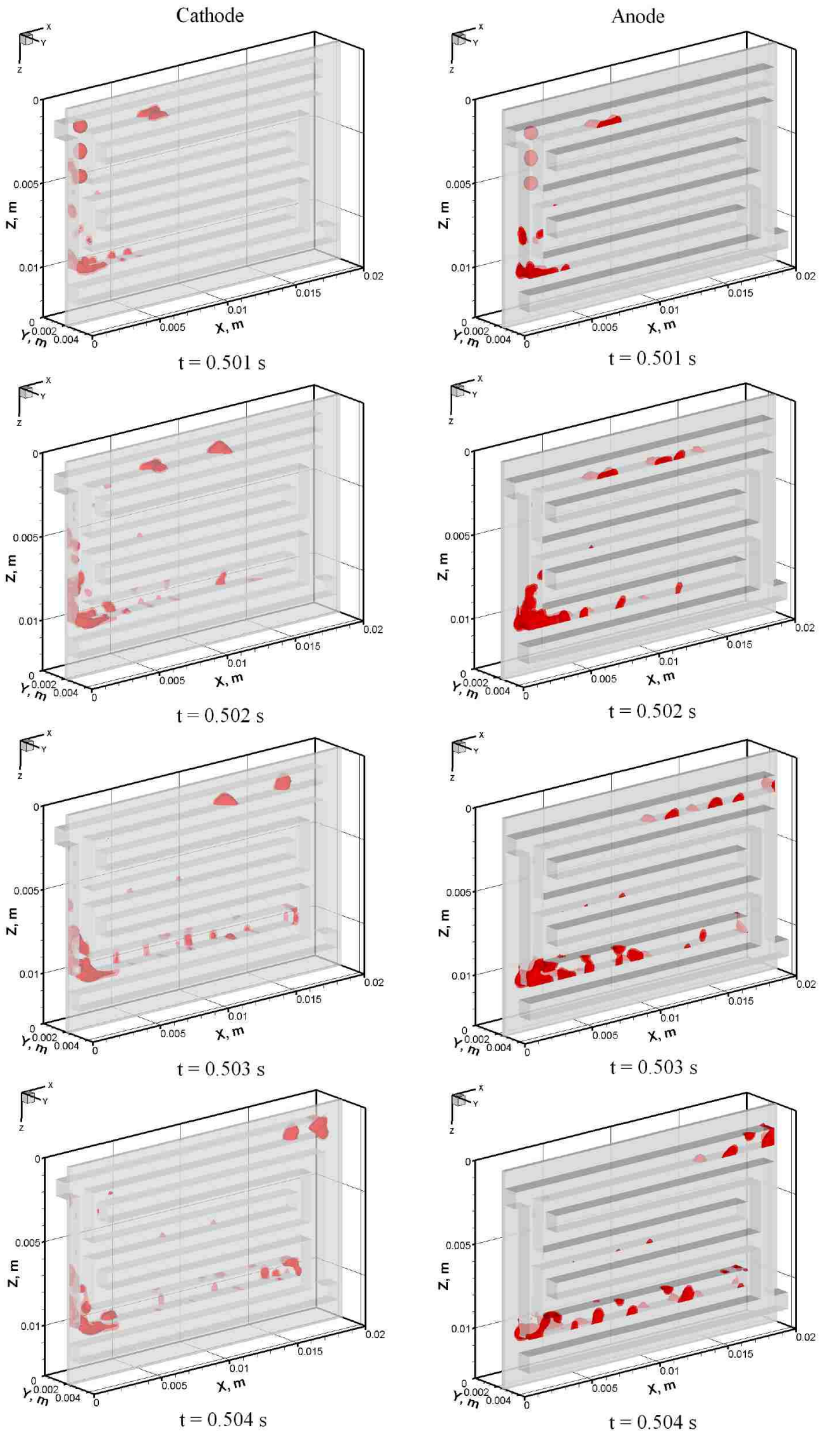


Figure 4.3b: Liquid water motion in the anode and cathode from t = 0.501 s to t = 0.504 s

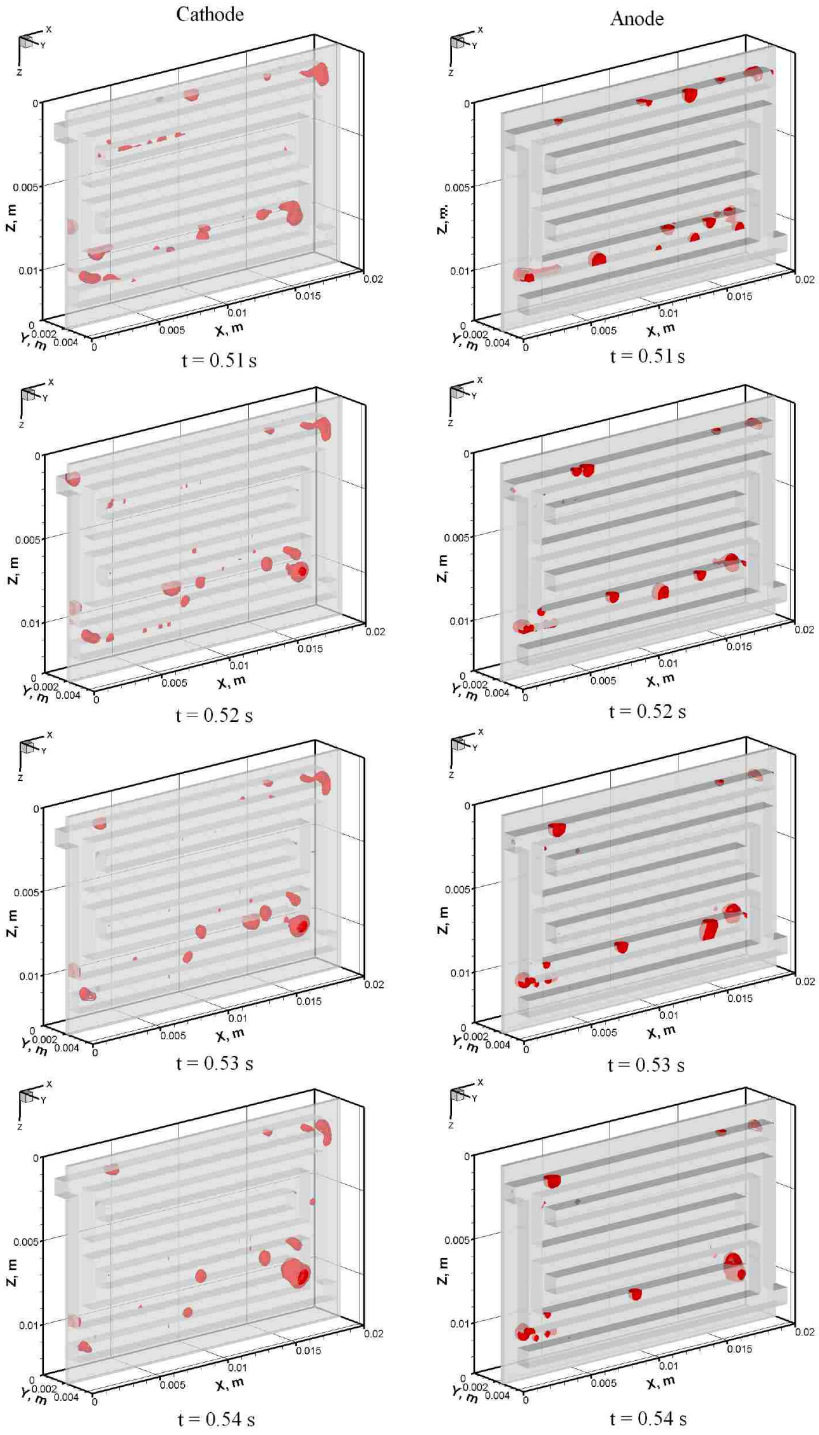


Figure 4.3c: Liquid water motion in the anode and cathode from t = 0.51 s to t = 0.54 s

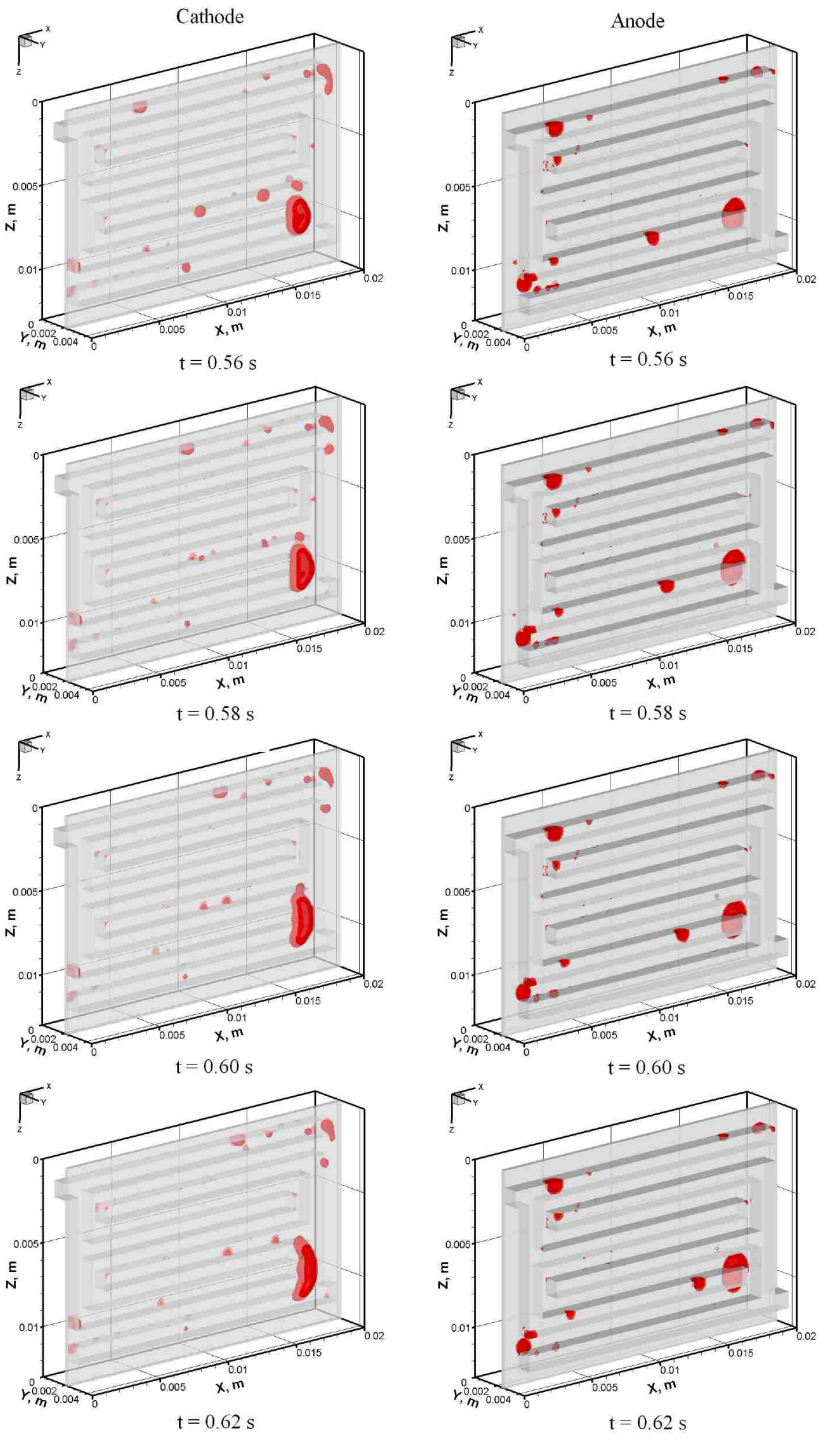


Figure 4.3d: Liquid water motion in the anode and cathode from t = 0.56 s to t = 0.62 s

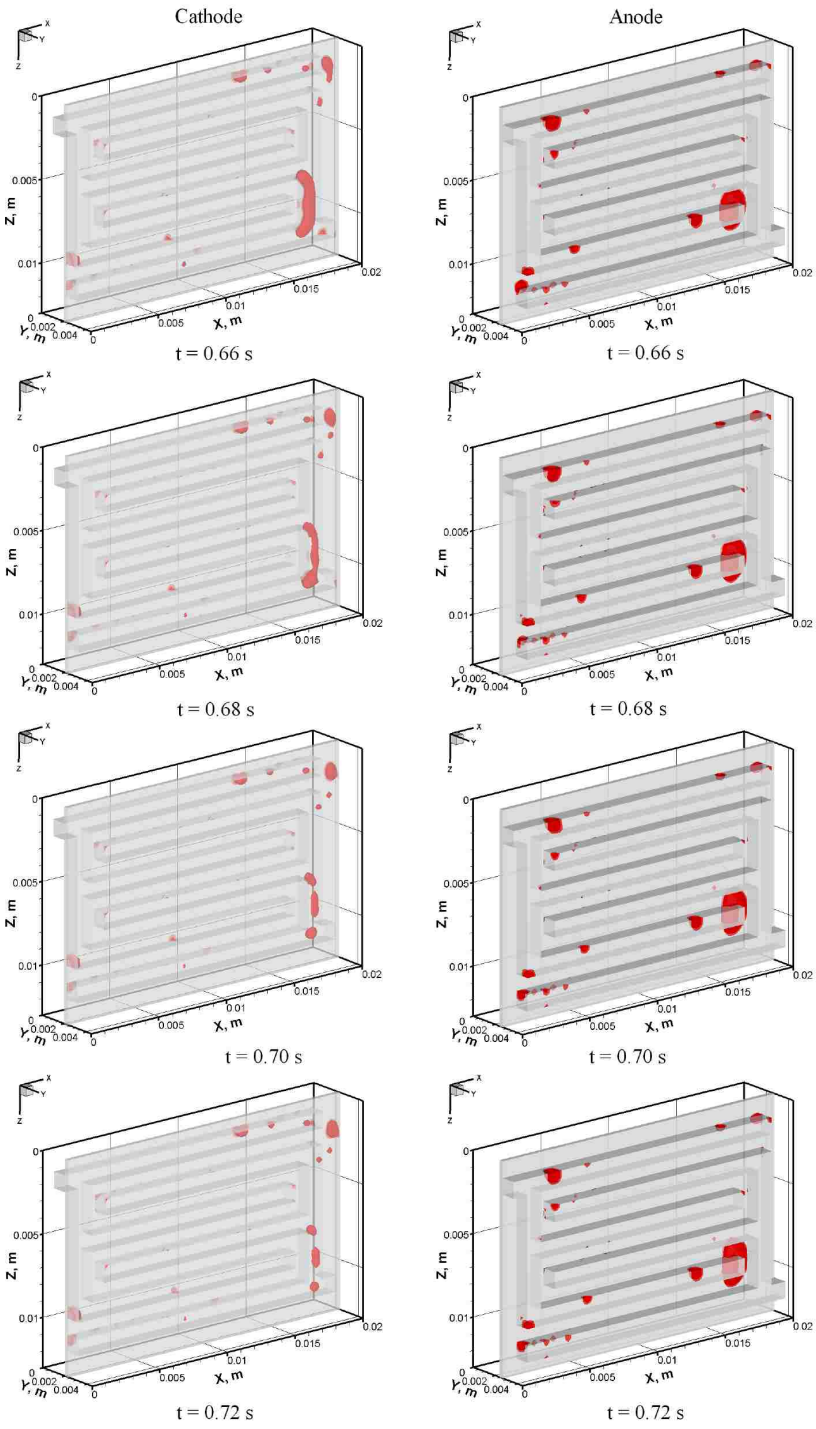


Figure 4.3e: Liquid water motion in the anode and cathode from t = 0.66 s to t = 0.72 s

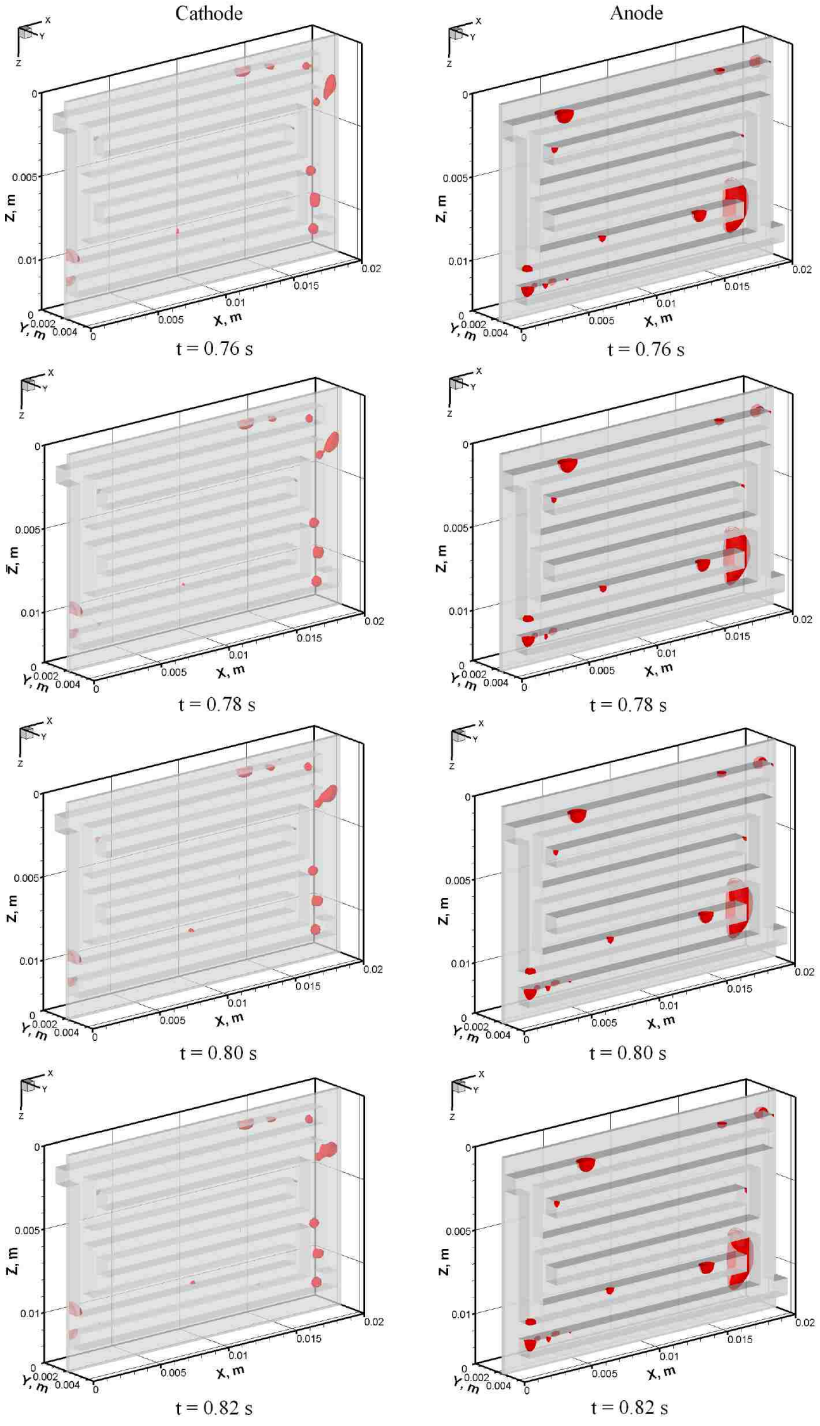


Figure 4.3f: Liquid water motion in the anode and cathode from t = 0.76 s to t = 0.82 s

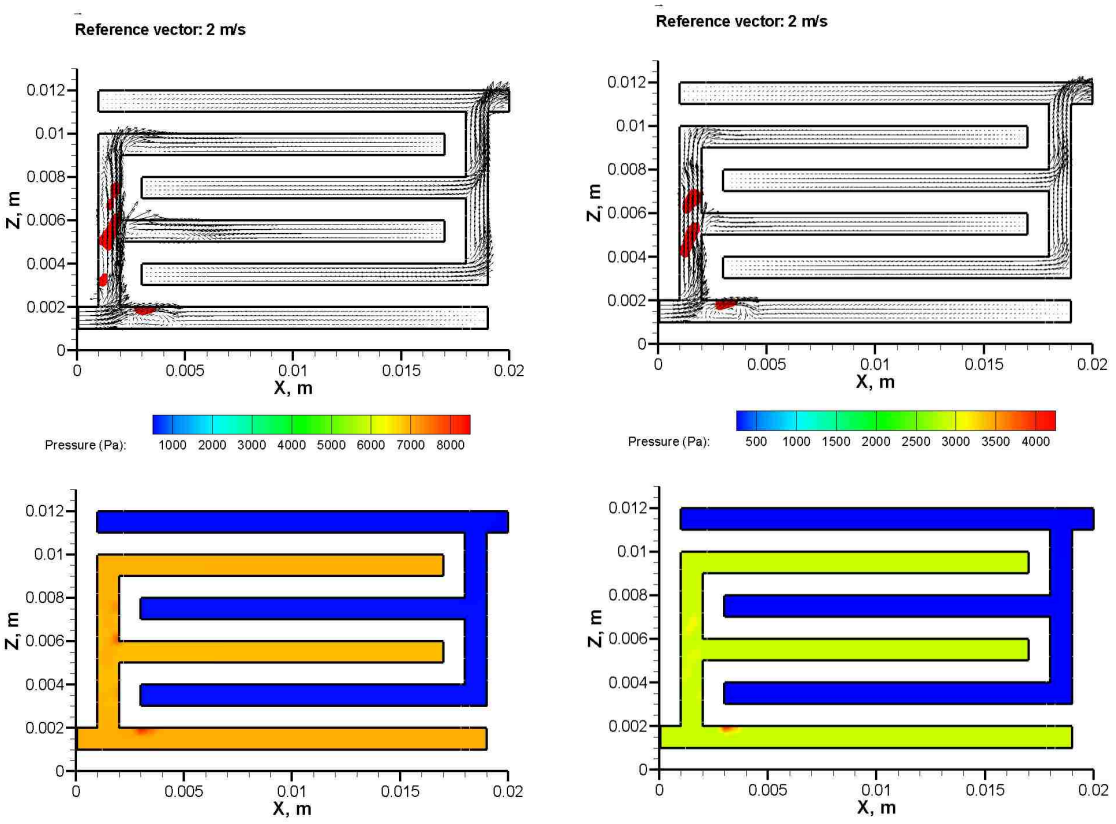


(a) On the middle-plane of cathode channel (Y = 0.0015m)

(b) On the middle-plane of anode channel (Y = 0.00317 m)

Figure 4.4: Velocity vectors and pressure distributions in the channels at t = 0.5003 s

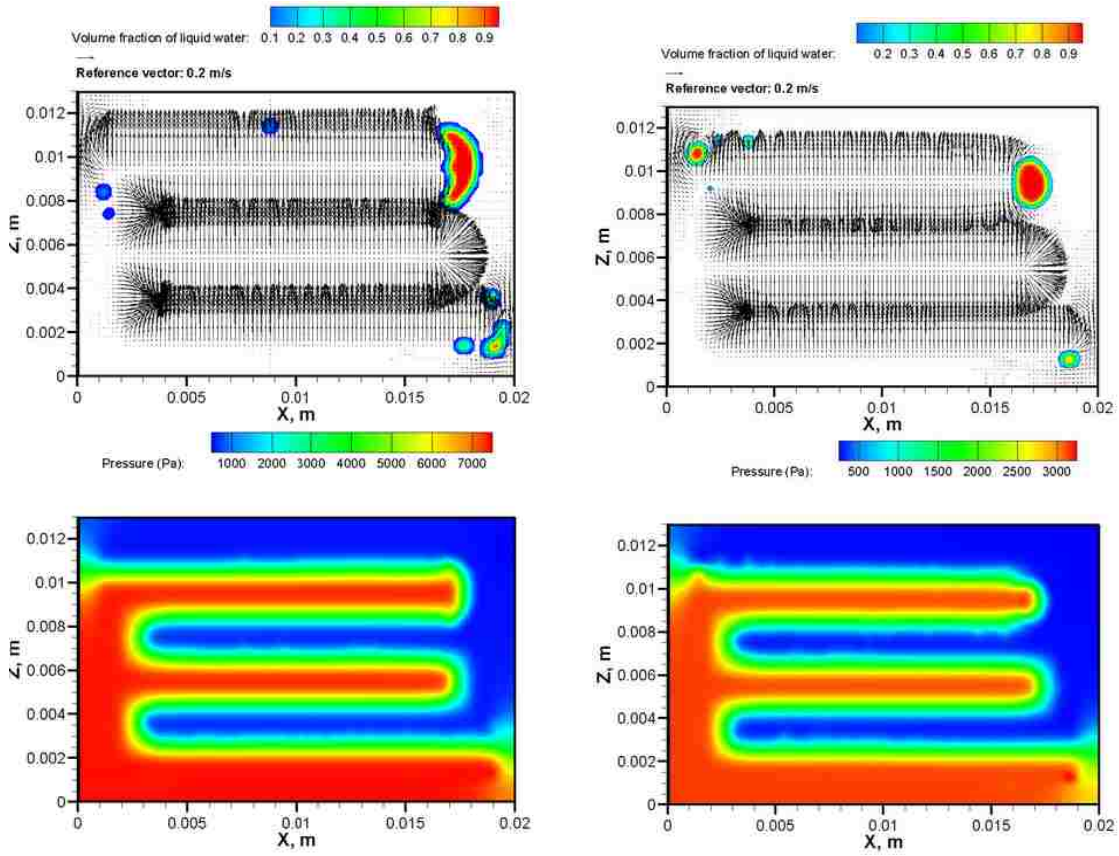


(a) On the cathode GDL/catalyst layer interface (Y = 0.0023m) (b) On the anode GDL/catalyst layer interface (Y = 0.00237m)

Figure 4.5: Velocity vectors and pressure distributions in the porous media at t = 0.62 s

distributions in the porous media are influenced by the corresponding position of the interdigitated channel. Velocity vectors tend to go through the porous media from the inlet channel to the outlet channel, such is a purpose of the interdigitated-shaped channel mentioned above. However, it would be different if there was liquid water somewhere in the porous media. One can notice that unlike the channel, the velocity of the gas flow in the porous region is quite low (approximately at the order of $10^{-1}$ m/s or under), leading to a small shear stress that could not constrain the surface tension and adhesion of liquid water buildup in this region. In other words, it is likely that the liquid water in the porous media barrier of the gas flow, result in sudden changes of the flow distribution in the locations occupied by the liquid droplets, as shown in Figure 4.5a and Figure 4.5b. In addition, liquid water also causes a significant pressure drop inside the porous media. In fact, the pressure difference is a driving force that causes the reactant gases to flow through the GDLs and catalyst layers from the inlet channels to outlet channels. Figure 4.6 show the time evolution of the motion of liquid water in the cathode GDL and catalyst layer when a portion of liquid water emerges from the porous media. The gas flow from the channel drags liquid water towards the end of the channel branches and

consequently pushes deformed droplets through the cathode GDL under the channel as seen in Figure 4.6a at *t = 0.54 s*. It is noticed that most of the liquid water emerges from the porous media at the channel-end due to the fact that there is no flow exit of the inlet channel. As mentioned above, the gas flow velocity in the GDL is small due to porous resistance, hence decreasing shear stress acts on the surface of the water droplets. Intuitively, this shear stress seems to be much weaker than that in the channels. As a result, the growth and spread of water droplets in the porous media has a longer time evolution compared to the channels as shown in Figures from t = 0.54 s to t = 0.66 s. In other words, the growth and spread of water droplets are quite slow in the GDL as well as the catalyst layer. In Figure 4.6, it also can be clearly seen that there is a large amount of liquid water concentrated in the region under the channel-end. Initially, liquid water is pushed from the channel to the porous media by the secondary flow in the Y- direction, the liquid water region is formed with a circular shape due to uniform velocity distribution. Furthermore, this region is influenced by the primary flow field distributed in the porous media (X-Z planes) instead of the secondary flow. The radial distribution of the flow velocity in the GDL region under the channel-end would make the liquid region deformed and elongated in the Z- direction as time progressed. Meanwhile, a small portion of liquid water in the GDL is pushed to the cathode catalyst layer by secondary flow in the cathode GDL, and also is deformed under the primary flow in the catalyst layer. The presence of too much liquid water in the GDL and especially in the catalyst layer would severely affect the fuel cell performance. A large amount of liquid water should be somehow removed from the porous media to prevent flooding but a small amount should be kept to maintain a high conductivity of the membrane. Interestingly, the simulation results show that it is feasible to remove the liquid water by a higher velocity field in the porous media of an interdigitated channel PEMFC as compared to the serpentine or parallel channel PEMFCs. The deformed liquid water would continuously elongate until it is partially removed to the outlet channel. This is illustrated by a decrease of the volume fraction of liquid water in the liquid region shown in Figure 4.6b at *t = 0.66 s*. It could be more clearly seen in the catalyst layer region that a large amount of liquid water first is pushed to the catalyst layer from the GDL at *t = 0.54 s*, then it is deformed and elongated under the impact of gas flow from *t = 0.56 s* to *t = 0.62 s*, and eventually is taken away from the catalyst layer at *t = 0.64 s*.

### 4.3.3 Species concentration distributions in the porous media under the presence of liquid water

#### In the cathode GDL/catalyst layer interface

Figure 4.7 shows the distributions of oxygen and water vapor concentrations on the cathode GDL/catalyst layer interface. The oxygen concentration is quite high in the porous region under the inlet and outlet channels and the area between the channels due to strong flow convection in the region. Contrary to this, the oxygen concentration in the area adjacent to the edges is lower due to a low convection. It is realized that the flow field in the area near the edges is insufficient and the oxygen concentration is dominantly due to diffusion terms. Under the presence of liquid water inside the porous media, the oxygen concentration is significantly influenced. As shown in Figure 4.7, there are few spots in the porous media that indicated low values of oxygen or water vapor concentrations. Undoubtedly, those spots represent the regions that were occupied by

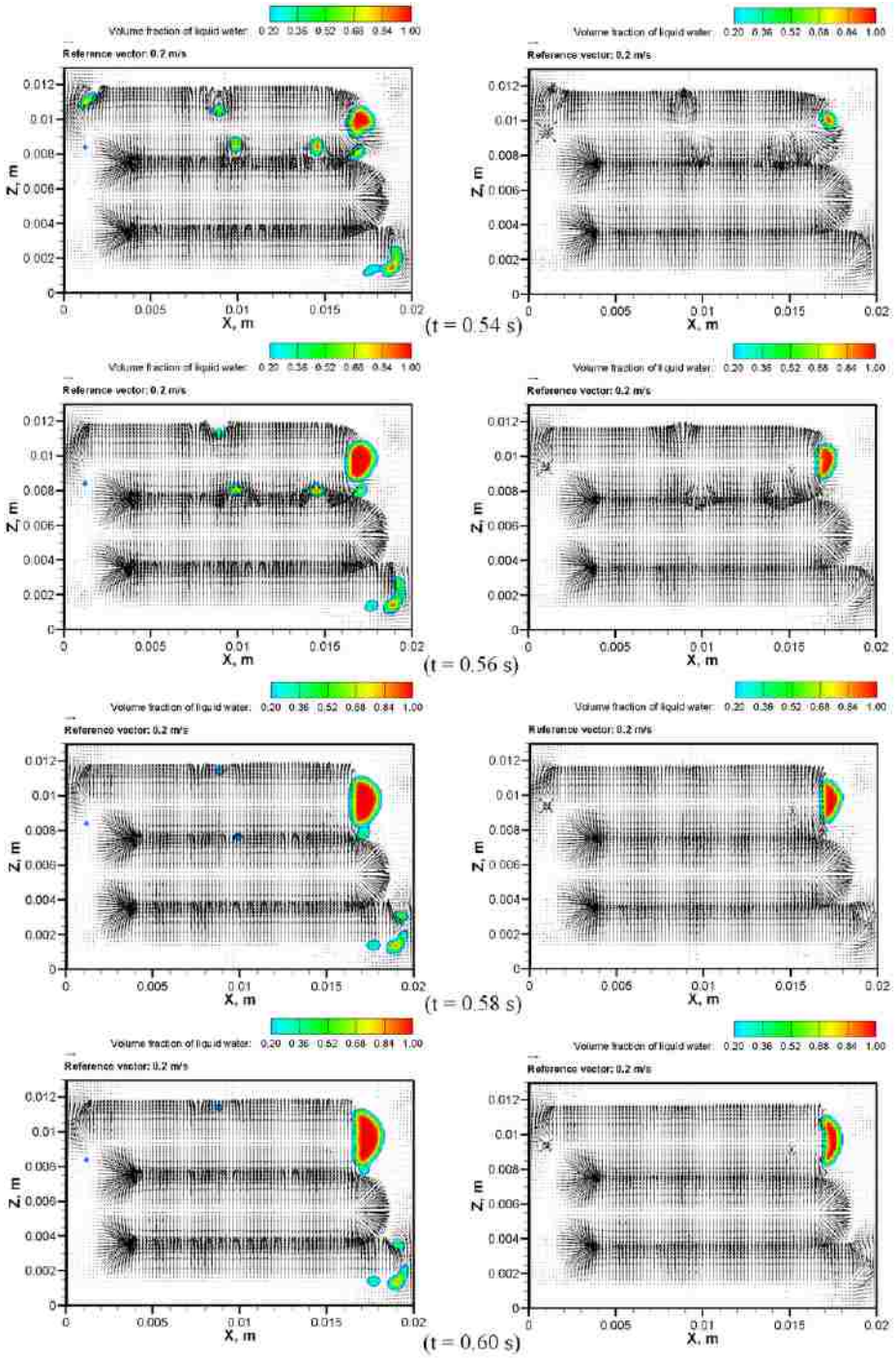


Figure 4.6a: Time evolution of the motion of liquid water in the cathode GDL (left) and catalyst layer (right) from t = 0.54 to 0.60 s

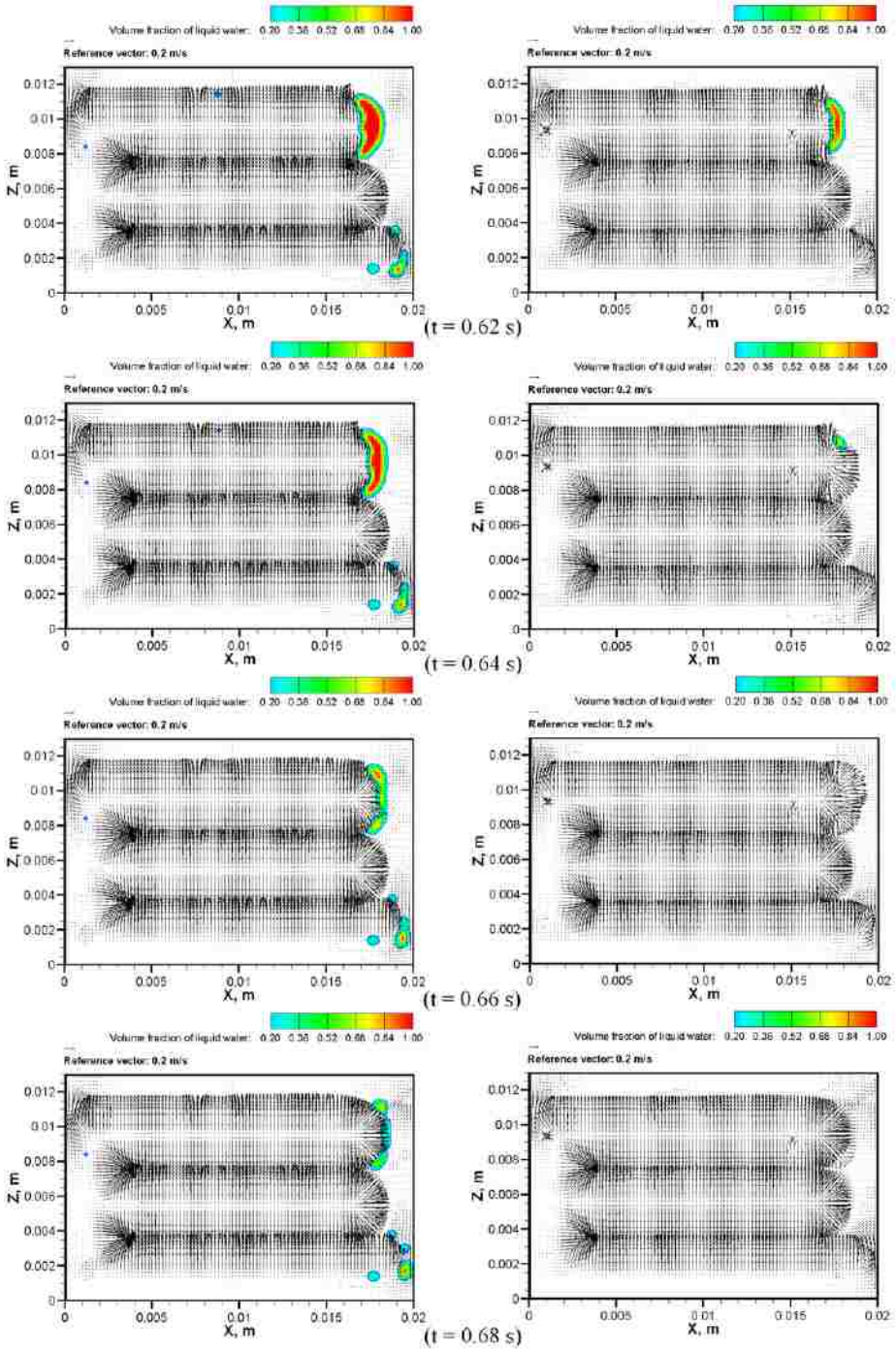


Figure 4.6b: Time evolution of the motion of liquid water in the cathode GDL (left) and catalyst layer (right) from t = 0.62 to 0.68 s

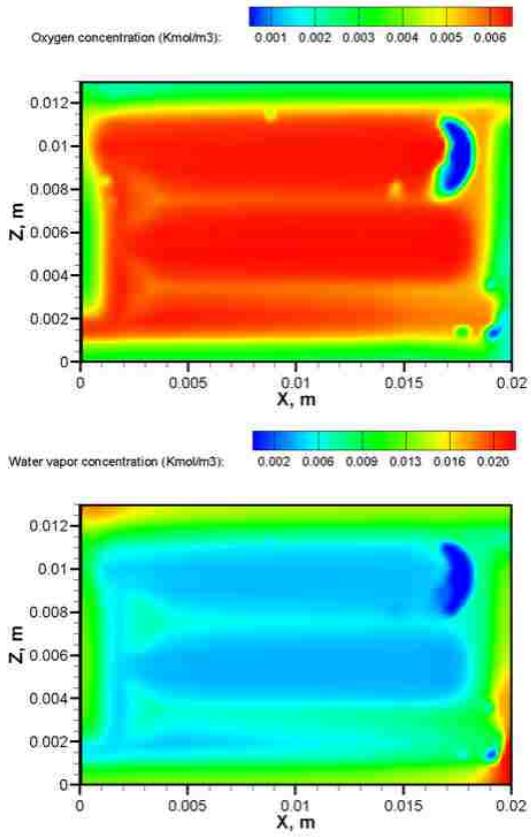


Figure 4.7: Oxygen and water vapor concentration distributions on the cathode GDL/catalyst layer interface (Y = 0.0023m) at t = 0.62 s

liquid water. The liquid water blocks the mass transport of gas species, resulting in a low concentration on the distribution of both oxygen and water vapor that were consumed and generated in the cathode catalyst layer, respectively. Interestingly, water vapor can be seen to be built-up in the area near the edges. It is the same phenomenon for the oxygen concentration, water vapor generated by chemical reaction in the catalyst layer is not easy to remove with a strong flow field in the area adjacent to the edges as discussed above in the previous section.

**In the anode GDL/catalyst layer interface**

Figure 4.8 shows the distributions of hydrogen and water vapor concentration on the anode GDL/catalyst layer interface. Similar to the oxygen in the cathode, hydrogen is also considered as a reactant gas in the anode. However, the distribution of the hydrogen concentration in the interface is quite different from the oxygen in the cathode. Hydrogen seems to be evenly distributed on the interface regardless of the distribution of the flow field (convection effect) in the porous media. This can be clearly explained by the high diffusivity

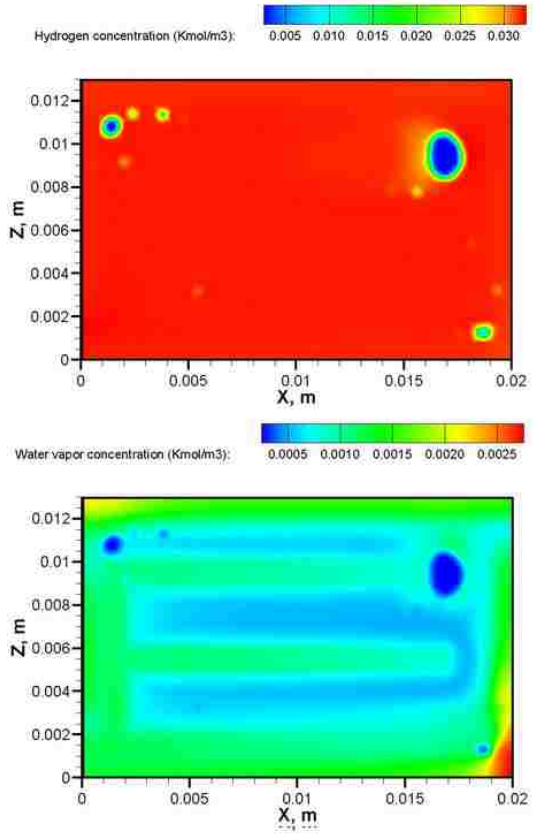


Figure 4.8: Hydrogen and water vapor concentration distributions on the anode GDL/catalyst layer interface (Y = 0.00237m) at t = 0.62 s

of hydrogen gas which causes the effect of convection on the hydrogen concentration to be negligible. The way that liquid water effects the hydrogen distribution is similar to that effects the oxygen distribution on the cathode GDL/catalyst layer interface. The build-up of water vapor in the area adjacent to the edges also can be seen in the anode catalyst layer and GDL. It is noticeable that the water vapor is supplied to the anode inlet as a humidifier and it would be dragged through the membrane from the anode to the cathode due to electro-osmotic drag force. The amount of dragged water depends on the reaction rate or in other words the current density. Therefore, it could not be doubted that the water vapor concentration in the porous region under the inlet and outlet channels and the area between the channels is lower than the other regions due to a high current density distributed in the region.

### 4.3.4 Temperature distribution under the presence of liquid water

Figure 4.9 shows the temperature distributions on the cathode and the anode GDL/catalyst layer interfaces, respectively. The heat generation is due to the electrochemical reaction and Ohmic heating. Therefore,

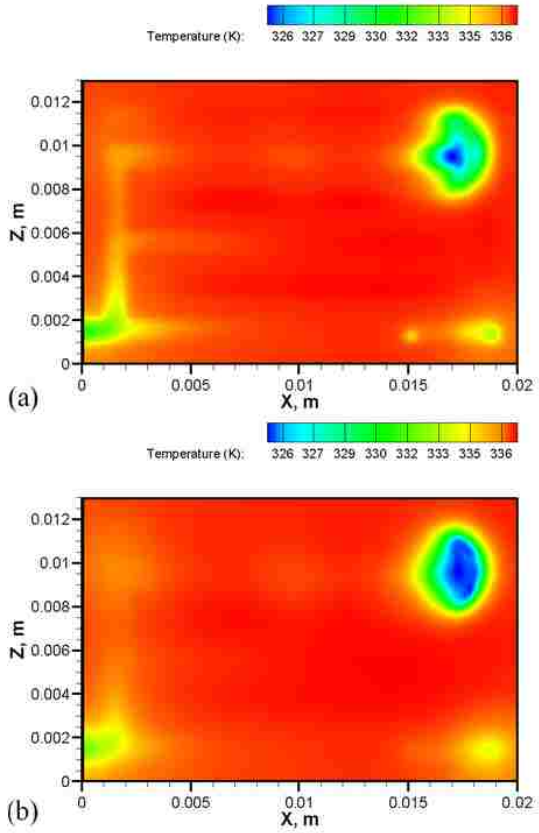


Figure 4.9: Temperature distributions at t = 0.62 s: (a) on the cathode GDL/catalyst layer interface (Y = 0.0023m) and (b) on the anode GDL/catalyst layer interface (Y = 0.00237m)

the temperature is proportional to the reaction rate, which corresponds to the local current density distribution in the membrane (Figure 4.11). Note that the heat transport in fuel cells is by diffusion, conduction and convection. The temperature distribution through the solid materials (including flow plates/collectors and solid phase of porous media) is also performed by the heat conduction process. Depending on different solid materials, the thermal conductivity may change, resulting in different temperature distributions in different solid layers. A uniform temperature distribution in the porous media is due to the high thermal conductivity of the solid material. However, the lowest temperature affected by convection could be observed at the flow inlet where the gas flows in at the ambient temperature. More interestingly, in the two-phase model, the presence of liquid water also affects the distribution of the cell temperature by absorbing heat from the cell, locally cooling down the temperature of the region where liquid water occupied, as seen in Figure 4.9. As mentioned above, by controlling the convective coefficient h (Eq. 3.60), the cell temperature distribution is in a good range of 325 K to 337 K.

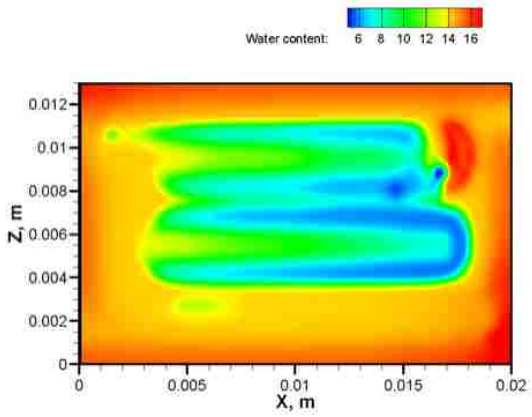


Figure 4.10: Water content distributions on the cathode GDL/catalyst layer interface (Y = 0.0023m) at t = 0.62 s

### 4.3.5 Water content, water flooding and their effects on the current density distributions in the porous media under the presence of liquid water

Figure 4.10 presents water content on the cathode GDL/catalyst layer interface. The water content is a function of water activity which is the ratio of the water vapor pressure to the saturated pressure. In the porous media, water content and ionic conductivity are strongly related. In general, the proton conductivity increases linearly with increasing water content. High water content in the porous media is desired to increase the conductivity and the current density as well. Similar to the distribution of water vapor concentration, it can be explained for the high water content in the porous media under the area adjacent to the edges and the low water content in the area under the channel in which water is taken away by forced convection.

Contrary to this, the presence of liquid water severely influences on the current density by blocking the mass transport of reactant gas, restricting reactant availability and degrading the chemical reactions in the catalyst layers, resulting in a low current density distribution or performance loss where liquid water exists as seen in Figure 4.11. Intuitively, Figure 4.11 shows that the current density where the flooding occurs was observed at a value under 1000 A/m$^2$. Meanwhile, an average current density is valued at 6000 A/m$^2$ and high values are over 7000 A/m$^2$. Furthermore, it can be noticed that the liquid water distribution in the porous media is not generally uniform and it might be easy to remove under a high convection due to the structure of interdigitated channel design. The removal of water from under the lands into the channel is essential to avoid flooding. However, a dry condition can result in low performance and durability. It could then be to trap liquid water somehow in order to humidify the porous media, especially in the anode. Hence, the interdigitated channel might have a limitation in keeping the liquid water for this purpose.

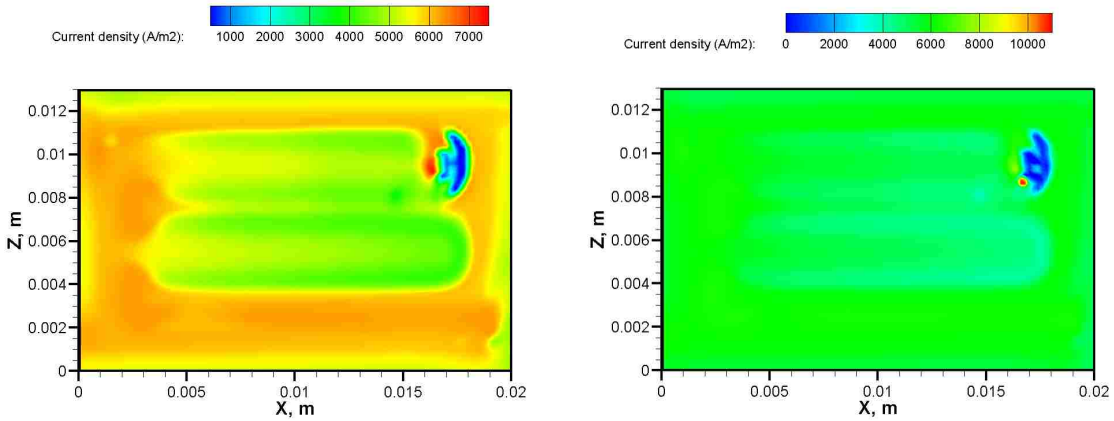


(a) On the cathode GDL/catalyst layer interface (Y = 0.0023m)

(b) On the mid-plane of the membrane (Y = 0.002335 m)

Figure 4.11: Average current density distributions at t = 0.62 s

## 4.4 Conclusions

In this chapter, the transport of water droplets in the channels and porous media has been investigated to figure out physical understanding of liquid water behavior including deformation, coalescence and detachment. By injecting the liquid droplets into the channels at the initial time of operation, the trace of liquid water in the channel and porous media was also predicted by analyzing the characteristics of liquid water and the influence of the interdigitated flow field on the liquid water distribution. The numerical results show that the presence of liquid water in the interdigitated channels and porous media significantly influences flow field, species concentrations, heat, mass and current transport. For an interdigitated channel PEMFC, it shows that the reactant flow and transport to the channel and porous media is primarily subject to forced convection from gas flow. Therefore, this design effectively enhances the liquid water removal and forces the reactant flow to the GDLs and catalyst layers. Thus, the removal of liquid water strongly depends on the magnitude of flow field. On the other hand, the presence of liquid water in the channel and porous media leads to an uneven distribution of gas flow. As a result, this phenomenon provides inadequately distributed mass transfer to the catalyst layers and requires a pressure supply for the fuel cell - it will consume more energy during fuel cell operation. By investigating the behavior of liquid water in the catalyst layers at different periods of time, it can be clearly observed that the liquid water blocks the gas transport in the fuel cell, resulting in a degradation of local current density. This effect severely impacts the cell performance, especially when the flooding is significant.

# Chapter 5

# Numerical Studies of Transport Phenomena in a PEMFC with Serpentine Channel with Phase Change Effect

## 5.1 Phase change and its effect on the presence of liquid water in PEMFCs

In fact, liquid water is formed in a PEMFC due to condensation at certain regions depending on local temperature and pressure and on the other hand, water vapor is also formed due to evaporation from the liquid phase. By incorporating the phase change and VOF method with fluid dynamics, heat and mass transport and electrochemical reaction processes to a PEMFC simulation, the formation, motion and removal of liquid water in the channels and porous media can be numerically visualized in real-time. Without injecting water liquid droplets at initial time, the transition of liquid-vapor would be investigated by applying the phase change effects into the channel and voids of porous media. In this approach, the phase change rate is used to be a main factor for determining phase change equilibrium (Eq. 3.49) and it is added into the source terms of mass, species and energy equations.

## 5.2 Computational domain description

In this chapter, the phase change and VOF numerical model is applied into a serpentine channel PEMFC with 230,688 grid cells in the computational domain as shown in Figure 5.1. The electrode collectors and

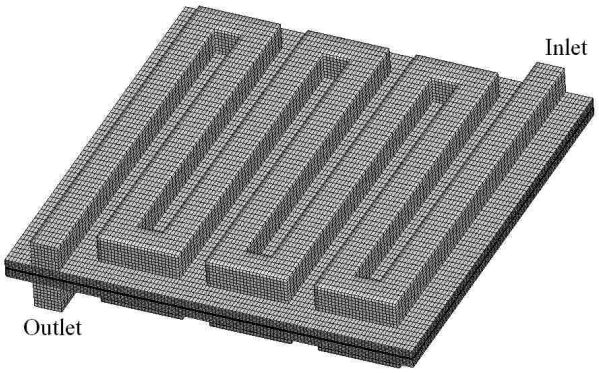


Figure 5.1: Computational domain and mesh of the serpentine PEMFC

cooling channels are not considered to reduce the calculation quantity and time. Since the electric and thermal conductivity of the collectors' material is high to disregard the Ohmic loss of the collectors, the assumption of neglecting the energy transport in the collector is reasonable. Because the goal of this work is to numerically simulate a real-time operation of liquid water motion, formation and removal in a Proton Exchange Membrane Fuel Cell, the water liquid transport and physical phenomena in a real-time operation in the first 10 seconds of operation are described.

## 5.3 Results and discussion

The results shown in this section are obtained for the properties and operating conditions listed in Table 5.1.

### 5.3.1 Liquid water formation, motion and removal

**The initial formation of liquid water in the cathode channel**

The volume fraction of liquid whose values are in between zero and unity is represented to determine the presence of liquid water in the fuel cell. From this point of view, the presence of liquid water more or less would be determined by various values of liquid volume fraction displayed in the figures. As the fuel cell starts running at the time $t = 0\ s$, the humidified gas flows is supplied to the cathode and anode channel inlets. There is no liquid formed in the fuel cell at this stage because of the following reasons: only water vapor is supplied from the channel inlets, a little amount of water is generated in the cathode catalyst/membrane interface. The water transport mechanism through the membrane begins its operation. Hence, the water vapor built-up is not much enough to significantly increase its concentration to form liquid water. As the time progressed until $t = 0.52\ s$, the liquid water starts to be observed in the cathode channel although its amount is too small - the values of volume fraction of liquid presented in Figure 5.2 are roughly 0.02 to 0.1.

Table 5.1: Geometrical properties and operation conditions

| **Parameters** | **Value** |
|---|---|
| Channel width | 0.001 m |
| Channel height | 0.001 m |
| Membrane thickness | $50 \times 10^{-6}$ m |
| GDL thickness | $300 \times 10^{-6}$ m |
| Catalyst layer thickness | $10 \times 10^{-6}$ m |
| Anode and Cathode Inlet Temperature | 300 K |
| Relative humidity at cathode inlet | 2.25 |
| Relative humidity at anode inlet | 1.3 |
| Cathode inlet excess coefficient | 1.2 |
| Anode inlet excess coefficient | 3 |
| Open-circuit voltage | 1.15 V |
| Gas Constant | 8,314 J $\text{kmol}^{-1}$ $\text{K}^{-1}$ |
| Anode volumetric reference exchange current density /Reference hydrogen concentration | $7 \times 10^{10}$ A $\text{kmol}^{-1}$ |
| Cathode volumetric reference exchange current density /Reference oxygen concentration | $7 \times 10^{5}$ A $\text{kmol}^{-1}$ |
| Anode transfer coefficient | 0.5 |
| Cathode transfer coefficient | 0.5 |
| Anode concentration dependence | 0.5 |
| Cathode concentration dependence | 1.0 |
| Factor accounts for energy release | 0.5 |
| Membrane porosity | 0.5 |
| Diffusion layer porosity | 0.5 |
| Catalyst layer porosity | 0.5 |
| Permeability of porous media | $1.76 \times 10^{-11}$ $\text{m}^2$ |
| Contact angle of the channel | $70^\circ$ |
| Surface tension | 0.065 N $\text{m}^{-1}$ |
| Condensation rate | 100 $\text{s}^{-1}$ |

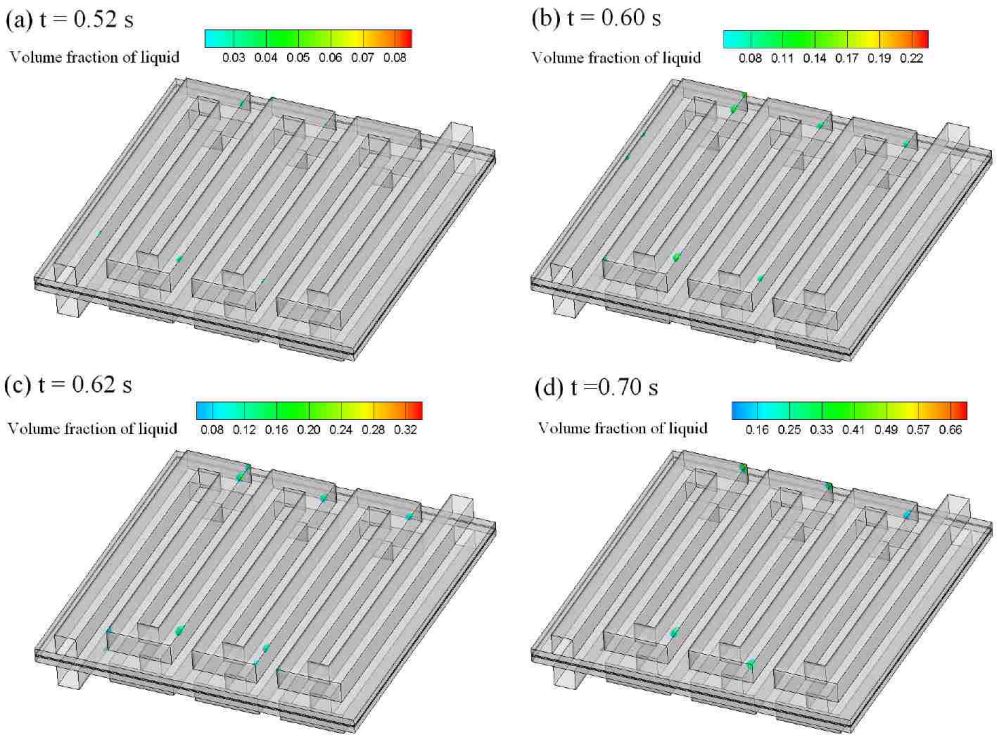


Figure 5.2: Liquid water motion in the anode and cathode from t = 0.52 s to t = 0.70 s

**The initial formation of liquid water in the porous media**

Even if the generated liquid water amount is too small to be considered as real liquid droplets, the liquid water accumulation is continually taking place, resulting in an increase of volume fraction of liquid water. In other words, the droplet formation is rising up. It also can be seen in the figures at the different instants, the slight change of the droplets' positions indicates that the droplets are pushed towards the corners of the channel along the gas flow direction. At $t = 0.60$ s when the liquid volume fraction get the values at around 0.15 to 0.3, the formation of liquid water in the porous media is initially observed as shown in Figure Figure 5.2c and continue growing as shown in Figure 5.2d.

**The formation and growth of the droplets in the cathode channel corners**

The droplets will coalesce as they move along the flow channel towards the turns and accumulate in the first corners of the turns where the flow velocity can be neglected. The small and large droplets are formed in different positions in the channel. But they will combine to form the larger ones in the channel corners since the small droplets move and overtake the larger droplets. Another effect to support the growth of liquid droplets in the corners is mass transfer from vapor phase to liquid phase of accumulated water along with time. As seen in Figure 5.3, the droplets in the corners become bigger in terms of size and volume fraction although the growth process takes longer time than the formation process of liquid water.

**The growth of the droplets in the porous media**

Liquid water continuously occurs in the porous media in different positions after the initial liquid droplet is formed in the cathode GDL. As shown in Figure 5.3a at t = 1.0 s, there are at least three positions of liquid water distributed in the porous zone. The small droplets of liquid water in such positions gradually grow to become the bigger ones as the time progresses. Here is noticeable that the mechanism of the growth of liquid water in both the channel and the porous media seems to be analogous from the point of view of flow convection. The condition of growth of liquid droplets is that the flow field velocities or flow convection at the droplet-formation positions is small enough. Since that, the growth of water droplets can develop without any impacts from a strong air-flow field. This is explained as shown in Figure 5.3a to Figure 5.3d that there are positions of liquid water growth existing almost in the channel corners and in the porous media under the collector ribs where the air-flow convection is trivial.

**The removal of the droplets in the cathode channel**

Liquid droplets continuously grow and expand in the corners with time until it is likely to block the channel and hinder the air flow in the turns. This blockage leads to a decrease of the cross-sectional area and an increase of flow velocity as the inlet flow rate remains constant. Thus, the shear stress from the air flow prevails against the droplets' surface tension, thus resulting in significant droplet elongation and deformation. The air flow also pushes the deformed droplets out of the corners towards the flow stream, causing the droplets removal. Figure 5.4 show how the droplets in the corners are deformed and removed by flow stream. Most

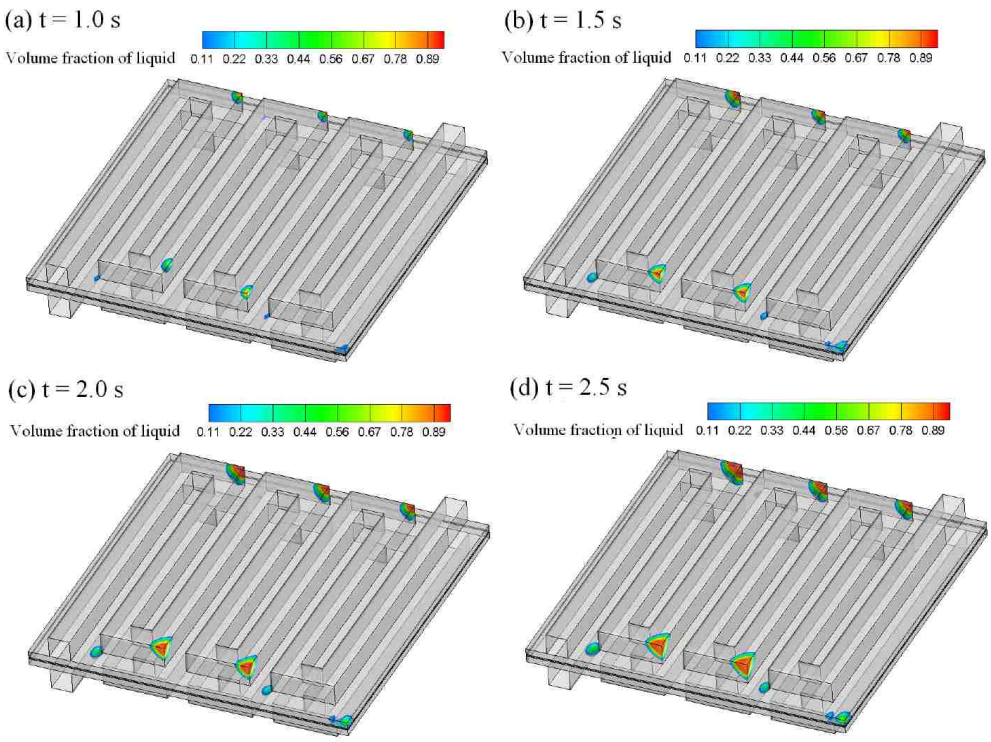


Figure 5.3: Liquid water motion in the anode and cathode from t = 1.0 s to t = 2.5 s

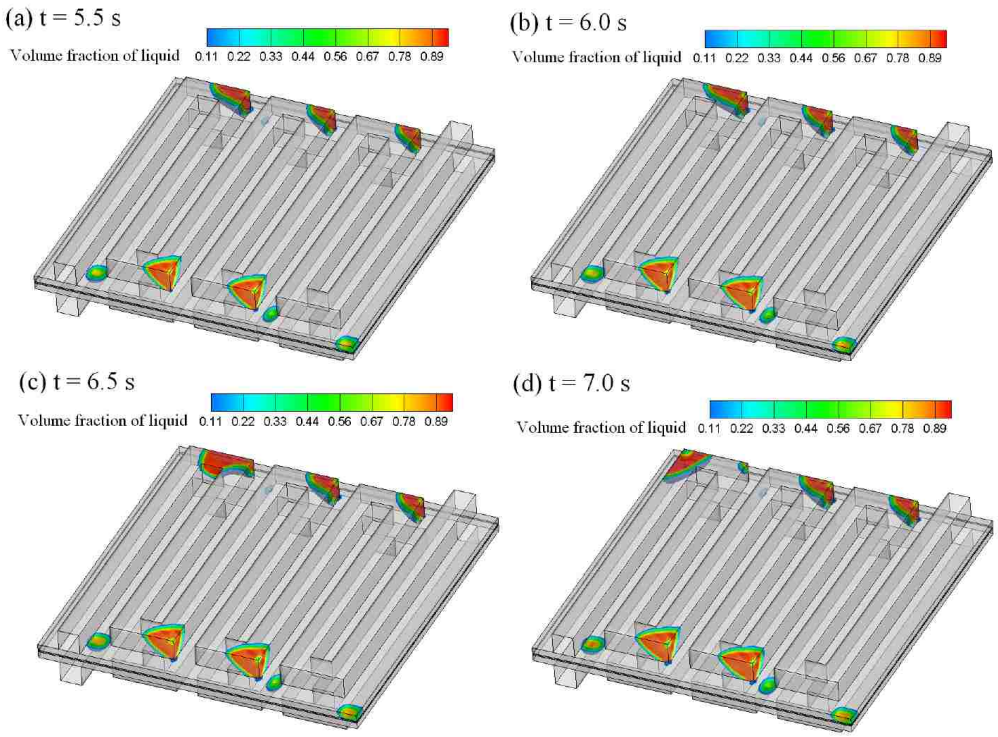


Figure 5.4: Liquid water motion in the anode and cathode from t = 5.5 s to t = 7.0 s

clearly, the droplet in the corner of last turn can be seen as it was pushed to the other corner (at *t = 7.0 s*) and was removed out of the channel (by *t = 7.6 s*). Other droplets in the corners moving ahead to the next corners is also shown in Figure 5.5 and Figure 5.6 with various time instants until t = 10.0 s.

**The removal of the droplets in the cathode porous media**

Liquid water was formed and gradually expanded in the porous media. Under the strong impact of flow field in the cathode GDL, it moves out to the channel. This phenomenon could be observed in Figure 5.7 as it was divided into two processes: water removal out of the channel and water removal from the GDLs to the channel. For the water removal process from the GDLs to the channel, it can be explained that gas flow field in the porous media that was formed by pressure difference between two sequence channel branches in the serpentine channel, forces the liquid water to the channel along with flow direction. Although the magnitude of gas flow velocity is quite small in the porous media (order of millimeter per second) when compared to the gas velocity in the channel (order of meter per second), the liquid water can still be pushed out. In the water removal out of the channel, liquid water is taken away from the channel by two mechanisms: it may be pushed out by the strong gas flow in the channel or may be taken by other big liquid drops moving out of the channel, as shown in Figure 5.7 at *t = 8.96 s*.

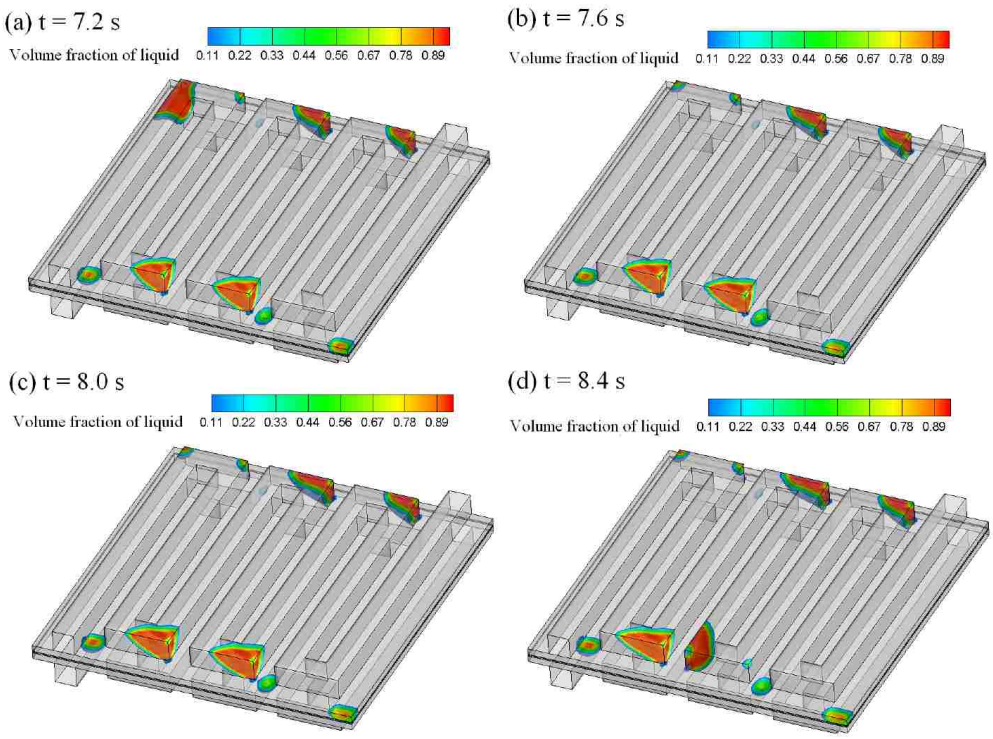


Figure 5.5: Liquid water motion in the anode and cathode from t = 7.2 s to t = 8.4 s

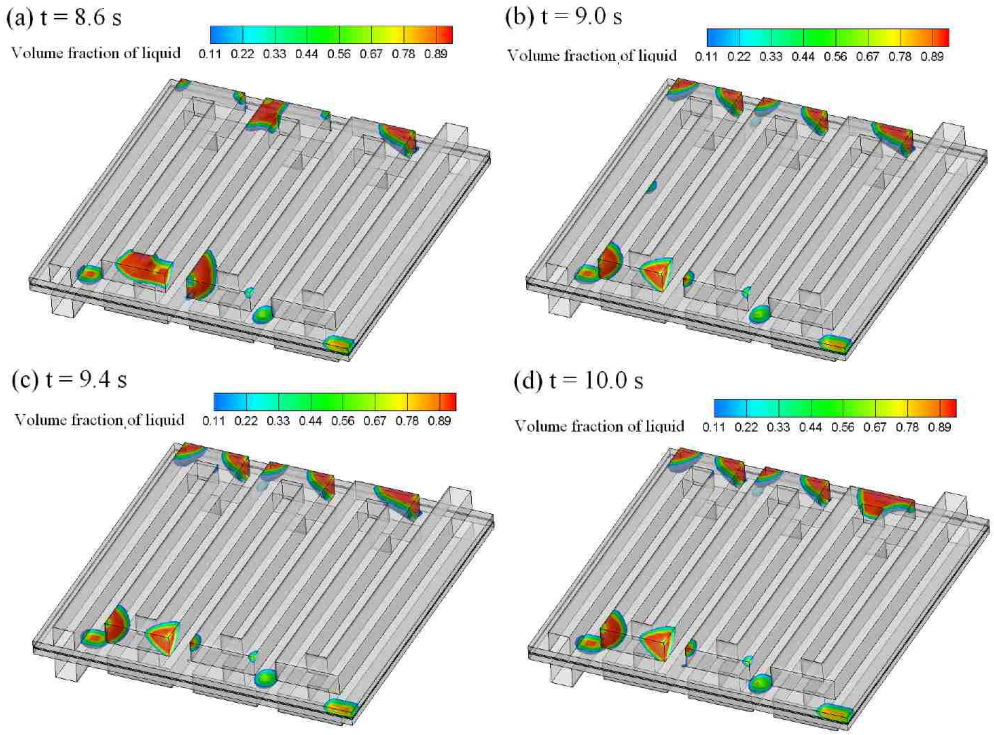


Figure 5.6: Liquid water motion in the anode and cathode from t = 9.4 s to t = 10.0 s

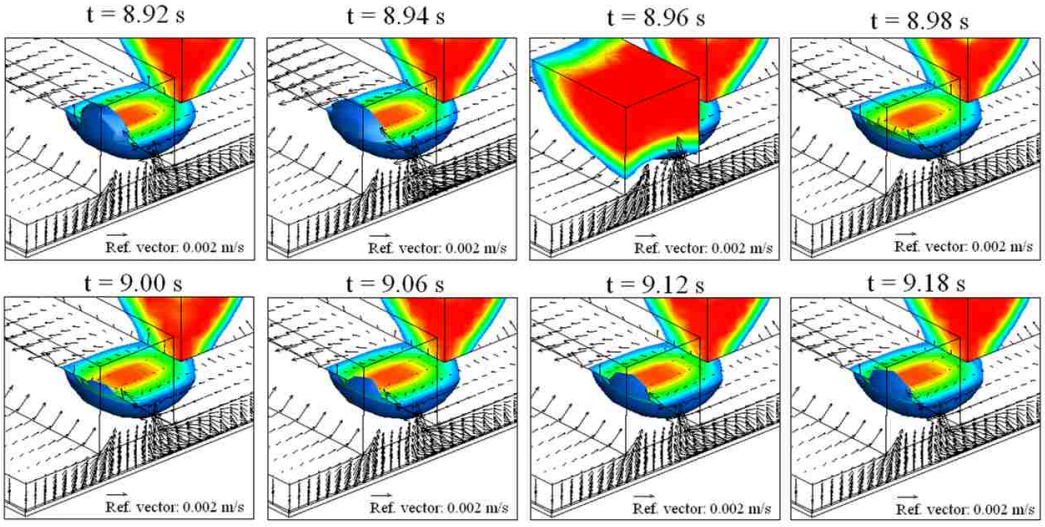


Figure 5.7: Liquid water removal in the cathode channel and GDL

### 5.3.2 Liquid water formation and removal in the cathode channel and GDL throughout the fuel cell operation within the first 10 seconds

Figure 5.8 shows the liquid water amount in the cathode channel and GDL and corresponding average current density of the fuel cell from the starting time to $t = 10.0\ s$. The increase of liquid water amount with time indicates the formation of liquid water as the phase change is implemented to the model. The liquid amount in the cathode GDL is likely to gradually increase since the liquid water is generated and accumulated in the porous media. Meanwhile the liquid amount in the cathode channel fluctuates after its linear increment until around $t = 7.0\ s$. This is due to the fact that there are repeated accumulation and removal of the liquid water in the channel. The liquid water formed due to phase change is gradually accumulated in the channel until a certain amount is big enough to be removed by the gas flow. Actually, the water removal did occur in the cathode GDL as mentioned in Figure 5.7, as well as in the cathode channel. However, it can be explained that the liquid amount removed in the cathode GDL is quite smaller than the liquid formed and hence, the decrement of liquid water can not be clearly seen due to removal in the cathode GDL. The average value of current density versus time is also depicted in Figure 5.8. The current density initially increase until it reaches at around 7000 A/m$^2$ (the fixed fuel cell voltage is 0.5 V). After reaching this critical value, the average current density slightly reduces due to the effect of liquid water in the fuel cell: if liquid water blocks the flow field and/or mass transport of reactant gas at a certain location, the average current density then decreases. It is not clear to observe this phenomenon in the first 10 seconds since the flooding is insignificant (not much liquid generated and causes flooding). In case the fuel cell operates in minutes or the fuel cell contains much liquid, the influence of flooding on the current density can be examined as introduced in chapter 4 and our studies [48, 49, 50].

### 5.3.3 Effects of liquid water on physical and transport properties

Because the fuel cell operation is an unsteady process, the numerical data at a $t = 4.5\ s$ are analysed to qualitatively investigate the change of physical and transport properties in local regions of the cathode under the presence of liquid water.

#### Effect of liquid water on flow field

The numerical results presented in Figure 5.9 explicitly prove that the liquid drops in the channel are critical factor to cause the changes on gas-flow velocity field and pressure distribution in the channel and porous media as well. When there are liquid drops accumulated in the corners of flow channel, they would block the channel like baffle by reducing the cross-sections of the channel near the corners, increasing gas-flow velocity before entering the channel turns as shown in Figure 5.9a. This is somewhat undesirable as it causes uneven flow distribution in the channel at local regions where liquid water is present. More than that, blocking the channel by water drops is a negative effect as it happens in a single cell of a serial-connection fuel cell stack since each single cell performance plays an important role in contributing to the stack performance. In contrary to the channel, it can be seen in Figure 5.9b that the flow field is less affected by the liquid water

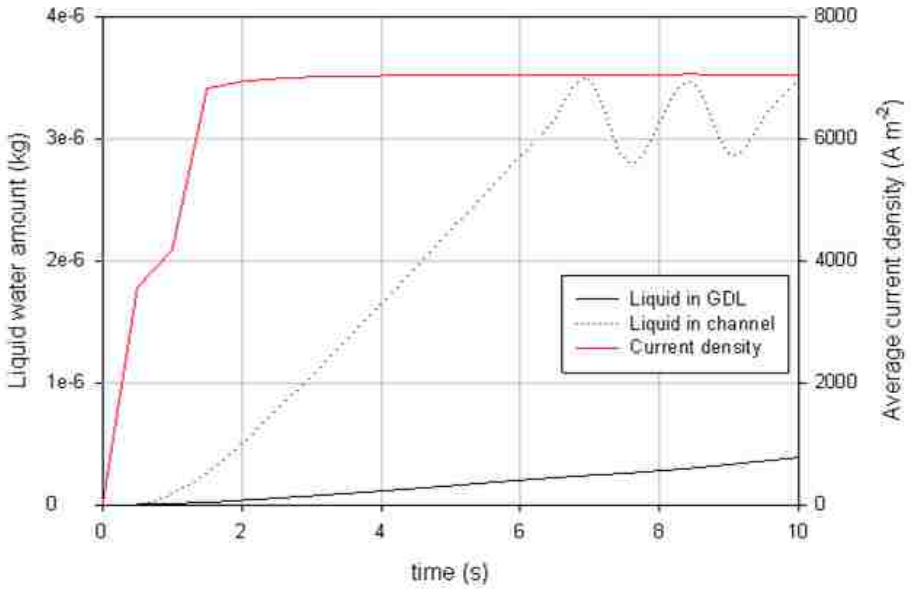


Figure 5.8: Liquid water amount in the cathode channel, GDL and average current density variations with respect to time

in the porous media because the volume fraction of liquid in the porous media is usually not as high as in the channel and the velocity of flow field in the porous media is much lower than in the channel due to its high flow resistance. Another effect of liquid water on the flow field is considered to be an increase in pressure distribution on the locations where liquid water takes places as shown in Figure 5.9c and Figure 5.9d. Hence, it would create more energy loss since the pressure increase has to be overcome by using compressors or blowers.

**Effect of liquid water on species transports**

Figure 5.10 indicates that the oxygen mass fraction reduces along the channel from the inlet to the outlet as a result of oxygen consumption due to the reactions in the cathode catalyst layers. More importantly, the contours of oxygen mass fraction represented in Figure 5.10 obviously show how the oxygen transport is hindered by liquid water. It is realized that the oxygen transport limitation in the channel is more considerable than that in the GDL. Similar to flow field distribution, this can be explained by volume fraction of liquid when its presence in the channel is much more than in the porous media. Moreover, this also can elucidate that although there is liquid water in the membrane that may block the mass transport of reactant gas, it would not affect much the fuel cell performance by degrading the local current density generated from the reaction. In contrary, the local current density can be increased due to a high ionic conductivity of the membrane when liquid water appears. This conclusion will be described in the next section. Before moving to the next, let see how the water mass fraction is increased under the presence of liquid water in the cathode channel and

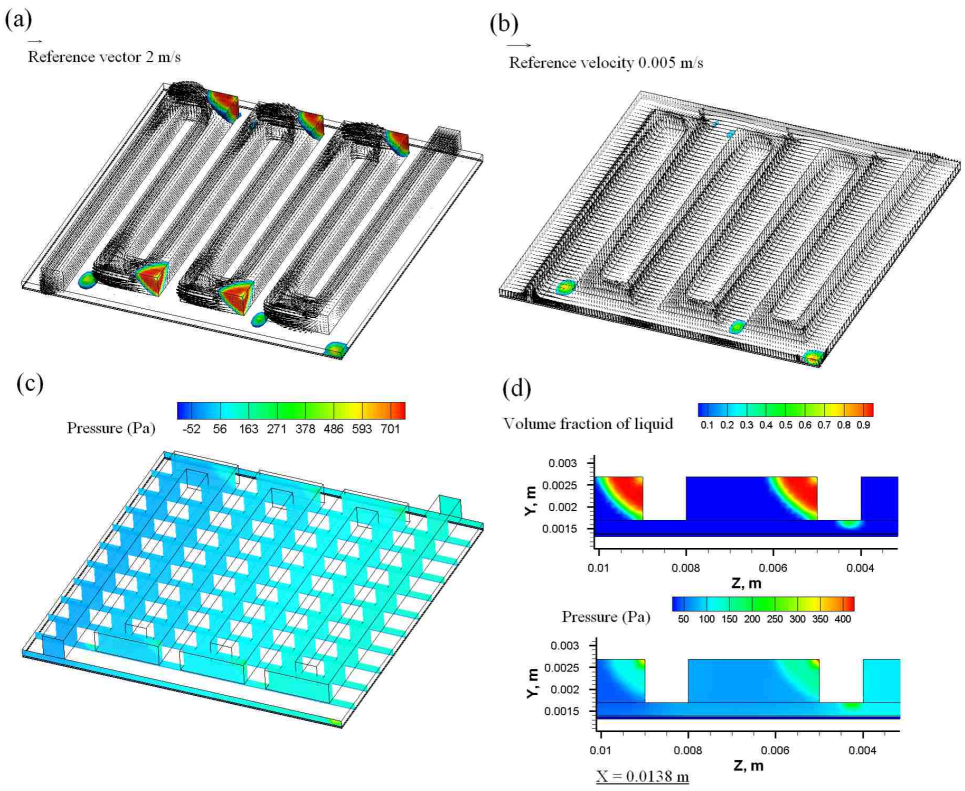


Figure 5.9: Volume fraction of liquid, velocity and pressure distributions on the cathode channel and porous media at t = 4.50 s

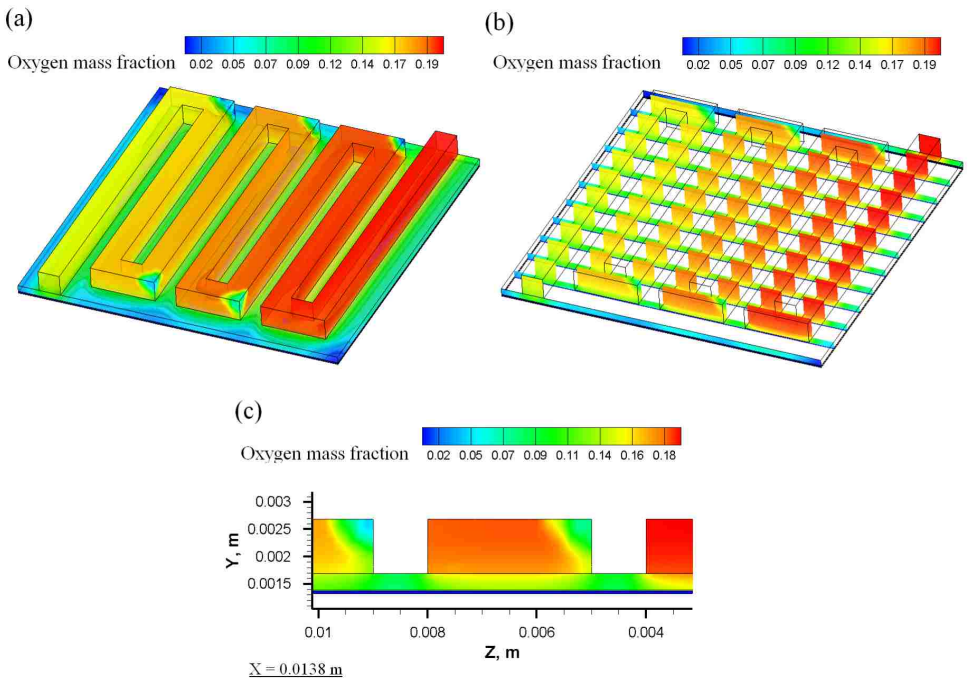


Figure 5.10: Oxygen mass fraction distribution on the cathode channel and porous media at t = 4.50 s

porous media in Figure 5.11. Note that both vapor and liquid phases are considered in water mass fraction calculation. Hence, the presence of liquid would much increase water mass fraction if its volume fraction values are large.

**Effect of liquid water on local current density**

It is known that liquid flooding is one of the main reasons causing degradation of the fuel cell performance. The liquid water in the fuel cell will block the oxygen transport from the channel to porous media and/or from the GDL to the catalyst layer where the reaction takes place. Since the reaction and reactant gas mass transport are inhibited, it leads to a reduction in local current density that is generated by the reaction. This conclusion seems to make sense. Figure 5.12a and Figure 5.12b shows the current density distributions in the membrane in two cases at $t = 4.5\ s$: one case considers the liquid water and another case does not consider the liquid water. It indicates that the local current density in the membrane where liquid drops are present is much higher than at the location without the presence of liquid water. The question is how the presence of liquid water positively influences the local current density although it may inhibit the mass transport of reactant gas and the reaction as mentioned above. To answer this question, first recall that water is necessary to be in the membrane. The ionic conductivity of the membrane is a function of the water content and it is proportional to the water concentration. The higher the water content in the membrane, the larger local current density is obtained. It can be seen in Figure 5.12c and Figure 5.12d that the locations that liquid

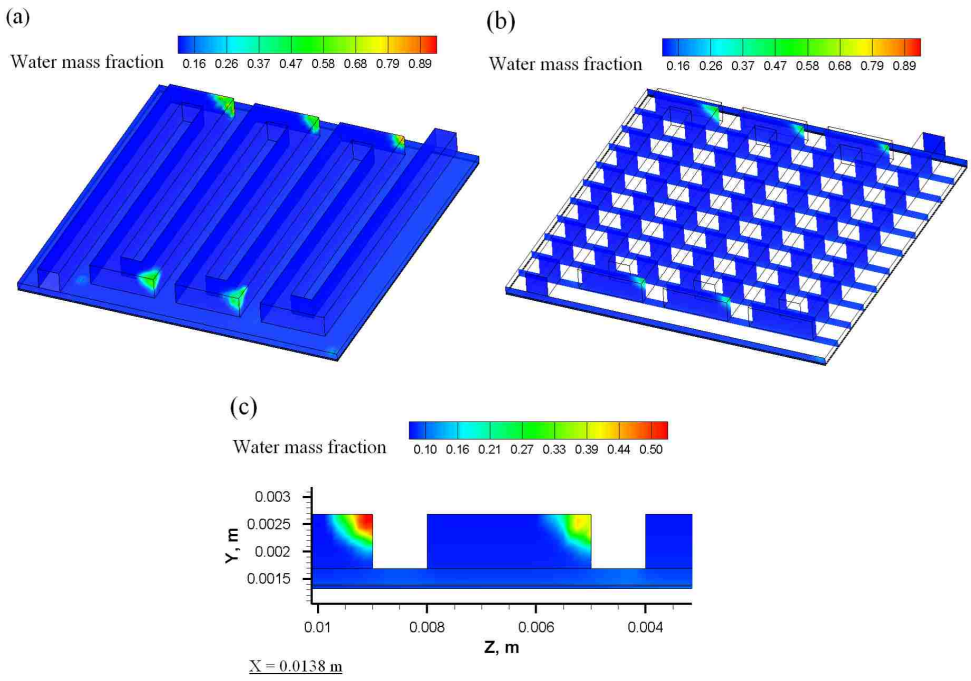


Figure 5.11: Water mass fraction distribution on the cathode channel and porous media at t = 4.50 s

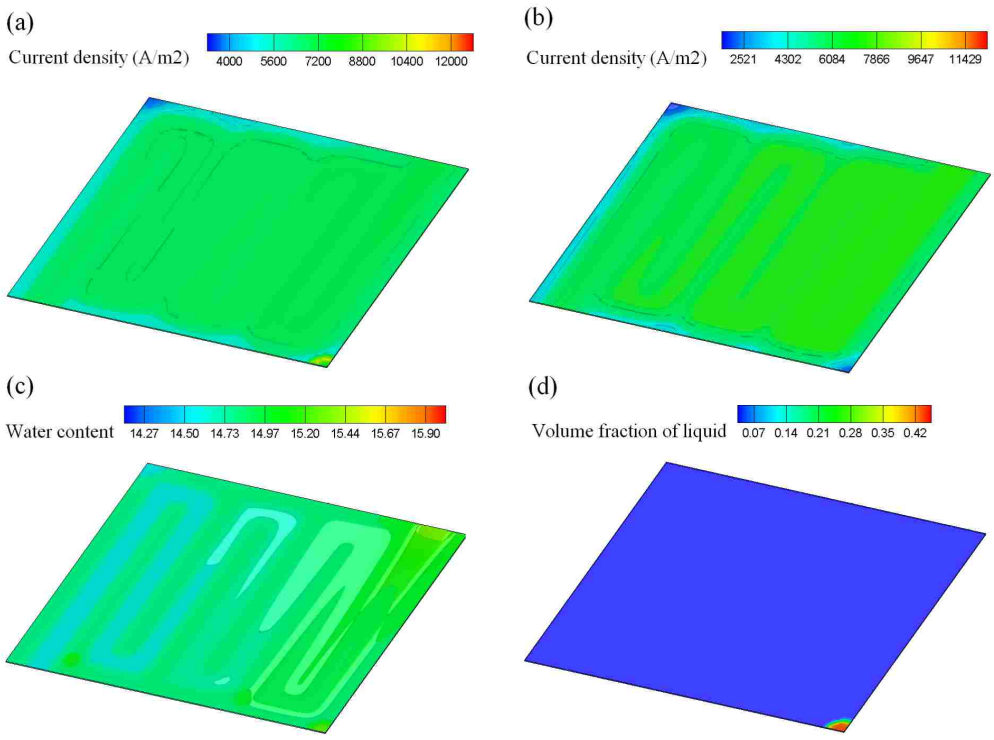


Figure 5.12: Current density distribution on the membrane at t = 4.50 s

water is present usually have higher values of water content, and in other words, they contain higher values of current density. Second, it is observed that the maximum value of liquid volume fraction distributed in the membrane and cathode catalyst layer is around 0.5 and there are at least values at 0.5 of volume fraction of gas mixture remaining in such locations. If the gas mixture including oxygen is in there, the reaction can still go on and continue to generate the current density. This explains why the current density in a certain location is available although the location may be occupied by an amount of liquid water in terms of drops or droplets. It will completely stop the reaction and mostly block the mass transport as the pure liquid water or liquid water indicated by large volume fraction takes place. Then the local current density is insignificant or reaches zero value. This conclusion was demonstrated in chapter 4.

### 5.3.4 Phase change in the PEMFC

Phase change of water, namely water condensation and evaporation processes, is main mechanism for liquid water formation and flooding occurring in PEMFCs. By incorporating the phase change, liquid water formation in the PEMFC was examined in previous sections. The characteristics of phase change are described here by presenting the phase change rate that was defined in Eq. 3.49. Due to unsteady state of this model, contours of the phase change rate in the PEM fuel cell shown in Figure 5.13 is taken at $t = 4.5\ s$.

The positive value of phase change rate denotes water phase change is from vapor to liquid (water condensation) and the negative value means phase change is from liquid to vapor (water evaporation). It indicates that evaporation will take places if the liquid water exists, especially in the positions of liquid drops in the channel. The more positively phase change rate is, the more strongly the condensation occurs. In the other hand, condensation is observed in the vapor phase region. However, the phase change rates of the two processes (condensation and evaporation) are significantly different: the rates of condensation are higher than the rates of evaporation in terms of magnitude. It means that at $t = 4.5\ s$, water condensation is dominant in the fuel cell. In addition, the phase equilibrium can be understood by presenting volume fraction of liquid. If the volume fraction of liquid in a drop is high, then it tends to evaporation. In contrary, if the drop has a low value of liquid volume fraction, phase equilibrium will shift to condensation.

The contours of phase change rates presented in Figure 5.13 show that convection also influences on phase change: the condensation in the region having strong flow field - such as the center line region of the channel - takes place slowly. Other factors affecting phase change are temperature and water vapor pressure as they are taken into account in Eq. 3.49. Intuitively, a location with cooler temperature and higher water vapor pressure (water concentration) let the condensation occur faster and vice versa. However, to fully examine the effects of such physical parameters on characteristics and mechanism of phase change under various operating conditions and material properties, it needs to investigate the phase change at different instants of operation and different fuel cell operating conditions. Due to length limitation of this present paper, the elaborated study on this work will be presented by our group in the next research publications.

## 5.4 Conclusions

In this chapter, the formation, motion and removal of liquid water has been numerically visualized in a 3-D mathematical PEMFC model by using VOF method incorporated with phase change process. The overview pictures of water liquid transport in a real-time operation in the first 10 seconds of the PEMFC are described as in the following stages: the formation, growth and removal of the water liquid in the channels and porous media. The numerical results show that the removal of liquid water from the GDLs to the channel is due to convection of the flow field in the porous media. The liquid amount in the cathode channel fluctuates after its linear increment because there are repeated accumulation and removal of the liquid water in the channel: liquid water accumulation due to condensation and liquid water removal due to air flow convection. The presence of liquid water hinders the mass transport of reactant gas, resulting in a decrease of current density since two cases: with and without liquid water are simulated and compared. The model results also suggest that the phase change rate is an important factor to investigate the characteristic and mechanism of phase change and liquid water transport in PEMFCs.

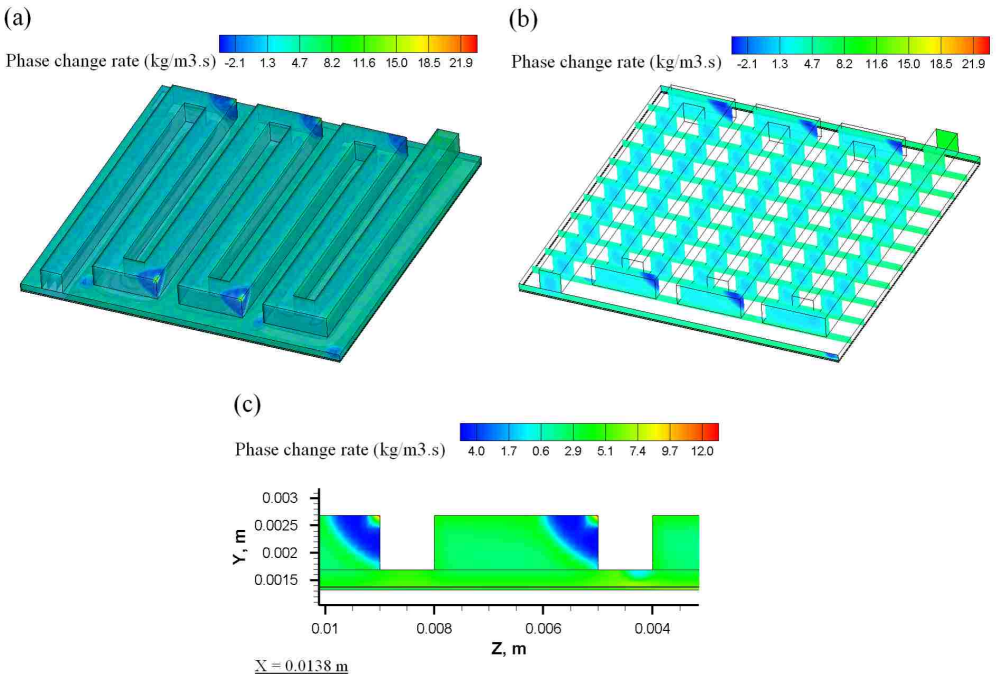


Figure 5.13: Contours of phase change rate on the cathode channel and porous media at t = 4.50 s

# Chapter 6

# Numerical Studies of Transport Phenomena in a PEM Fuel Cell Stack

## 6.1 Fuel cell stack A basic concept and issues

The theoretical potential of a single PEMFC is about one volt and the actual potential is possibly smaller than one volt. To generate more current and voltage that are suitable for practical applications in industry and transportation, single fuel cells are stacked. By electrically connecting the single cells in series and/or parallel, the voltage and/or current of a stack will be multiplied, generating the required the high power output. This way is simple, however, connecting single cells into a fuel cell stack definitely leads to an increase of size and weight of the fuel cell, resulting in some very important issues in stack design such as the distribution of reactant gas flow through the channels of the single cells and by-products water exhaust through the manifold, heat transfer and removal, water management of the stack, etc. In fact, one of the key requirements for a fuel cell stack design, according to [82], is uniform distribution of reactants to each single cell and inside each single cell. In other words, uneven distribution in flow field and reactant concentration would result in uneven performance among the single cells in a stack. The unevenness may be overcome by having appropriate manifold and flow channel designs to obtain uniform flow distribution. The shape of the flow field, flow field orientation, the configuration of channels can be calculated by simple methods. On the other hand, the presence of liquid water in a certain location of a certain single cell or a number of cells would significantly affect the flow distribution as well since liquid water blocks the flow field and hinders the reactant concentration in the flow channel and porous media. The presence of liquid and the mechanism of liquid water transport in fuel cell stacks are quite complicated and difficult to predict. Furthermore, this problem can only be solved by effective simulation tools in addition to proper design flow field and channel configuration of fuel cell stack.

## 6.2 The application of the numerical simulation on liquid water transport to a fuel cell stack model

Although a large number of researches on single PEMFC model have been published, only few studies have focused on the modeling of fuel cell stack. Modeling a fuel cell stack with complex geometry at adequate grid solution and calculation time is still a big challenge. Although a large number in such studies nearly focuses on investigating dynamic response and dynamic behaviors of PEMFCs, the models that consider simulations of physical and electrochemical phenomena and flow-field, heat and mass transports characteristics of a PEMFC have been rarely discussed [83, 84, 85, 86, 87, 88]. However, these numerical models have not dealt with liquid water transport which is still a challenge to the management of flow field and reactant distributions. Hence, the general numerical PEMFC model used for single PEMFCs mentioned in the previous chapters is also applied for PEMFC stack model with various boundary conditions for the overall stack. By simulating the liquid water transport and predicting the presence of liquid water and water flooding in the channels and porous media, the numerical results would elucidate how liquid drops influence physical and transport characteristics of each single cell in the stack and how performance of each single cell impacts the stack performance.

## 6.3 Computational domain and boundary conditions

The fuel cell stack comprises of three single PEMFCs numbered from top to bottom, connected in serial with parallel-designed channel used for each single cell as shown in Figure 6.1. The width and height of the channels are identical and are 1 mm. The channel inlets and outlets of the three single cells are connected to the gas inlets and outlets by the manifolds. The computation domain includes current collectors, middle bipolar plates, flow channels, gas diffusion layers (GDLs), catalyst layers, proton exchange membranes and manifolds. The computational mesh contains 399,650 hexahedral grid cells and is implemented by Gambit 2.3 mesh generation software. The boundary conditions for physical parameters applied on a fuel cell stack are described in Section 3.6.

## 6.4 Results and discussion

As discussed in Section 4.1, liquid droplet injection is necessary to examine the effects of liquid transport on flow field behavior, species and charge transport since the computation of VOF method is temporally expensive. In this stack model, the droplets were added into the cathode channel of each individual cell at $t = 1\ s$ and as the time progresses, the numerical results of simulation for all parameters are obtained at $t = 3\ s$. Geometrical properties and physical parameters of the stack are listed in Table 6.1. The three different cases corresponding to different locations of droplet addition are listed in Table 6.2 and Figure 6.2.

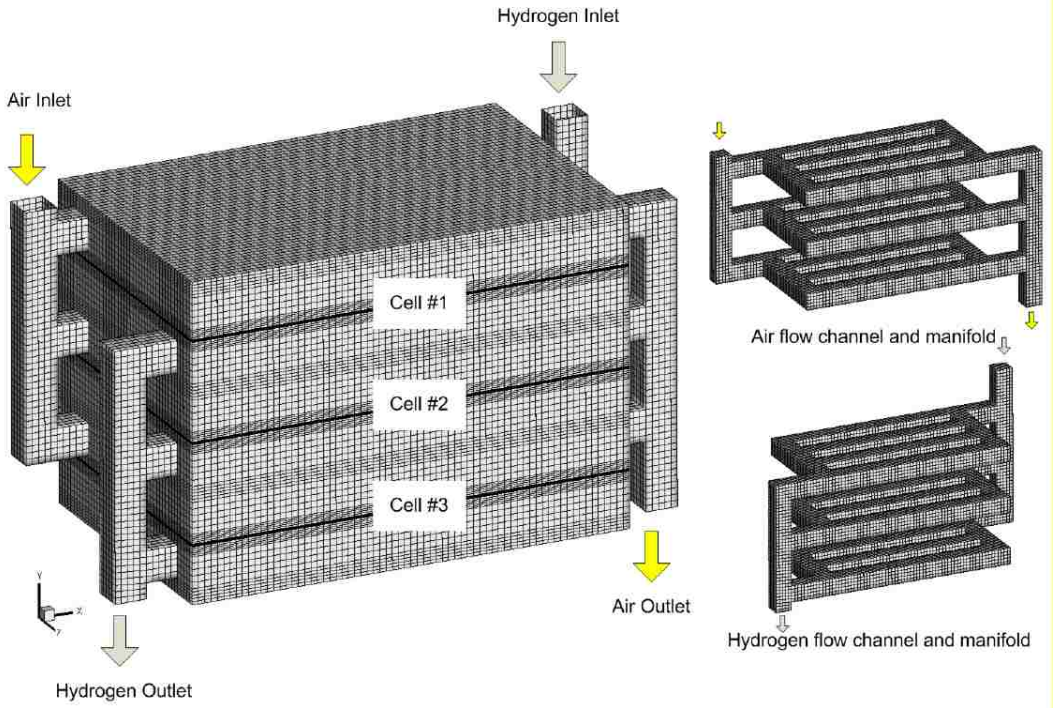


Figure 6.1: Schematic diagram and computational domain of the fuel cell stack

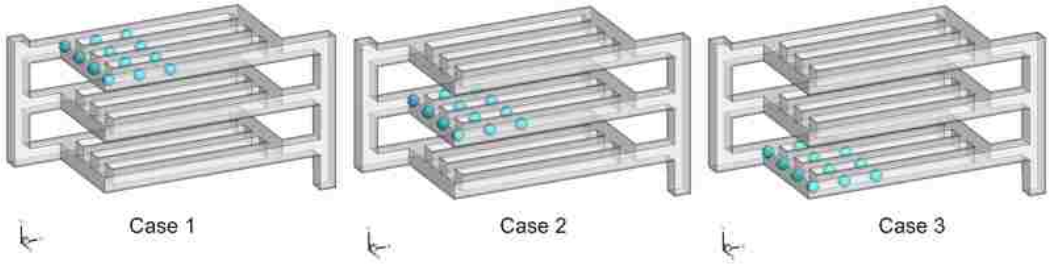


Figure 6.2: Three different cases for different locations of droplet addition at t = 1 s

Table 6.1: Geometrical properties and physical parameters of the fuel cell stack

| **Parameters** | **Value** |
|---|---|
| Anode channel width | 0.001 m |
| Anode channel height | 0.001 m |
| Cathode channel width | 0.001 m |
| Cathode channel height | 0.001 m |
| Manifold width | 0.001 m |
| Manifold height | 0.001 m |
| Membrane thickness | $50 \times 10^{-6}$ m |
| GDL thickness | $300 \times 10^{-6}$ m |
| Catalyst layer thickness | $20 \times 10^{-6}$ m |
| Active surface area (per one single cell) | $1.26 \times 10^{-4}$ $m^2$ |
| Number of single fuel cell in stack | 3 |
| Stack height, Y-coordinate | $1.007 \times 10^{-2}$ m |
| Stack length, X-coordinate | $1.6 \times 10^{-2}$ m |
| Stack width, Z-coordinate | $0.9 \times 10^{-2}$ m |
| Anode inlet excess coefficient | 4 |
| Cathode inlet excess coefficient | 1.25 |
| Operating voltage | 1.80 V |
| Anode Inlet Temperature | 300 K |
| Cathode Inlet Temperature | 300 K |
| Anode volumetric reference exchange current density /Reference hydrogen concentration | $7 \times 10^{10}$ A $kmol^{-1}$ |
| Cathode volumetric reference exchange current density /Reference oxygen concentration | $7 \times 10^{5}$ A $kmol^{-1}$ |
| Anode transfer coefficient | 0.5 |
| Cathode transfer coefficient | 0.5 |
| Anode concentration dependence | 0.5 |
| Cathode concentration dependence | 1.0 |
| Factor accounts for energy release | 0.5 |
| Membrane porosity | 0.5 |
| Diffusion layer porosity | 0.5 |
| Catalyst layer porosity | 0.5 |
| Permeability of porous media | $1.76 \times 10^{-11}$ $m^2$ |
| Contact angle | $70^{\circ}$ |
| Surface tension | 0.065 N $m^{-1}$ |
| Condensation rate | 100 $s^{-1}$ |

Table 6.2: Three different cases for different locations of droplet addition

| Case No. | Location of droplets | Number of droplets | Time of addition (s) |
|---|---|---|---|
| 1 | Cell 1 Cathode channel | 12 | at 1s |
| 2 | Cell 2 Cathode channel | 12 | at 1s |
| 3 | Cell 3 Cathode channel | 12 | at 1s |

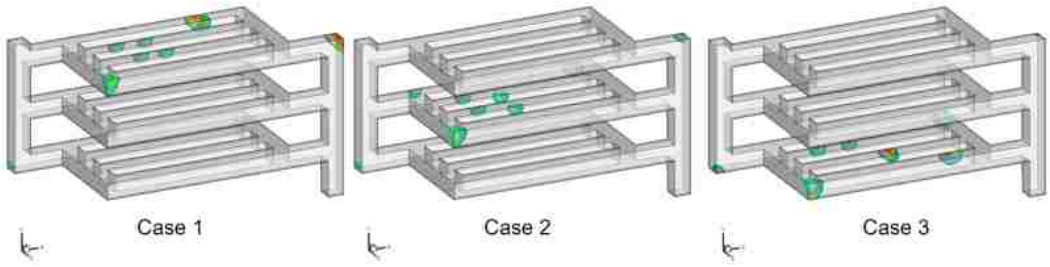


Figure 6.3: Three different cases for different locations of droplet addition at t = 3 s

### 6.4.1 Liquid water distribution in the air channel of three cases at t = 3 s

Figure 6.3 shows the liquid droplets distribution in the cathode flow channel of three single cells in the stack after a time interval of 2 seconds. In Chapters 4 and 5, we have thoroughly presented and commented the liquid water transport in the channels by various different time intervals. In this section, however, the droplets information at 3 seconds in a fuel cell stack at different cells is briefly reintroduced to facilitate the analysis on the effects of liquid water to fluid flow and species distribution characteristics of the single cells in the stack.

### 6.4.2 Pressure and flow field distribution in the cathode channel of three cases at t = 3 s

Figure 6.4 shows the distribution of pressure and flow field under the presence of liquid water in the channels in different cells. It could be observed that liquid droplets taking place in a channel of a cell will locally cause an the uneven distribution of pressure and flow field in this channel. First, one can notice that the pressure drop across the surface of droplets is relatively high compared with the pressure difference in the channel. Second, in the case of straight-parallel channel, since pressure drop along a channel is nearly the pressure drop in the entire flow field, the liquid droplets blocking a channel plays a role as a resistance, causing a decrease of the velocity or flow rate through the channel.

Regarding the straight-parallel channel, the numerical results show that this design ensures the distribution of flow field and pressure drop are more uniform than other channel designs (as shown in Figure 6.4: there is no significant change of flow velocity under the presence of liquid droplets). However, the straight-parallel channel may not be suitable to remove the liquid droplets from the channel as observed in the figure.

### 6.4.3 Species transport distribution in the channels and catalyst layers of three cases at t = 3 s

In Figure 6.5 and Figure 6.6, the mass fraction distributions of oxygen and water in the cathode channel and catalyst layer of three cases are shown. The distributions illustrate that the oxygen transport is hindered

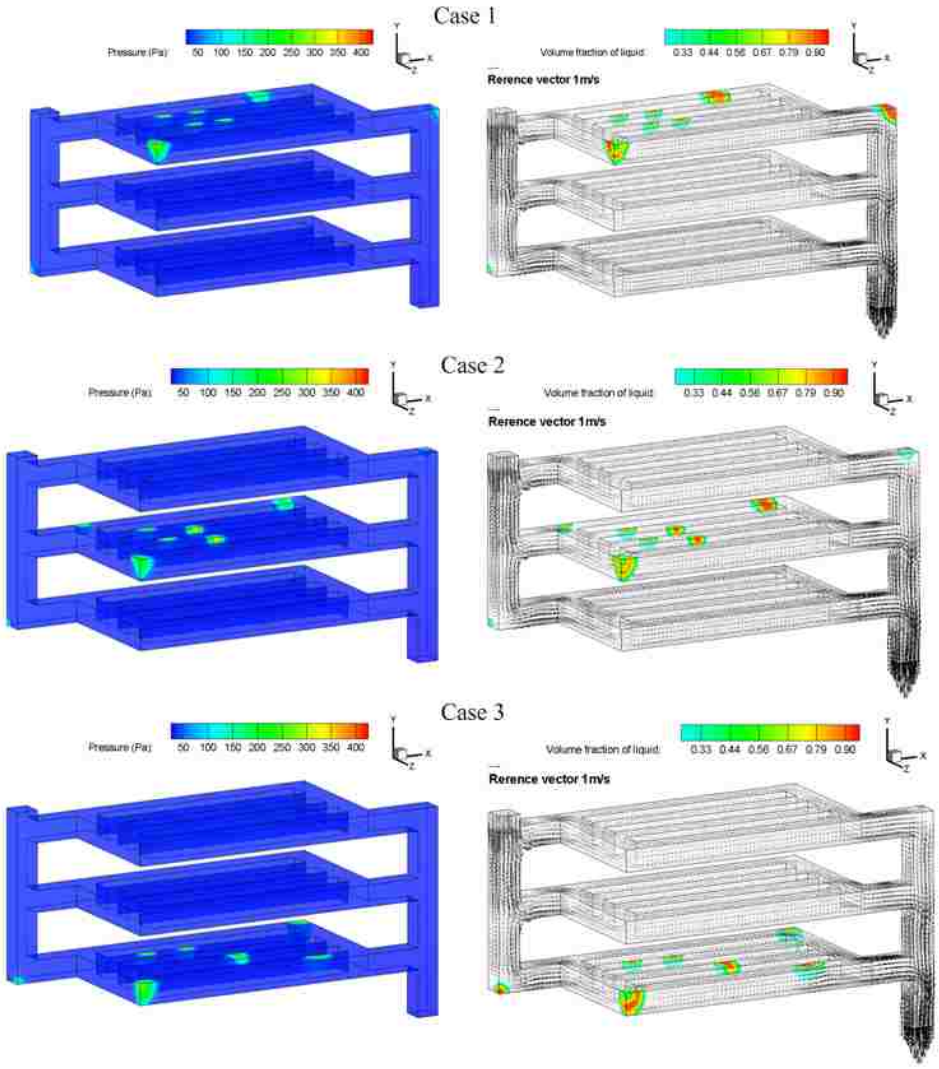


Figure 6.4: Pressure and velocity distributions in the air channel of three cases at t = 3 s

by liquid droplets locating in the channel. As shown in Case 1, at the top of the cathode channel (of Cell 1) a number of droplets placed that prevents the mass transport of oxygen, leading to a low concentration of oxygen if compared with the oxygen concentrations at the same channel in other two cases. Similar to Case 1, Case 2 and Case 3 show low concentration distributions of oxygen at the middle channel and the bottom channel where the liquid water takes place, respectively. Of courses, a low oxygen distribution in the channel would result in a small amount of oxygen concentrated in the catalyst layer in the same cell. It also causes a low current density distribution if the cell contains a large amount of liquid water, since the concentration distribution of oxygen is proportional to the reaction rate.

On the other hand, regarding the distribution of water in the cathode channel, the phenomenon is the opposite. Because the liquid water is in the same species with water vapor, the water distribution shown in Figure 6.6 denotes mass fraction distribution of water regardless of liquid or vapor phase. Note that although the phase change of water is taken into account in this model, the amount of water at a location is unchanged. Thus, once liquid water is located in the channel of a certain single cell, the water distribution becomes high, especially at the locations where the liquid droplets are present.

Figure 6.7 depicts the water fraction distributions in the anode channel and catalyst layer of three cases. Note that the liquid water was not present in the anode by adding droplets from $t = 0\ s$ as in the cathode, the species mass fractions in the anode, however, are still affected by the distributions of reactant gas in the cathode where the liquid water located. Let's explain this comment according to Case 1 shown in Figure 6.7 for water mass fraction. One can easily see that the water mass fraction in the anode channel of the cell 1 is higher than that in the cell 2 and cell 3. Corresponding to this distribution, the water mass fraction in the cathode channel of the cell 1 is also higher than that in other cells as described above. This relation is explained by water transport through the membrane between the cathode and anode of the same cell in chapter 4 and 5. Thus, it can be concluded that the presence of liquid water in the cathode not only affects the water distribution in the cathode itself, but also influences the water distribution in the anode by water transport mechanism in a single cell. Moreover, as a consequence, the hydrogen fraction distribution is also altered corresponding to water distribution in the anode, as shown in Figure 6.8. Of course, in order to investigate the effects of liquid water in the single cells of a stack, the liquid water should be added into the anode and cathode as well. This idea will be implemented in the near future.

### 6.4.4 Potential and current density distributions in the stack of three cases at t = 3 s

With a fixed cell voltage of 1.8 V applied on the fuel cell stack, the voltage and current density distributed in each single cell and the stack will be calculated in the transient state. Here the current density distributions in the membrane of each cell at $t = 3\ s$ are presented to examine the effects of liquid water on the fuel cell performance. The uneven distribution of flow field and species concentration, as analysed above, that is caused by the presence of liquid is the main reason to cause uneven current density distribution. As shown in Figure 6.9, a degradation of current density occurs only at the cell containing the liquid water. This mechanism of the current density degradation was explained in details in the previous chapters and hence, it is briefly mentioned again in the stack model to support the demonstration of effects of liquid water on the

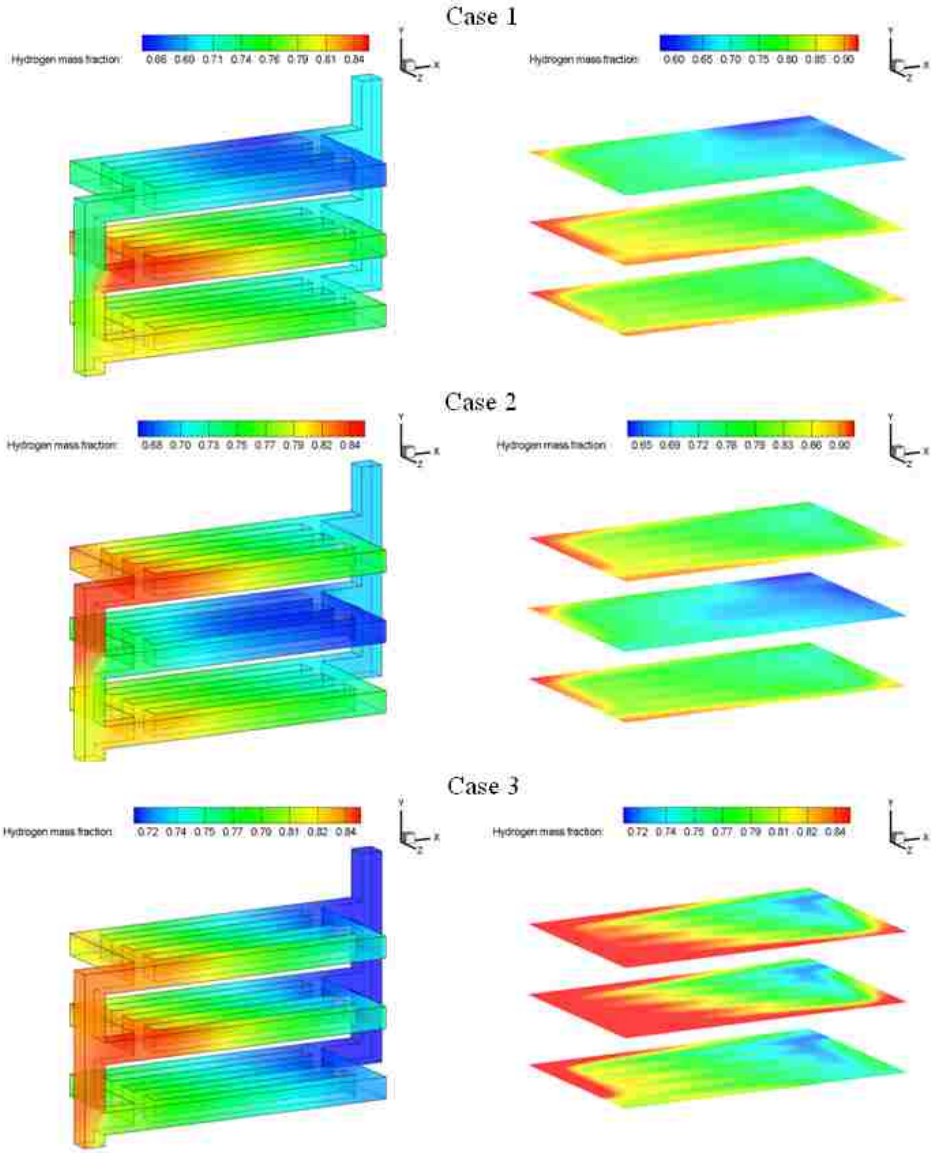


Figure 6.5: Oxygen distribution in the cathode channel and catalyst layer of three cases at t = 3 s

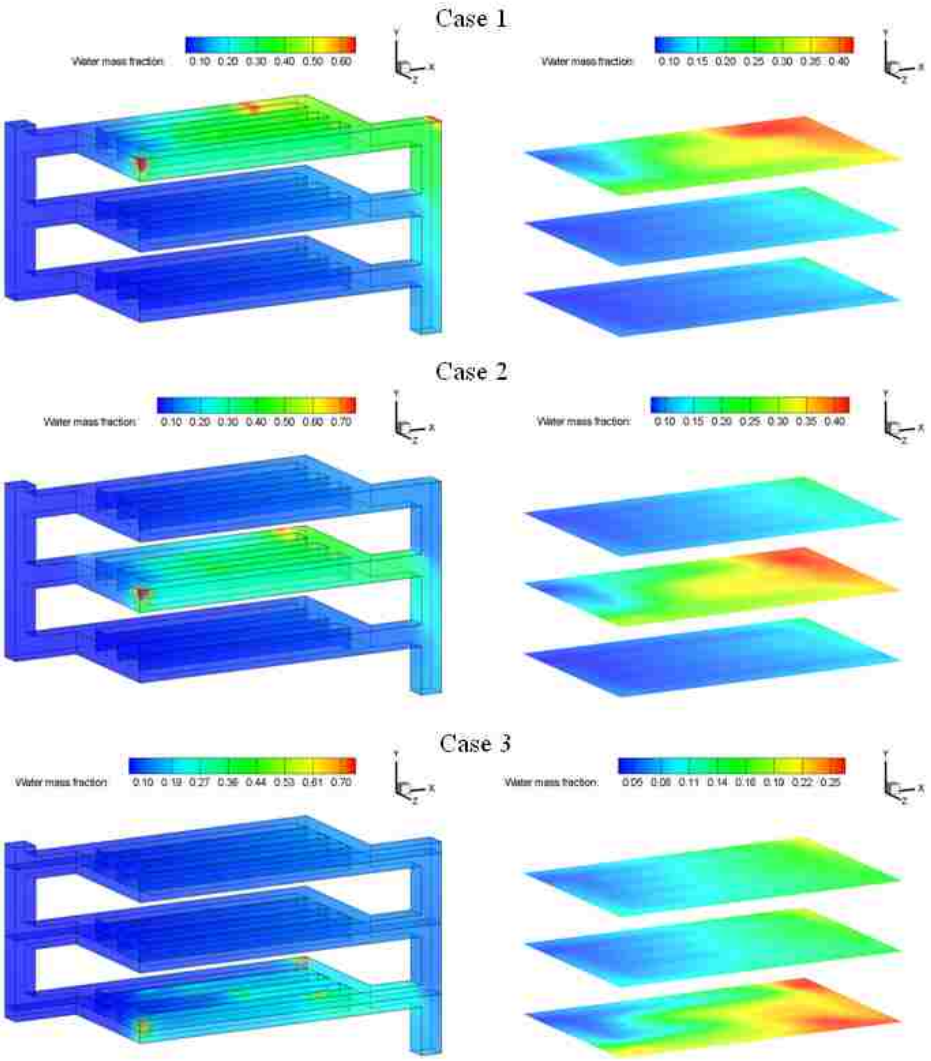


Figure 6.6: Water distribution in the cathode channel and catalyst layer of three cases at t = 3 s

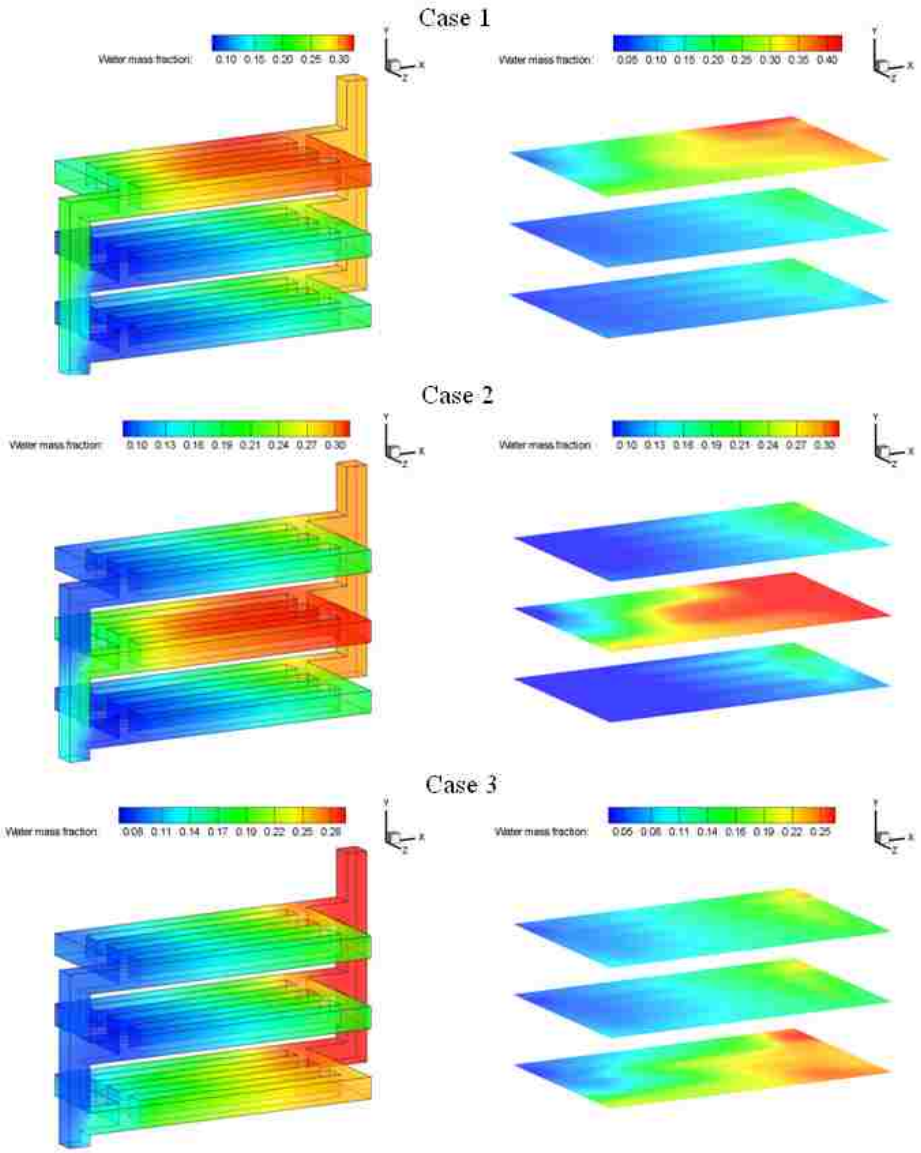


Figure 6.7: Water distribution in the anode channel and catalyst layer of three cases at t = 3 s

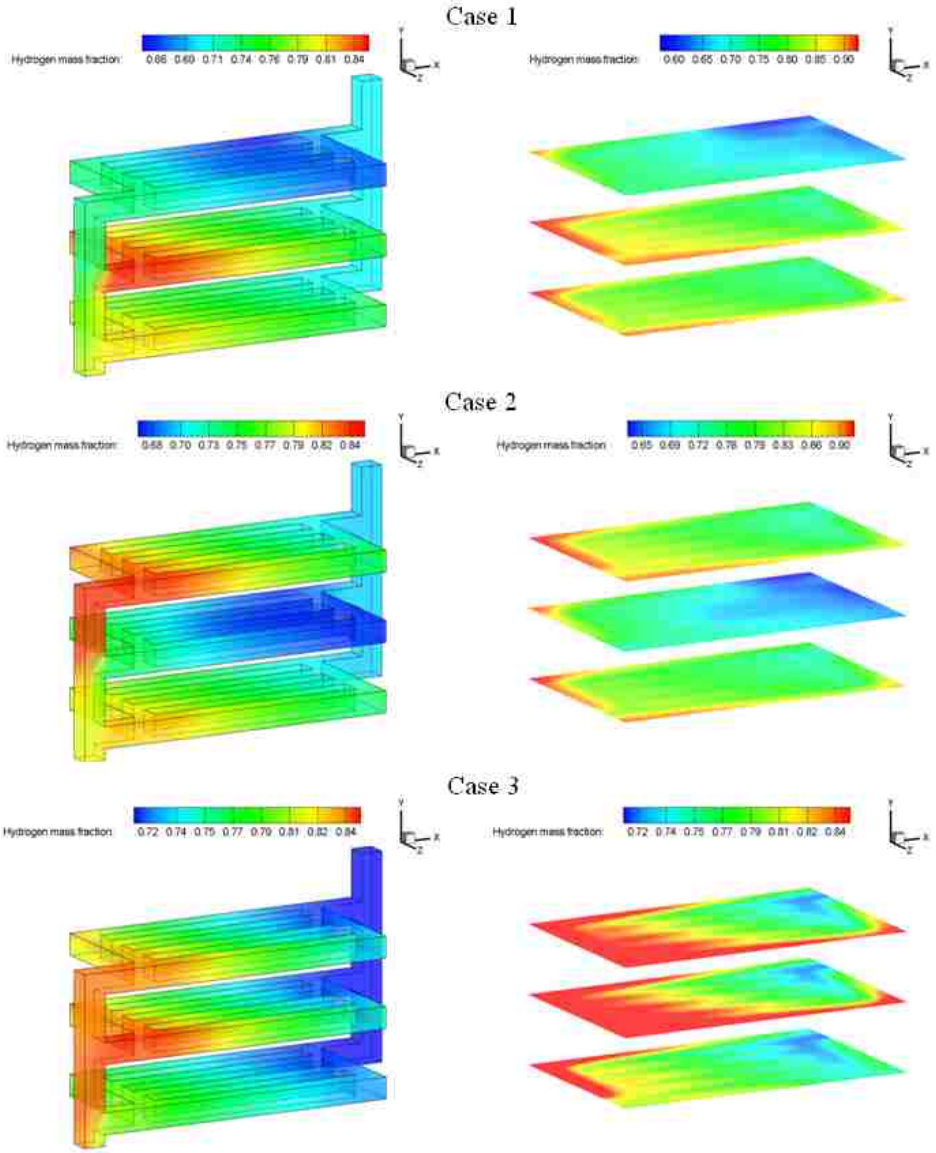


Figure 6.8: Hydrogen distribution in the anode channel and catalyst layer of three cases at t = 3 s

fuel cell performance. In Figure 6.9, however, the current density distribution in the flooding cell looks like smaller than in other cells containing no liquid water. For this matter, one can argue that the average current density in each cell in serial connection must be the same according to the charge conservation. The answer is that the numerical results are obtained at certain time in the transient state. Since the process reaches the steady state after few minutes, the current density in each cell will get the same value. In addition to the current density distribution, the voltages of each cell and the whole stack also achieved from the numerical model. The values of cell potential are approximately 0.6 V for every cell in the stack and this is quite reasonable.

## 6.5 Conclusions

In this chapter, the three-dimensional, multi-phase, VOF PEMFC model is also applied to a PEMFC stack to customize the governing, relative equations and their source terms that describe physical and electrochemical phenomena in a PEMFC stack. Numerical simulation is conducted in a PEFMC stack with three single cells connected in series. The numerical results show that the model can predict a number of important parameters such as flow field, species concentrations, temperature, voltage and current density distributions in all single cells of the stack under various operating conditions and design parameters. Similar to the application of the numerical model in a single PEMFC, the PEMFC stack model also considers the presence of liquid water inside the manifold, channels and porous media as well. The numerical results from three different cases of locating liquid droplets in different single cells indicate that it is an effective way to examine the flooding phenomenon in single cells and investigate how the presence of liquid water affects the single cell performance and how the performance of different single cells affects the fuel cell stack performance.

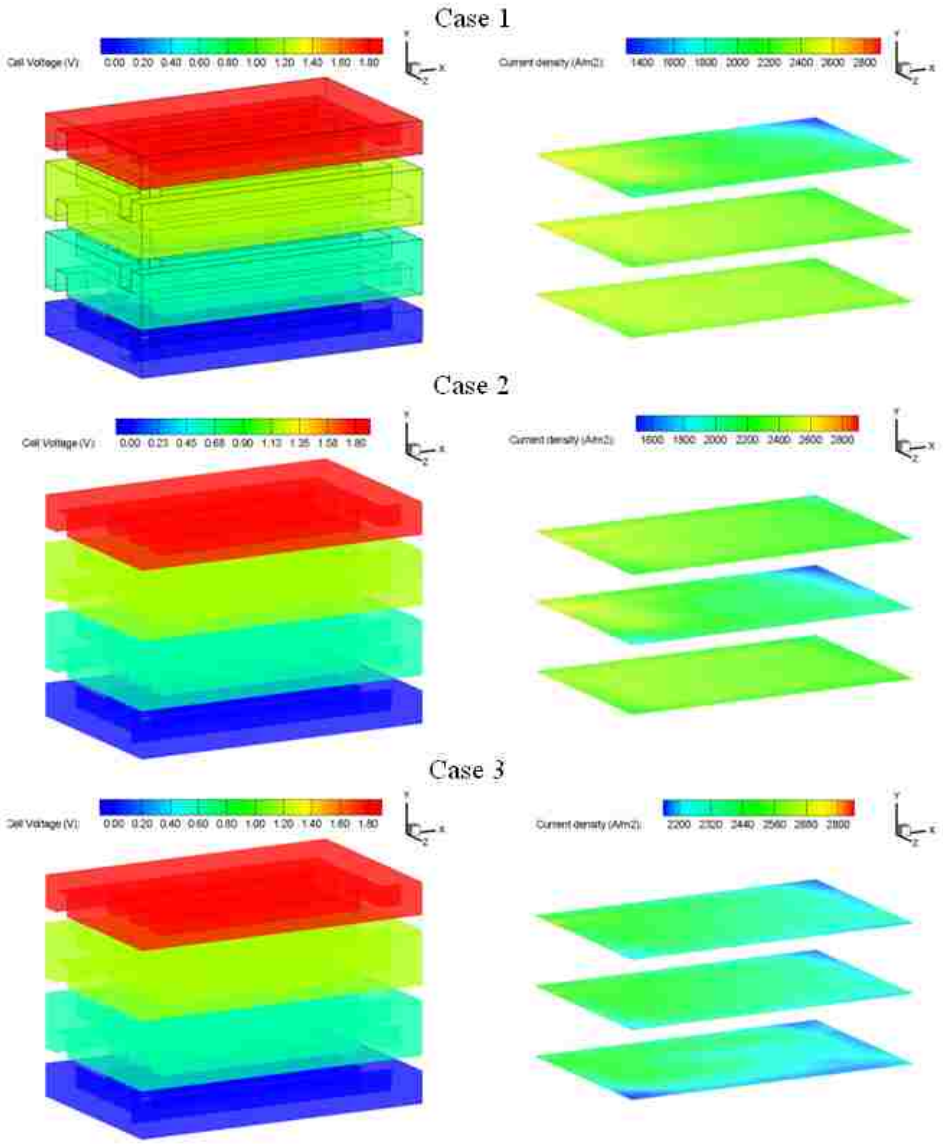


Figure 6.9: Potential and current density distributions in each single cell of three cases at t = 3 s

# Chapter 7

# Experimental Validation of Liquid Water Behavior in a PEMFC with Serpentine Channel

In addition to the numerical model, it is necessary to develop an experimental system that can visualize the motion and transport behavior of liquid droplets in the cathode flow channel of a single transparent PEM fuel cell. Moreover, the experimental data will be used to qualitatively and quantitatively validate the numerical results from the simulation model, especially VOF numerical method. The experimental visualization techniques used in our work is direct optical visualization since it is a powerful tool to capture the droplets motion and liquid water distribution with its advantages of high spatial and temporal resolutions.

## 7.1 Description of experimental devices and setup

The experimental system comprises of a transparent PEM fuel cell cathode, a fuel cell test bench (including air supply tanks, flow controllers, flow and pressure transducers and data acquisition systems - DAQs) and a commercial camera supported with optical lenses and light source as shown in Figure 7.1.

The operation of the experimental system is described as follows: a series of liquid water droplet with various operating conditions of air flow is injected into the flow channel via liquid injector in order to visualize the temporal evolution of liquid transport process. The droplet motion and deformation are captured by the camera that will export the visualized data to the computer in terms of movie file. The operating conditions such as airflow rate are set in the flow controller via the control signal transferred from the computer via DAQ hardware. The output parameters such as inlet and outlet pressures are also obtained from the pressure transducers and monitored in the computer by using the self-developed code in LABVIEW software environment [89, 90]. The characteristic length of the experiment is the order of $\mu$-scale and the characteristic time scale has the order of micro seconds. Hence, the experimental visualization will focus on identifying the length

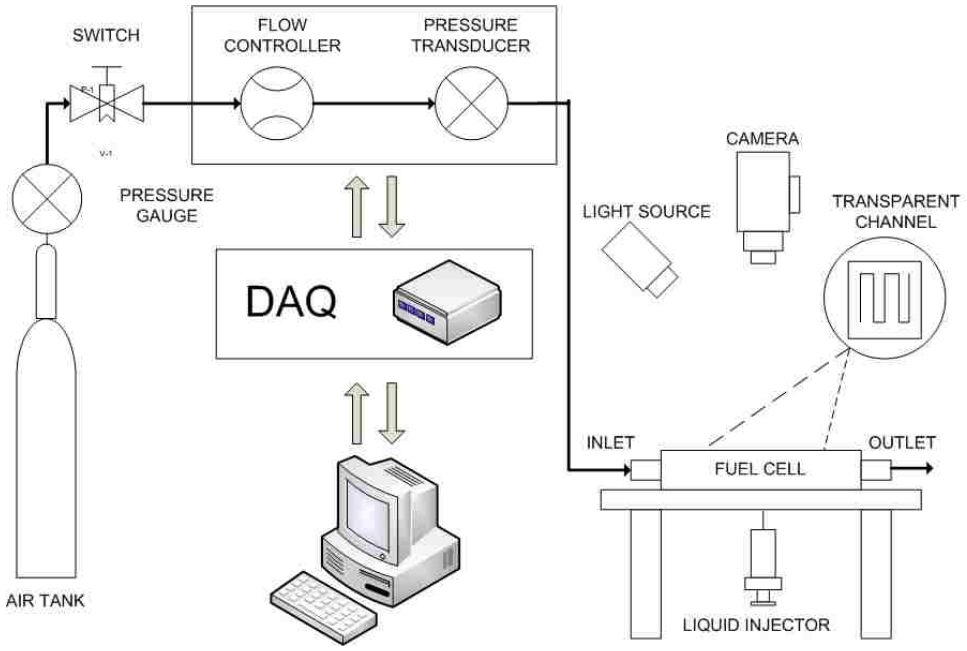


Figure 7.1: Schematic diagram of fuel cell experimental visualization system

and shapes of droplets and times characteristic of the liquid motion process to validate the numerical results.

### 7.1.1 Droplet generation

A number of droplets are consequently injected into the channel via the needle of a liquid injector that was placed under the fuel cell channel and porous media (MEA). By applying the force to the plunger, liquid water will be pushed out of the cylindrical tube on demand as shown in Figure 7.2. The fluid volume initially oscillates upon injection and creates the spherical droplets at the needle bit due to the minimization of interfacial energy (surface tension effect). The velocity and shape of the droplets are dependent on the frequency of the pulse force applied on the plunger, the diameter and size of the plunger, cylindrical tube and the needle, and the environment in which the droplets are created.

This experimental work uses the hypodermic needles with an inner diameter of 400 $\mu$m. The working fluid is dyed liquid water. The preliminary droplet created from the needle tip in atmospheric environment without convection (no airflow) has a maximum diameter of 3.4 mm (3400 $\mu$m) as calculated by volume method shown in Figure 7.3 and Table 7.1. In fact, the droplet diameter is smaller and different if it is created under a airflow with various velocities. As calculated according to the operating condition of the experiment, the droplet diameter is approximately 1 mm at airflow inlet velocity of 5.9 m/s.

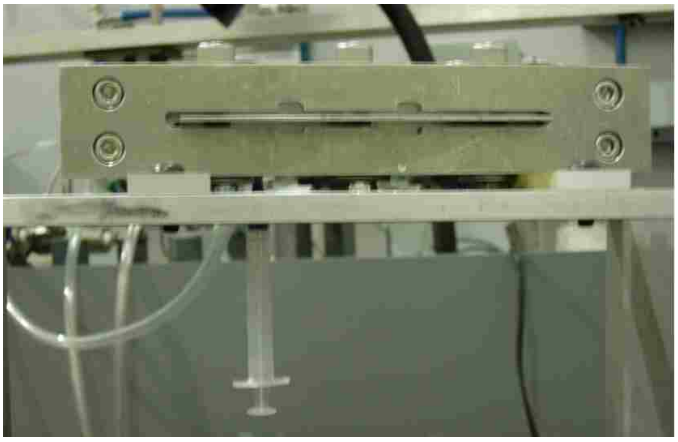

Figure 7.2: Droplet generation in the experimental visualization


Figure 7.3: Description of creating the droplets

Table 7.1: Calculation of droplet size

| No. of droplets | Capacity of container (ml) | Average amount of a droplet (ml) | Radius of a droplet (ml) | Diameter of a droplet (ml) | Air flow velocity (m/s) |
|---|---|---|---|---|---|
| 119 | 2.1 | 0.017647059 | 1.615081991 | 3.230163983 | 0 |
| 127 | 2.6 | 0.020472441 | 1.697046227 | 3.394092454 | 0 |
| 145 | 3.0 | 0.020689655 | 1.703027056 | 3.406054113 | 0 |

Table 7.2: The values of contact angle of the droplet

| Liquid type | Solid materials | Location of solid surface | Contact angle (°) |
|---|---|---|---|
| Dyed water | Glass | Transparent plate - up wall | 43 |
| Dyed water | MEA 12E-W | MEA - surface | 130 |
| Dyed water | Stainless steel | Collector/channel side wall | 53 |

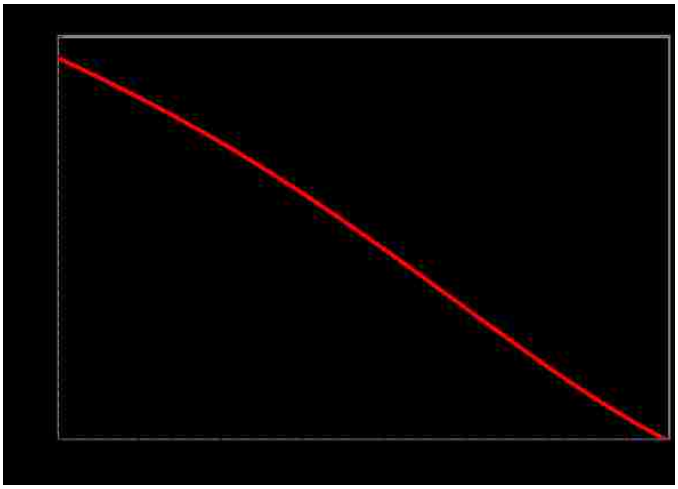

Figure 7.4: Surface tension of pure water as a function of temperature (Source from Internet)

### 7.1.2 Properties of the water droplet

**Contact angle of the droplet**

Contact angle that is one of the most important factors affects liquid transport in the fuel cell channel and porous media. By definition, contact angle is the angle at which a liquid/vapor interface meets the solid surface. Different types of liquid/gas interaction and different solid materials creates different contact angle. In this experiment, hence, we measured the contact angle of water drop in different solid materials used in the transparent fuel cell by a simple optical method. The values of contact angle at different materials are shown in Table 7.2.

**Surface tension**

Since the portion of the dye in liquid water is very insignificant (approximate 1 g/l), the surface tension of the droplet is considered to be the surface tension of liquid water measured at the operating temperature. From Figure 7.4, the value of surface tension at 20 °C is 0.072 $Nm^{-1}$.


(a) The serpentine flow channel

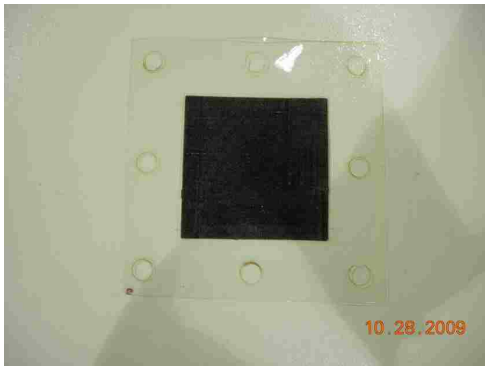


(b) Structure of the 12E-W MEA

Figure 7.5: Geometrical structure of the interdigitated PEMFC

**Viscosity**

The liquid water viscosity is chosen to be 0.001003 $kgm^{-1}s^{-1}$ at 25 °C. If the liquid water is dyed, the viscosity of dyed liquid water is slightly different. However, the difference can be negligible due to a very small amount of dye dissolved in the pure liquid solution.

### 7.1.3 Transparent fuel cell design [91]

The flow channel used in the experiment is serpentine (Figure 7.5a) and it is fabricated in a stainless steel plate with 1.7 mm thickness. The channel width is 2 mm and its total length is 180 mm. The plate is placed on a 12E-W MEA made by BASF®with an active area of 70 mm $\times$ 70 mm (Figure 7.5b). To capture the liquid water motion in the channel and connect the fuel cell cathode assembly, the steel plate and MEA are sandwiched between two plastic end plates and those are fixed by 8 bolts distributed around the plates' edges. The channel inlet is also connected to the air gas feed from fuel cell test band by a flexible hose and the channel outlet is vented to atmosphere.

### 7.1.4 Visualization method

As discussed in Chapter 2, the direct optical visualization method is used to capture the liquid motion and flow field behavior in a transparent object. For observing the flow field with velocities in the order of meters per second, this method is quite sensitive and has high spatial and temporal resolutions. In some cases, the high speed camera is required to record the pictures at an acquisition rate of thousand frames per second. The frame resolution, however, is inversely proportional to the frame rate and it may affect the quality of the recorded pictures.

In this experiment work, the time resolution is only required at a rate in the order of tens $\mu$s to obtain a number of pictures of liquid motion in a duration of few seconds that can be used to validate the numerical results. Thus, a commercial camera JVC GZ-MG 37 was utilized to visualize the liquid motion process. The

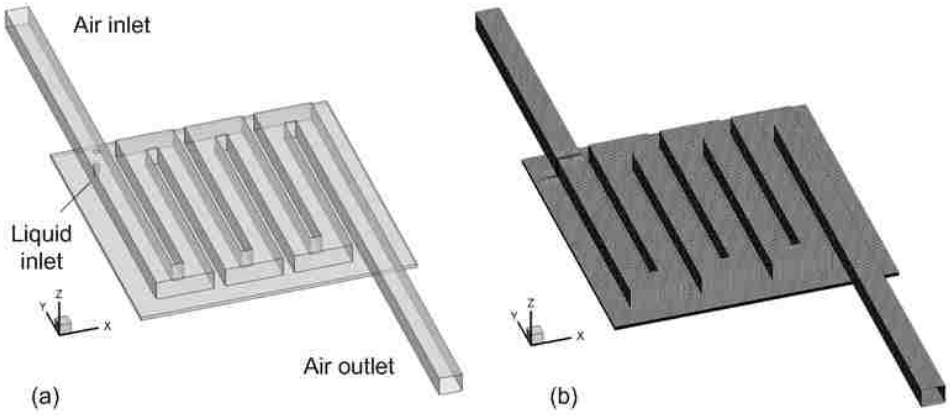


Figure 7.6: (a) Schematic diagram and (b) computational mesh of the numerical model.

obtained movie files are processed in the PC and exported to picture files with the frame rate of 30 frames per second (fps) or the time resolution of 1/30 seconds (approximate 34 $\mu$s). The frame resolution is 640 $\times$ 480. During the recording process, the microscope mode is employed to magnify the droplet images.

## 7.2 Description of numerical model setup

### 7.2.1 Computational domain and numerical procedure

The computational domain of the fuel cell used for the numerical model is setup as the same geometrical dimensions as the one used in the experiment that consists of the cathode MEA, flow channel and collector plate as shown in Figure 7.6. The computational grids are implemented by using Gambit 2.3 mesh generation software with a number of grid cells of 285,168 and it is solved using Fluent 6.3 software. The number of grids in the cross-sectional area of the channel is 12 $\times$ 12. The VOF algorithm was incorporated with flow field solver to investigate the liquid droplet behavior in the channel. The solution procedure for Pressure-Based Segregated Solver [73] incorporated with SIMPLE algorithm [81] is implemented in parallel computing and the iterations of each time step is set to converge when the residual criteria reach a value in the order of $10^{-4}$.

### 7.2.2 Validation of grid dependency

The grid dependency is examined in Chapter 4. It indicates that the grid resolution used in this work as described in the previous section is quite suitable enough to resolve the physical scales of the model and not does not affect much the calculation time. For this case, in addition, validation of grid dependency has been conducted to insure satisfactory accuracy in the numerical computations. The numerical results obtained from the different cases for different grid sizes were compared with the experimental data.

Table 7.3: Operating condition and physical properties of the experiment and numerical model

| Parameters | Value |
|---|---|
| Inlet gas flow-rate | $2 \times 10^{-5}$ kgs$^{-1}$ |
| Inlet liquid flow-rate | $1.65 \times 10^{-5}$ kgs$^{-1}$ |
| Operating temperature | 20 °C |
| Surface tension | 0.072 Nm$^{-1}$ |
| Contact angle of the transparent glass | 43° |
| Contact angle of the collector/channel plate | 53° |
| Contact angle of the MEA | 130° |
| Air viscosity at 20 °C | $1.7894 \times 10^{-5}$ kgm$^{-1}$s$^{-1}$ |
| Liquid water viscosity at 20 ∘C | 0.001003 kgm$^{-1}$s$^{-1}$ |

## 7.3 Results and discussion

### 7.3.1 Setup of operating condition and physical properties

To make comparison and validation between the experimental and numerical results, a case is setup for both the experiment and numerical model with the same operating conditions and physical properties of fluid flow and materials shown in Table 7.3.

To set the physical properties of fluid flow and materials, these parameters are measured from the experimental case and then are used for the numerical model. The inlet gas flow-rate is measured by flow-rate controller in the fuel cell test band. For the liquid flow-rate measurement, it is measured by "Bucket-and-stopwatch" method. By examining the volume of liquid water moving in the syringe by its displacement for a certain time period, the liquid flow-rate is measured from the experimental case.

### 7.3.2 Dimensionless number

To make a comparison between the experimental and numerical results and examine the physics of liquid flow dynamics under the same operating condition for both cases, the dimensionless numbers: Reynolds (*Re*) and Weber (*We*) numbers are determined as follows

*Reynolds number*: Reynolds number of the air flow represents the ratio of inertia force to viscosity force and is defined as,

$$\mathrm{Re} = \frac{UD_h}{\nu} \tag{7.1}$$

where U the air flow velocity, $D_h$ is the hydraulic diameter of channel and $\nu$ is the dynamic viscosity of air. Since the inlet velocity of air flow in the channel is 5 ms$^{-1}$ and the hydraulic diameter of the rectangle channel is 0.0018 m [92], Reynolds number is given as

$$\mathrm{Re} = \frac{5 \times 0.0018}{1.6 \times 10^{-5}} = 562.5 \tag{7.2}$$

*Weber number*: Weber number is considered as the ratio between inertia and surface tension. It explains how importantly the surface tension force affects the droplet behaviors. It can be expressed as,

$$\mathrm{We} = \frac{\rho V^2 L}{\sigma} \tag{7.3}$$

where V is the velocity of motion of the droplet (it is assumed to be the air velocity when the liquid is in motion in air flow field),$\rho$ is liquid water density, L is the characteristic length (the contact radius of droplet) and $\sigma$ is the surface tension.
*Bond number*: Bond number is defined as the ratio between the gravitational force and surface tension force.

$$\mathrm{Bo} = \frac{\Delta\rho g R^2}{\sigma} \tag{7.4}$$

### 7.3.3 Experimental and numerical visualizations of liquid water motion in the channel - Comparison and Analysis

#### Model comparison

Figure 7.7 shows the comparison between the experimental and numerical simulation results for liquid droplet motion in the serpentine channel of a fuel cell under the operating conditions listed in Table 7.3. The time evolution of visualization processes is taken within a second that is good enough to describe and investigate the liquid water motion and behavior at any instants from the beginning when liquid is injected into the channel to the end when liquid water is removed out of the channel by the air flow field. As shown in a series of Figure 7.7, it can be seen that the experimental visualization and numerical simulation provide results that have similarities in terms of the shapes of droplets and spatial-temporal position of liquid water in the channel.

#### Physics of the droplets and liquid motion behavior - Analysis and Discussions

The droplets are injected into the channel via the needle placed inside. When a drop appears at the needle point, it is deformed by shear force from the air flow field and has pendant shape. This drop is called pendant drop [93]. The shape of droplet is determined by the Weber number that is the ratio between inertia and surface tension. In other words, the inertia force tends to elongate the droplet along the flow direction while the surface tension force tends to minimize the interface by making the droplet spherical. Figure 7.8 shows the time evolution of the droplet deformation with Weber number and Bond number that are calculated as

$$\mathrm{We} = \frac{1000 \times 5^2 \times 0.0007}{0.072} = 243 \tag{7.5}$$

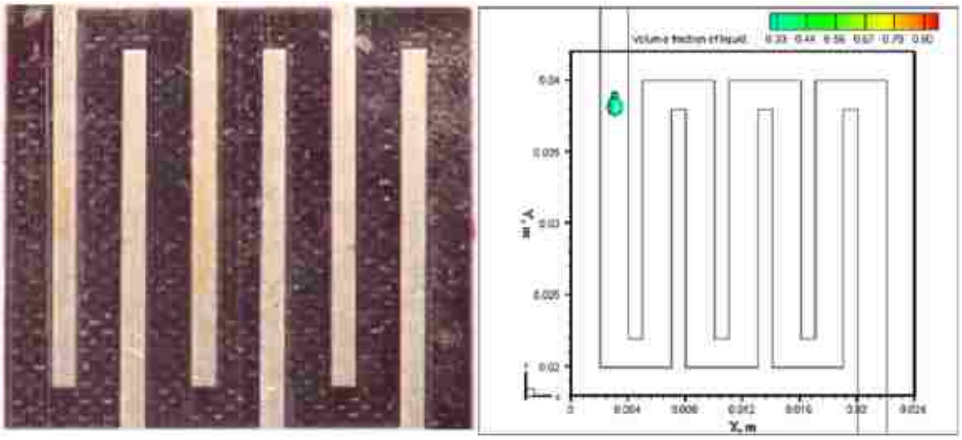

Figure 7.7a: Visualization of liquid motion in the channel at t = 0 s

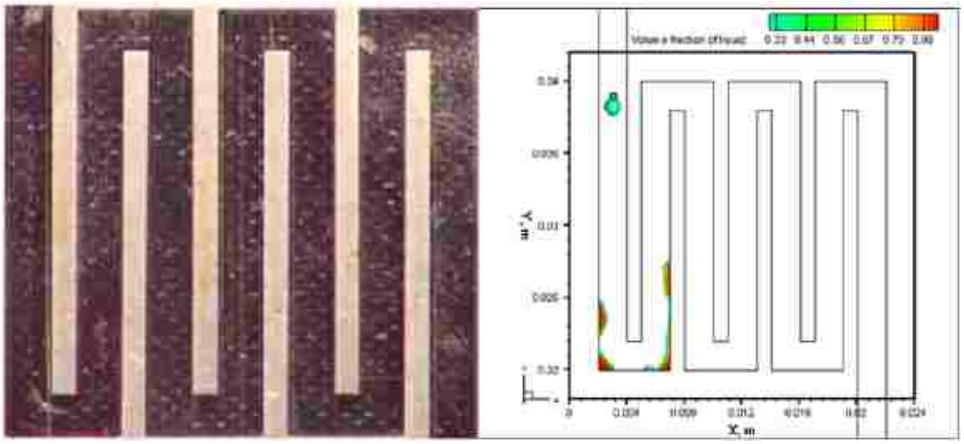

Figure 7.7b: Visualization of liquid motion in the channel at t = 0.067 s

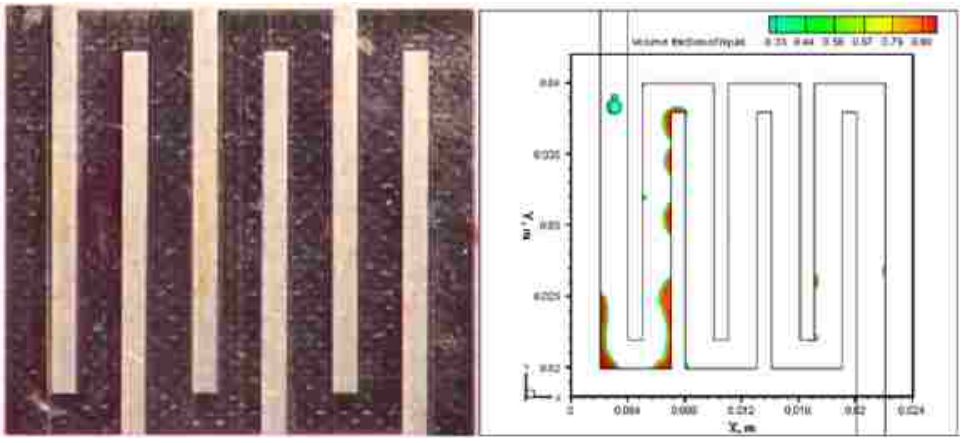

Figure 7.7c: Visualization of liquid motion in the channel at t = 0.133 s

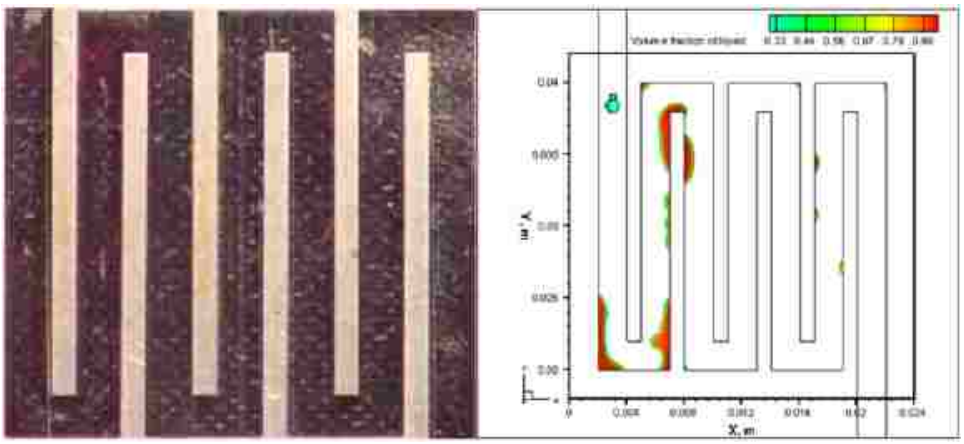

Figure 7.7d: Visualization of liquid motion in the channel at t = 0.2 s

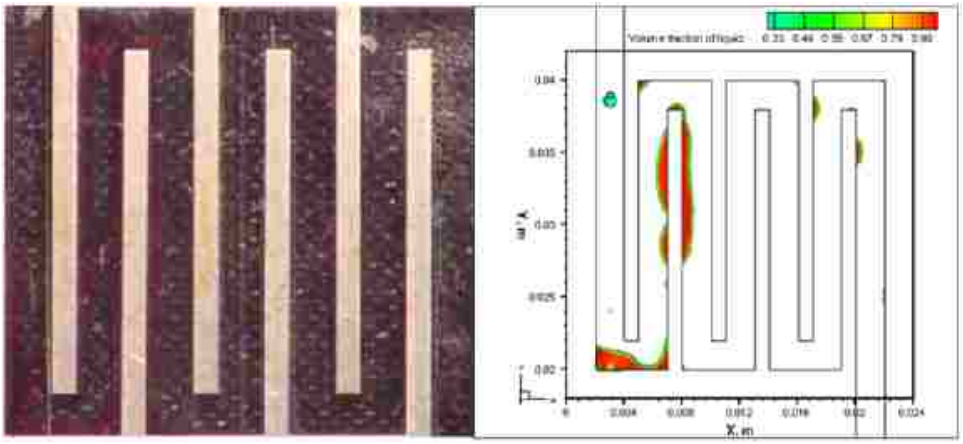

Figure 7.7e: Visualization of liquid motion in the channel at t = 0.267 s

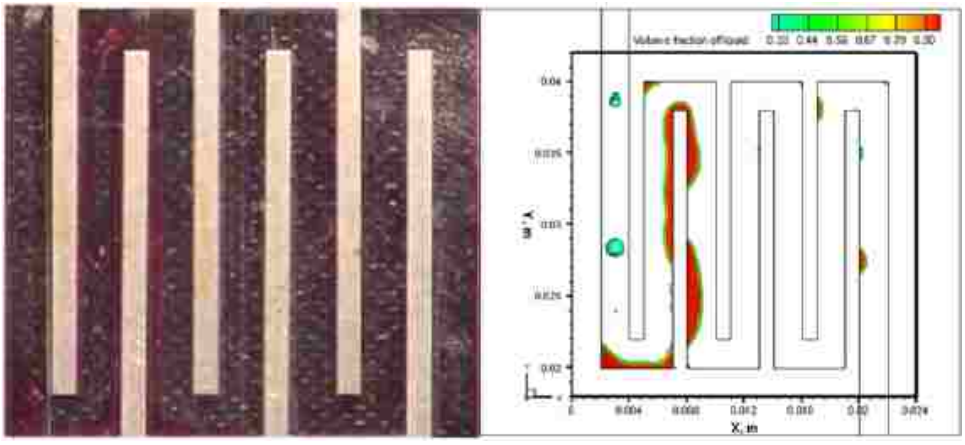

Figure 7.7f: Visualization of liquid motion in the channel at t = 0.333 s

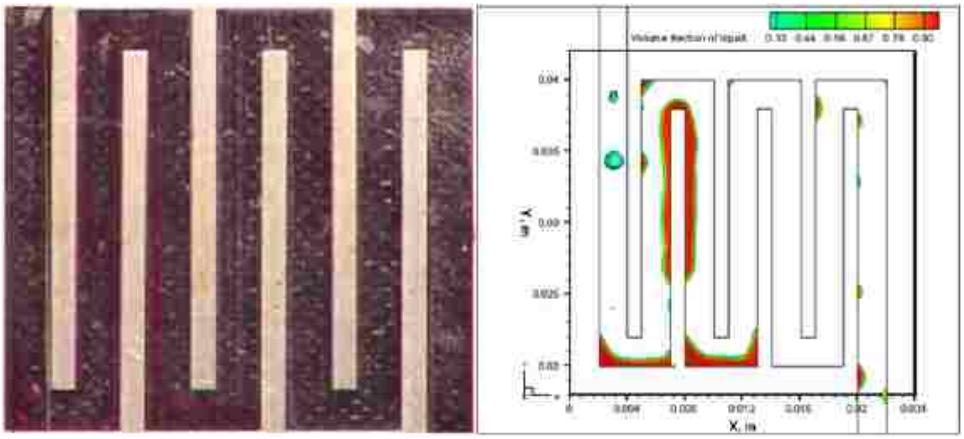

Figure 7.7g: Visualization of liquid motion in the channel at t = 0.4 s

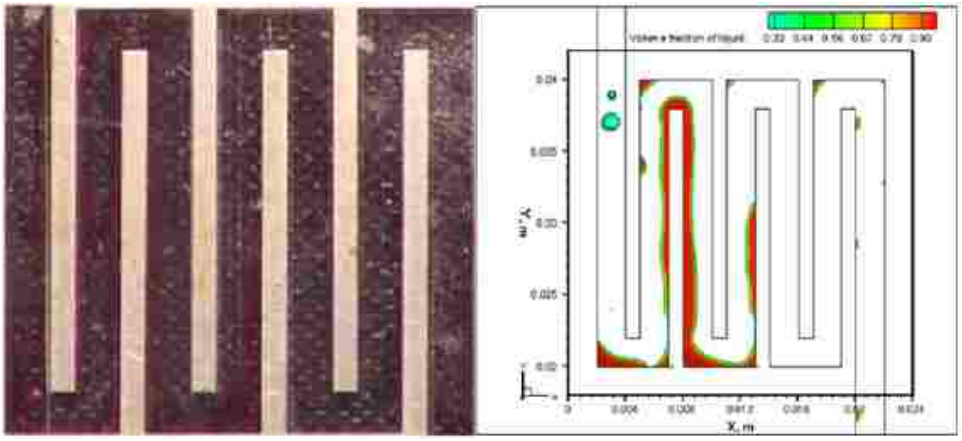

Figure 7.7h: Visualization of liquid motion in the channel at t = 0.467 s

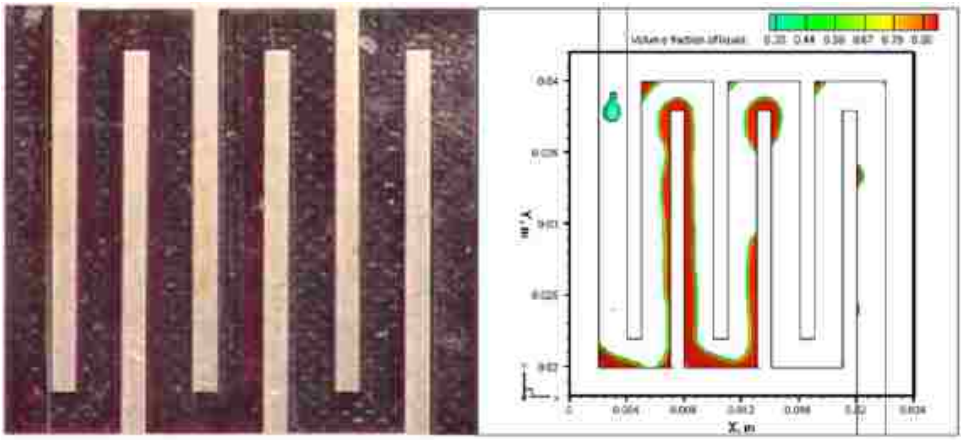

Figure 7.7i: Visualization of liquid motion in the channel at t = 0.533 s

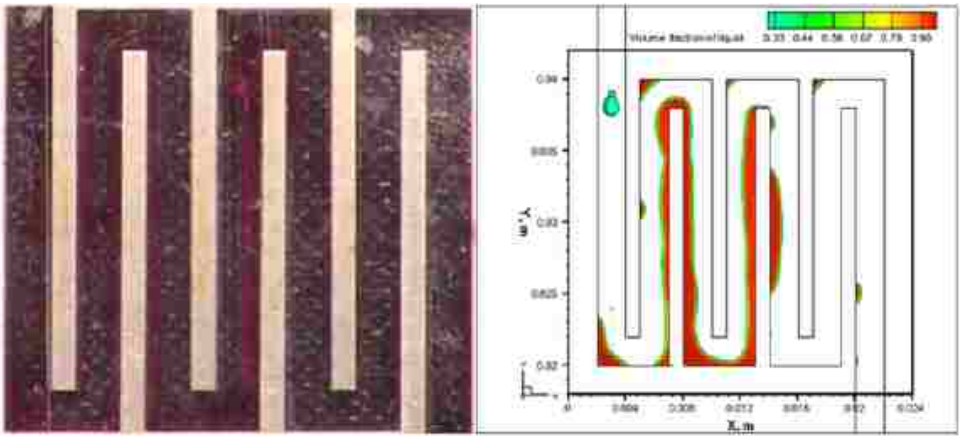

Figure 7.7j: Visualization of liquid motion in the channel at t = 0.6 s

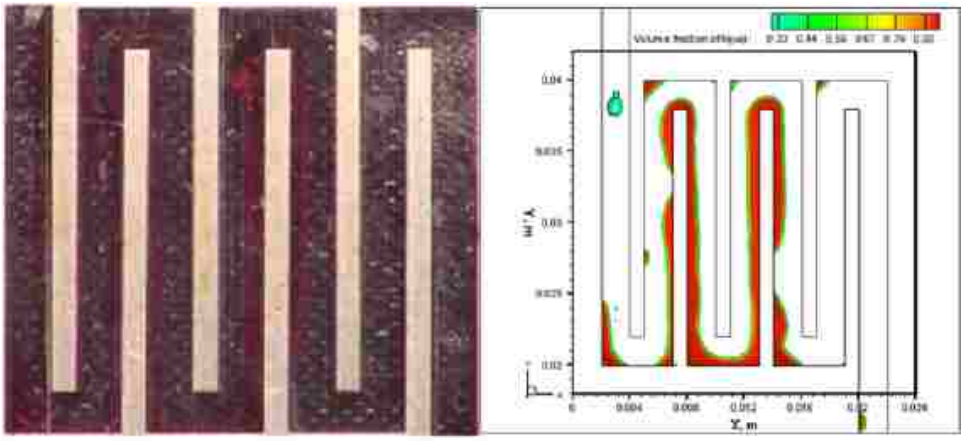

Figure 7.7k: Visualization of liquid motion in the channel at t = 0.667 s

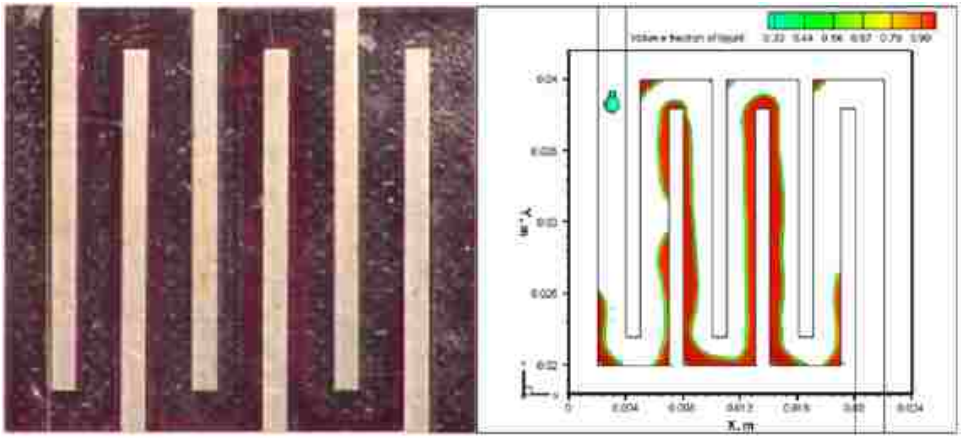

Figure 7.7l: Visualization of liquid motion in the channel at t = 0.733 s

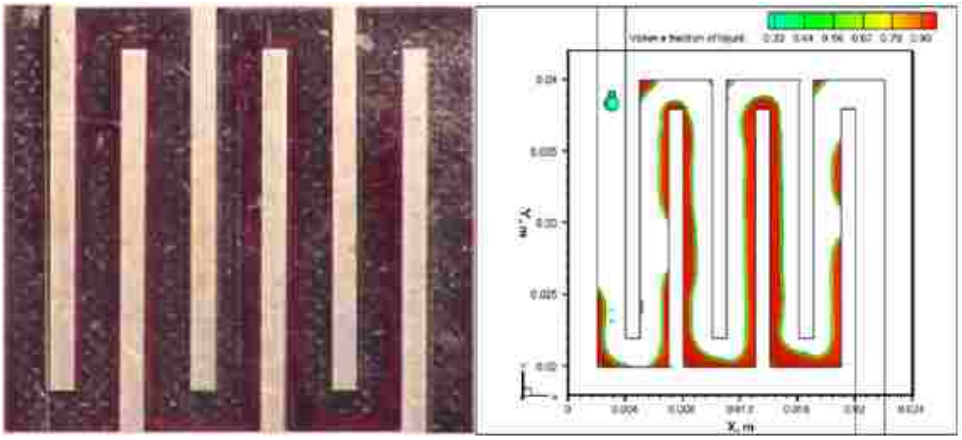

Figure 7.7m: Visualization of liquid motion in the channel at t = 0.8 s

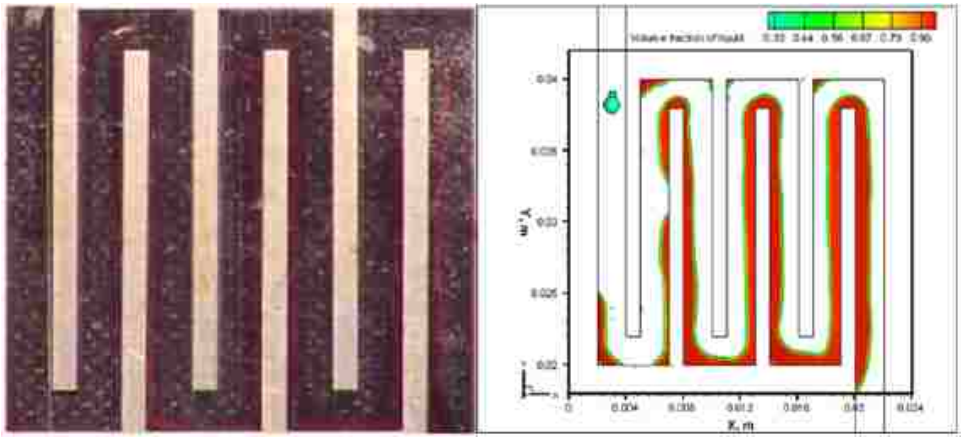

Figure 7.7n: Visualization of liquid motion in the channel at t = 0.867 s

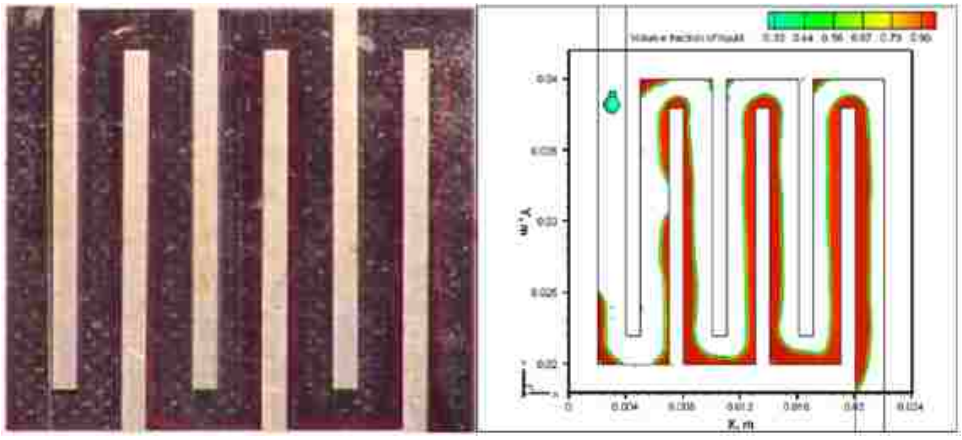

Figure 7.7o: Visualization of liquid motion in the channel at t = 0.933 s

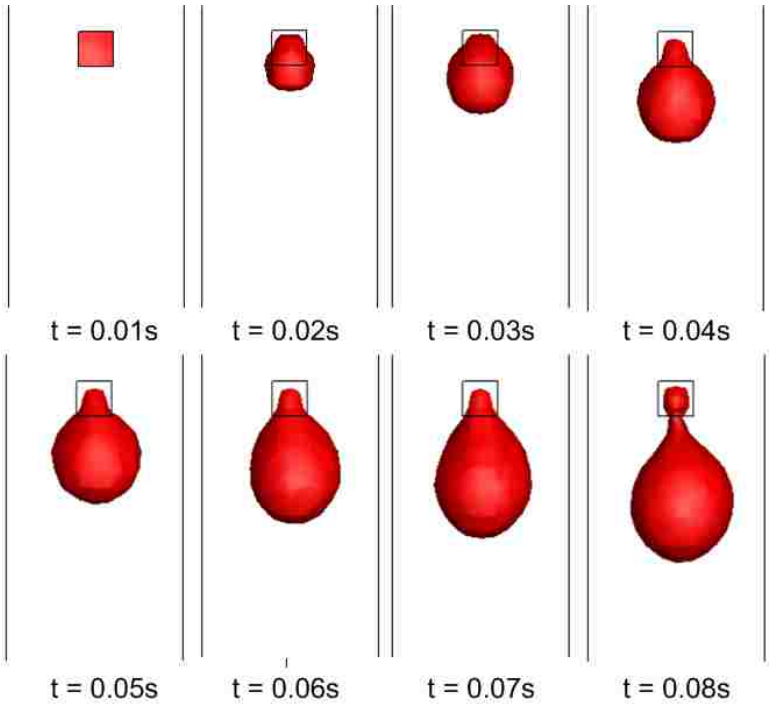


Figure 7.8: Development of pendant droplet in the channel

$$\mathrm{Bo} = \frac{(1000-1)\times 9.81\times 0.0007^2}{0.072} = 0.067 \tag{7.6}$$

Obviously, based on Weber and Bond numbers, it can be concluded that the droplet shape is mainly governed by inertia force rather than surface tension force in Y direction. Note that, the effect of gravity force can only be considered in Z direction (normal to X-Y plane).

Under shear stress from the air flow, the droplet are deformed and then detached from the needle point. It moves along the air flow direction and hit the wall at the channel turn due to its inertia. After hitting the wall, as can be seen in Figure 7.9, liquid interfaces in contact with the solid wall tend to spread in the corners between two different solid walls (sidewall and top wall - the transparent glass, or sidewall and bottom surface MEA). It is noticeable that the contact angles of different walls are different and the shape of droplet is dependent on the values of these contact angles. This phenomenon is also considered as Concus Finn relation described in [93]: the liquid droplet tends to spread in the corner when the contact angles of the surfaces are small (hydrophilic materials) and it tends to be spherical without wetting the tip of the corner when the contact angles of the surfaces are large (hydrophobic materials). Since liquid droplets are continuously provided from the needle into the channel, the stretched liquid is formed along the channel as in Figure 7.9 from $t = 0.1s$ to $t = 0.8s$. The formation of shape of droplet in the channel here can be explained by several factors: the inertia force due to the air flow moving along the channel, the contact angles of the walls formed the channel and the geometry of the channel. If the shear stress is caused by a strong air flow,

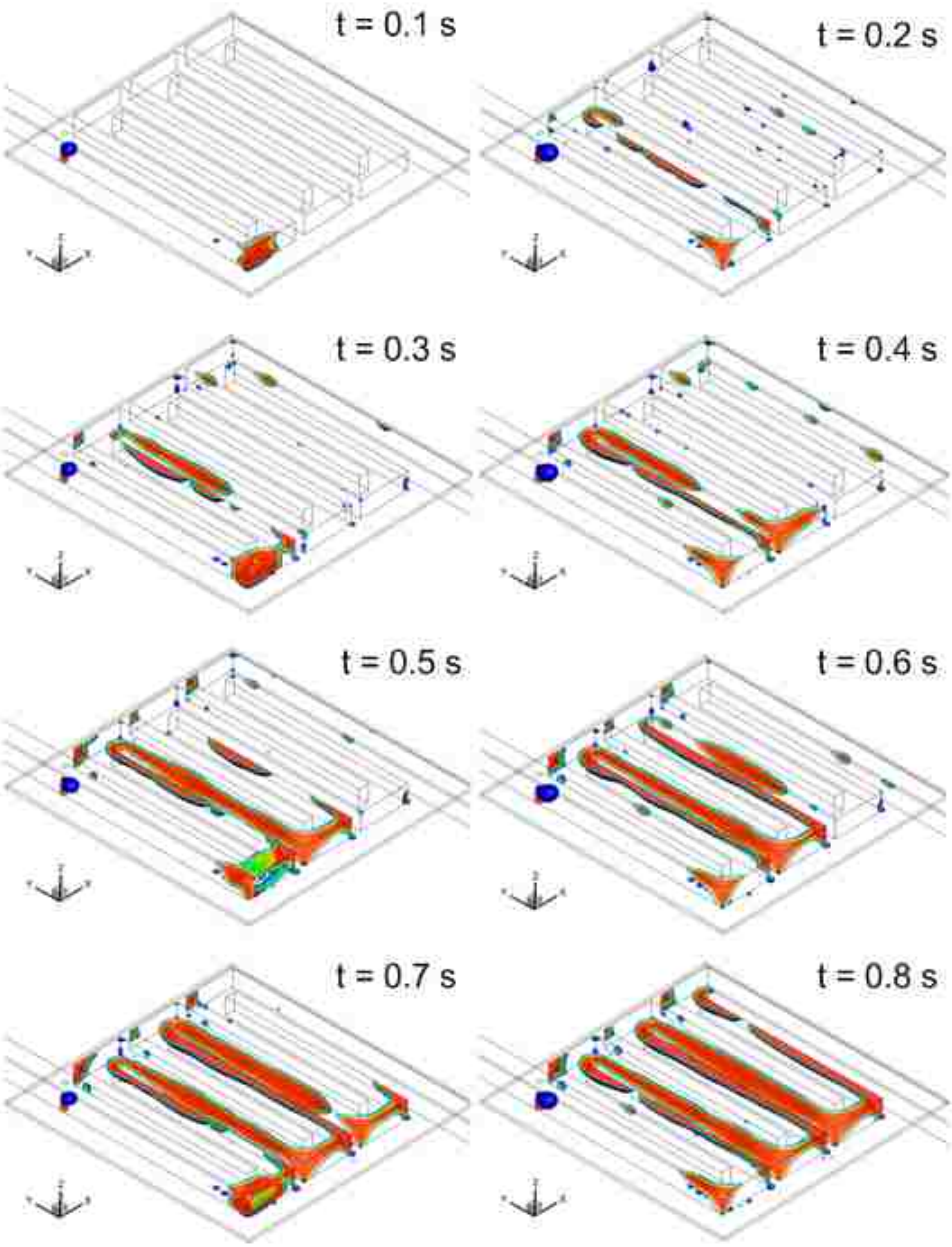


Figure 7.9a: Development of flattened droplet in the channel (From top view)

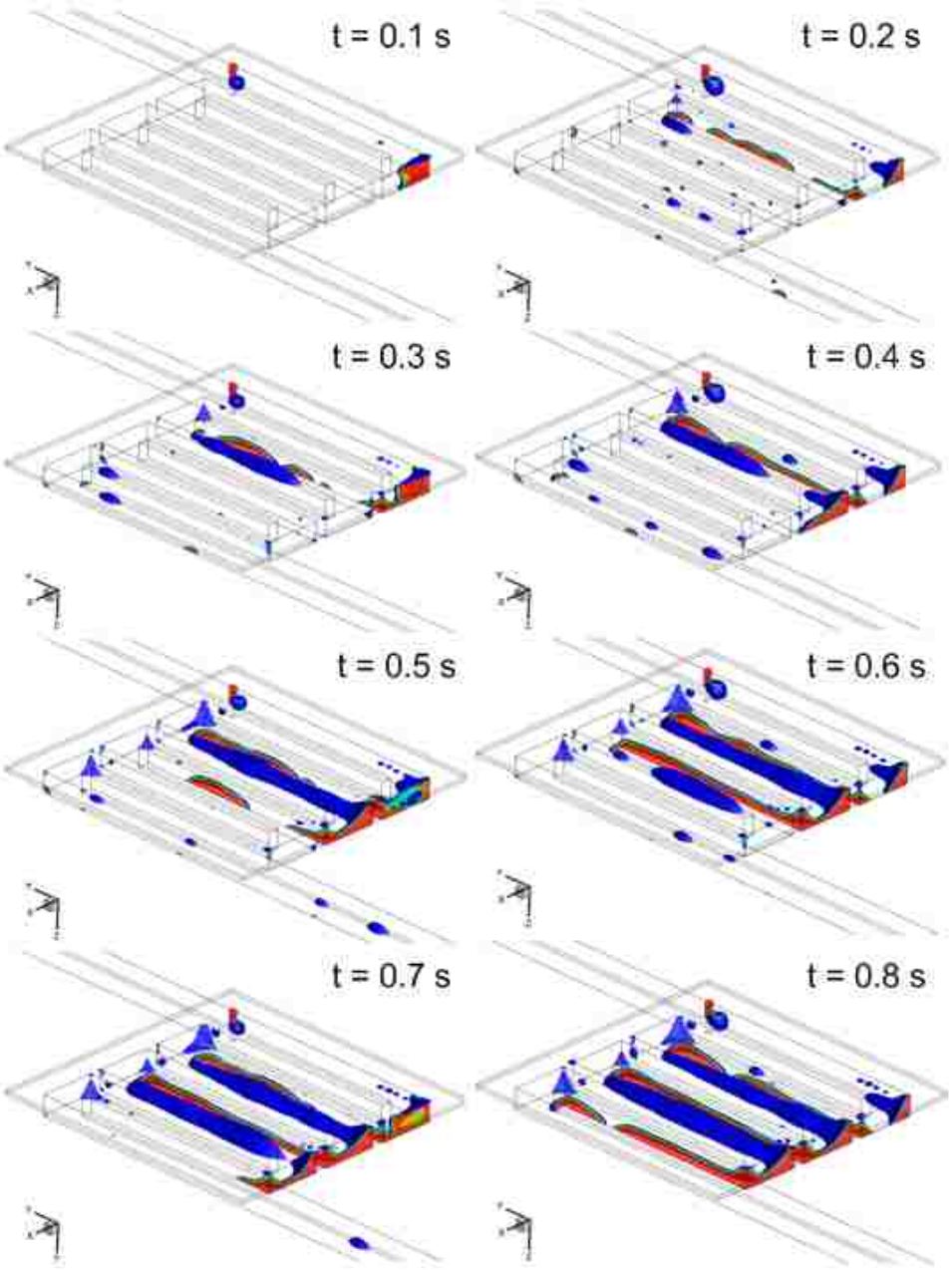


Figure 7.9b: Development of flattened droplet in the channel (From bottom view)

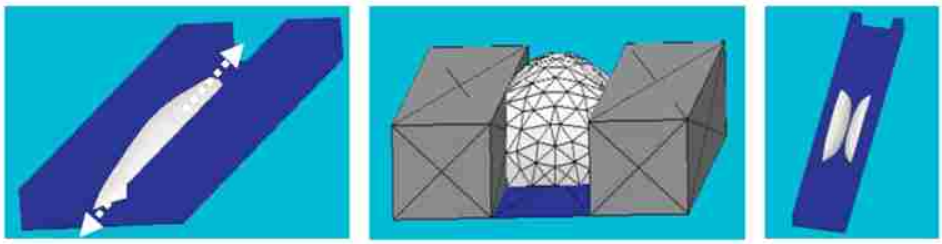

Figure 7.10: Different morphologies of liquid: filament, droplet and stretched droplet (from left to right) (Source from: [93])

the liquid droplet tends to be flattened more widely. The second factor is contact angle and follows Concus Finn relation; one of three morphologies including filament, wedges and droplet as shown in Figure 7.10 is formed depending on the contact angle. If the contact angles are smaller than 45°, the filaments are obtained and if those are larger than 45°, the stretched droplets or droplets are formed. It can be observed in Figure 7.9 that the filaments almost occur in the corner between the up-wall (transparent glass) with contact angle of 43° and the side-wall (stainless stain plate) with contact angle of 53°.

A minor effect realized from the numerical results is the accumulation of liquid water in the corner of the turn where the air flow is weak and it was already explained in the previous chapters. Coming back to the Figure 7.7b, this effect can be observed in the both experimental and numerical results.

**Qualitative comparison between the numerical and experimental models by evaluating the pressure drop in the channel**

The qualitative evaluation of the presence of liquid water effect on the flow and pressure field has been done in Chapter 4 to 6 according to the numerical model results. In this section, the quantitative comparison of this effect is conducted by validating both the numerical and experimental results. Figure 7.11 shows the values of pressure drop in the channel in 1 second when the liquid drops are continuously injected into the channel. The pressure drop indicates the difference between inlet and outlet channel pressures. It can be seen that the values of pressure drop increases as the time progresses while there are more and more liquid droplets occurring in the channel. Although liquid water is continuously added into the channel by setting constant liquid flow rate in the syringe, the appearance of liquid droplets at the needle point is not constant. Recall that liquid water does not stream out of the needle point to the channel, liquid droplets are formed instead: a liquid droplet is formed, gradually grows up and it is taken away due to the shear force from the air flow. After that, another droplet is formed and continues moving. Obviously, this process is discontinued. As a droplet is formed, it makes the pressure drop increased and as it is removed, the pressure drop decreases. This leads to the pressure oscillation as observed in Figure 7.11. The difference of pressure drop within a second is also similar in terms of magnitude order in both numerical and experimental results. However, one can see that the pressure value scale indicated in the experimental pressure transducer is higher than that indicated in the numerical simulation. It is due to the fact that the position of pressure sensor in the experiment is not the

same with the position of inlet pressure calculation in the numerical model. In fact, it is necessary to take into account the pressure drop in the manifold, the connected hose to the fuel cell inlet and the extra channel that are used to connect the experimental fuel cell to the fuel cell test band. The pressure drops in the manifold, the connected hose and extra channel are calculated by using Darcy formulation [92] for the laminar flow

$$\Delta P_L = f\frac{L}{D}\frac{\rho V_{avg}^2}{2} \tag{7.7}$$

For the manifold,

$$\Delta P_1 = \frac{64}{\mathrm{Re}}\frac{L}{D}\frac{\rho V_{avg}^2}{2} = \frac{64}{562.5}\frac{0.1}{0.002}\frac{1.125\times 5.2^2}{2} = 86.5\mathrm{Pa} \tag{7.8}$$

For the extra channel,

$$\Delta P_2 = \frac{57}{\mathrm{Re}}\frac{L}{D}\frac{\rho V_{avg}^2}{2} = \frac{57}{562.5}\frac{0.07}{0.0018}\frac{1.125\times 5.2^2}{2} = 60\mathrm{Pa} \tag{7.9}$$

For the connected hose, the pressure drop is measured at 20 Pa. Thus, the total pressure drop due to connection is approximately 167 Pa. Subtracting this pressure drop from the pressure drop measured in the experiment via the pressure transducer, we have the real number of pressure drop in the channel in the experiment. Figure 7.11 show that the scale of this pressure drop is very similar to the one obtained from the numerical results.

## 7.4 Conclusions

In this chapter, the experimental visualization of droplet motion in the cathode channel is developed to validate the numerical simulation of VOF model and investigate the physics of liquid droplets and its behavior in a PEMFC. The experimental devices and setup including a transparent PEMFC, liquid injection system, optical camera and light source are installed to observe the liquid motion in the channel in a short time period. The experimental data then will be analyzed and compared with the numerical simulation results. In both the experimental and numerical model setup, the geometrical dimension, material properties and operating conditions are set to be the same for the comparison between the experimental and numerical results. It is shown that the results obtained in both numerical model and experiments are in good agreement in terms of the shape of droplet and location of the droplet at a certain instant during operation. Moreover, the physics of droplet and liquid water transport mechanism in the fuel cell channel are also investigated.

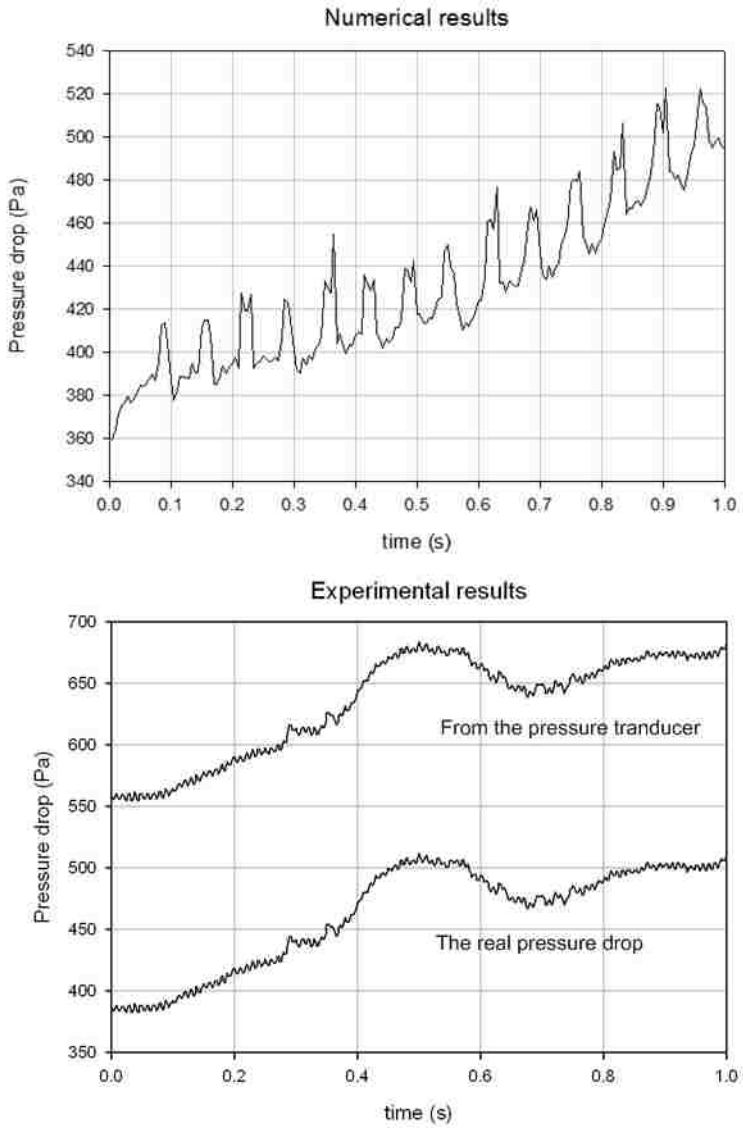


Figure 7.11: Comparison of pressure drop in the channel under the presence of liquid water

# Chapter 8

# Concluding Remarks

## 8.1 Summary of the Dissertation

The main objective of the work presented in this dissertation is to develop a three-dimensional, unsteady, multi-phase, multi-components numerical model incorporated with VOF interface tracking that is capable of addressing the water liquid transport and investigating the water management in PEMFCs. The critical issues of tracking the liquid water, effects of liquid water on physical and transport properties, phase change effect, water flooding phenomenon in a PEMFC have been addressed. The strategies and methodology of model development to figure out these issues also have been developed and validated. The main conclusions can be derived as follows:

In Chapter 4, the motion of water droplets in the channels and porous media of a single interdigitated PEMFC has been investigated to give a good understanding of liquid water transport including deformation, coalescence and detachment processes. In this case, to initialize a large amount of liquid water from the beginning of operation, a series of droplets are added into the channel. The numerical results show that the model is capable of predicting liquid water transport and investigating liquid water effects on the fuel cell performance. Liquid water removal is feasible in the channel and porous media. The presence of liquid water results in an uneven flow field and species concentration distributions in the fuel cell. By visualizing the liquid droplets appearance in the flow regions, it can be observed that the droplets block the mass transport of gas species, resulting in a degradation of local current density and thus severely affecting the fuel cell performance once the flooding is significant.

In Chapter 5, the formation, motion and removal of liquid water has been numerically visualized in a 3-D mathematical PEMFC model by using VOF method incorporated with phase change process. Unlike the case presented in Chapter 4 that liquid droplets are added into the channel at the beginning time, the liquid water presence in this case is automatically determined by phase change condition. Hence, the overview pictures of water liquid transport in a real-time operation in the first 10 seconds of the PEMFC are described as in the following stages: the formation, growth and removal of the water liquid in the channels and porous media. It is shown that the removal of liquid water from the GDLs to the channel is due to convection of the flow field

in the porous media. The removal of liquid in the porous media is much slower and more difficult than that in the flow channels. The liquid amount in the cathode channel goes up and down after its linear increment because there are repeated accumulation and removal of the liquid water in the channel: liquid water accumulation due to condensation and liquid water removal due to convection. It can be seen that the presence of liquid water blocks the mass transport of reactant gas, resulting in a decrease of current density as described in the case of Chapter 4. The model simulation of this case also suggests that the phase change rate is an important factor to investigate the characteristic and mechanism of phase change and liquid water transport in PEMFCs.

Chapter 6 proposes the application of the numerical model in a fuel cell stack. It indicates that the numerical model not only can be used for single PEMFCs but also are available to simulate a fuel cell stack with multi-single cells connected. Compared to the single cell, modeling fuel cell stack is more realistic. Again, the numerical results show that physical parameters such as flow field, species concentrations, temperature, voltage and current density distribution in all single cells of the stack under various operating conditions and/or design parameters can be predicted based on the VOF model. More importantly, by setting liquid droplets in a certain cell of the stack, the flooding is locally created and the degradation of the single cell is investigated to examine the influence of a single cell performance on the whole stack performance.

An experimental visualization of droplet motion in the channel is performed in Chapter 7 to validate the numerical simulation of VOF model. In both the experiment and numerical simulation setup, the geometrical dimension, material properties and operating conditions are set to be the same for the comparison between the experimental and numerical results. It is shown that the results obtained in both numerical model and experiments are in good agreement in terms of the shape of droplet and location of the droplet at a certain instant during operation. Moreover, the physics of droplet and its mechanism are also discussed in several aspects.

## 8.2 Future work

One of the shortcomings in the numerical simulation with VOF algorithm is that it is computationally expensive. From our experience, it takes several weeks to simulate a real-time operation of a single PEMFC with hundred thousand computational cells only in few seconds of flow time when running the simulation in a single core of an Intel Quad-core 2.01 GHz PC. The running time should take much longer if the computational domain is larger (for example: fuel cell stack with more than ten single cells), the grid is fined (then increasing the number of computational cells in the domain) and/or the flow time is longer (doing simulation in minutes). In order to increase the speed of calculation processing and save the running time, the code for parallel running algorithm will be implemented and improved. This will be beneficial for the application of the numerical model to Fuel Cell R&D in practice.

Since the parallel programming is implemented, the next applications of numerical model are investigation on the PEFMC performance with different designs and various operating conditions of fuel cell. When the computational speed is significantly increased, running the model simulation for long periods of time will be necessary to examine liquid behavior and flooding phenomenon in a PEMFC up to several hours of

computational time. In addition, the fuel cell stack models with large dimension and complex geometry will also be simulated.

A potential future direction for experimental visualization of droplet motion in the channel will to investigate the droplet behavior in micro channels. Actually, it is one of research aspects in microfluidics. However, the injection of liquid droplet into the channel by manipulation may not be very accuracy due to the uncertainty of experiment. In addition, capturing the droplet motion conducted by a commercial camera with a low frame rate at 30 frames per second is not sufficient enough to examine the physics of droplet in very small time intervals of $\mu$s. In order to increase the accuracy and time resolution of the experiment, the micro-syringe pump and high-speed camera will be in consideration in our future work. Furthermore, we will focus on analyzing the physics of droplet in the fuel cell channel with more details since the high resolution of the camera and high accuracy of the experimental devices are obtained.

# Bibliography


[1] International energy outlook, Energy Information Administration, U.S. Department of Energy, 2009.

[2] T. E. Drennen, J. E. Rosthal, Pathways to a hydrogen future, Elsevier, 2007.

[3] Hydrogen energy and fuel cells - A vision of our future, European commission, 2003.

[4] L. O. Vasquez, Fuel Cell Research Trends, Nova Science Publishers Inc., 2007.

[5] Matthew. M. Mench, Fuel Cell Engines, John Willey & Sons, 2008.

[6] A. Z. Weber, J. Newman, Modeling Transport in Polymer-Electrolyte Fuel Cells, Chemical Reviews 104(10) (2004), pp. 4679-4726.

[7] T. E. Springer, T. A. Zawodzinski, S. Gottesfeld, Polymer Electrolyte Fuel Cell Model, Journal of the Electrochemical Society 138(8) (1991), pp. 2334-2342.

[8] D. M. Bernardi, M. V. Verbrugge, A Mathematical Modeling of the Solid-Polymer-Electrolyte Fuel Cell, Journal of the Electrochemical Society 139 (9) (1992), pp. 2477-2491.

[9] T. V. Nguyen, R. E. White, A Heat and Water Management Model for Proton-Exchange-Membrane Fuel Cells, Journal of Electrochemical Society 140(8) (1993), pp. 2178-2186.

[10] J. J. Baschuk, Xianguo Li, Modeling of polymer electrolyte membrane fuel cells with variable degrees of water flooding, Journal of Power Sources 86 (2000) 181-196.

[11] W. Huang, B. Zhou, A. Sobiesiak, Steady and Unsteady Modeling of Single PEMFC with Detailed Thermo-Electro-Chemical Model, Journal of the Electrochemical Society 153(10) (2006), pp. A1945-A1954.

[12] D. S. Falcao, V. B. Oliveira, C. M. Rangel, C. Pinho, A. M. F. R. Pinto, Water transport through a PEM fuel cell: A one-dimensional model with heat transfer effects, Chemical Engineering Science 64 (2009), pp. 2216-2225.

[13] J. H. Nam, M. Kaviany, Effective diffusivity and water-saturation distribution in single- and two-layer PEMFC diffusion medium, International Journal of Heat and Mass Transfer 46 (2003), pp. 4595-4611.

[14] V. Gurau, H. Liu, S. Kakac, Two-dimensional Model for Proton Exchange Membrane Fuel Cells, AIChE Journal 44(11) (1998), pp.2410 2422.

[15] D. Singh, D. M. Lu, N. Djilali, A two-dimensional analysis of mass transport in proton exchange membrane fuel cells, International Journal of Engineering Science 37 (1999), pp.431-452.

[16] I. M. Hsing, P. Futerko, Two-dimensional simulation of water transport in polymer electrolyte fuel cells, Chemical Engineering Science 55 (2000), pp. 4209-4218.

[17] Z.H Wang, C.Y. Wang, K.S. Chen, Two-phase flow and transport in the air cathode of proton exchange membrane fuel cells, Journal of Power Sources 94 (2001), pp. 40-50.

[18] Z. Liu, Z. Mao, C. Wang, A two dimensional partial flooding model for PEMFC, Journal of Power Sources 158 (2006), pp. 1229-1239.

[19] K. T. Jeng, C. Y. Wen, L. D . Anh, A study on mass transfer in the cathode gas channel of a proton exchange membrane fuel cell, Journal of Mechanics 23(4) (2007), pp. 223-232.

[20] L. You, H. Liu, A two-phase flow and transport model for the cathode of PEMF fuel cells, International Journal of Heat and Mass Transfer 45 (2002), pp. 2277-2287.

[21] M. K. Baboli, M. J. Kermani, A two-dimensional, transient, compressible isothermal and two-phase model for the air-side electrode of PEM fuel cells, Electrochimica Acta 53 (2008), pp. 7644-7654.

[22] S. Dutta, S. Shimpalee, J. W. Van Zee, Three-dimensional simulation of straight channel PEM fuel cells, Journal of Applied Electrochemistry 30 (2000), pp.135-146.

[23] S. Dutta, S. Shimpalee, J. W. Van Zee, Numerical prediction of mass-exchange between cathode and anode channels in a PEM fuel cell, International Journal of Heat and Mass Transfer 44 (2001), pp. 2029-2042.

[24] H. Ju, H. Meng, C. Y. Wang, A single-phase, non-isothermal model for PEM fuel cells, International Journal of Heat and Mass Transfer 48 (2005), pp. 1303-1315.

[25] S. Um, C.Y. Wang, K.S. Chen, Computational fluid dynamics modeling of proton exchange membrane fuel cells, Journal of Electrochemical Society 147 (2004), pp.44854493.

[26] S. Um, C.Y. Wang, Computational study of water transport in proton exchange membrane fuel cells, Journal of Power Sources 156 (2006), pp.211-223.

[27] C. Y. Wang, P. Cheng, A multiphase mixture model for multiphase, multi-component transport in capillary porous media I: model development, International Journal of Heat Mass Transfer 39 (1996), pp. 36073618.

[28] Y. Wang, S. Basu, C. Y. Wang, Modeling two-phase flow in PEM fuel cell channels, Journal of Power Sources 179 (2008), pp. 603-617.

[29] S. Basu, J. Li, C. Y. Wang, Two-phase flow and maldistribution in gas channels of a polymer electrolyte fuel cell, Journal of Power Sources 187 (2009), pp. 431-443.

[30] S. Mazumder, J. V. Cole, Rigorous 3-D Mathematical Modeling of PEM Fuel Cells II. Model Predictions with Liquid Water Transport, Journal of the Electrochemical Society 150(11) 2003, pp. A1510-A1517.

[31] H. Ju, Analyzing the effects of immobile liquid saturation and spatial wettability variation on liquid water transport in diffusion media of polymer electrolyte fuel cells (PEFCs), Journal of Power Sources 185 (2008), pp. 55-62.

[32] T. Berning, N. Djilali, A 3D, Multiphase, Multicomponent Model of the Cathode and Anode of a PEM Fuel Cell, Journal of the Electrochemical Society 150(12) 2003, pp. A1589-A1598.

[33] Q. Ye, T. V. Nguyen, Three-Dimensional Simulation of Liquid Water Distribution in a PEMFC with Experimentally Measured Capillary Functions, Journal of the Electrochemical Society 154(12) 2007, pp. B1242-B1251.

[34] G. He, P. Ming, Z. Zhao, A. Abudula, Y. Xiao, A two-phase fluid model for two-phase flow in PEMFCs, Journal of Power Sources 163 (2007), pp. 864-873.

[35] T. Berning, A Three-Dimensional, Two-Fluid Model of PEM Fuel Cell Cathodes, ECS Transactions 16(2) (2008), pp. 23-34.

[36] V. Gurau, T. A. Zawodzinski, J. A. Mann, Two-phase Transport in PEM Fuel Cell Cathodes, Journal of Fuel Cell Science and Technology 5 021009-1 (2008).

[37] P. Quan, B. Zhou, A. Sobiesiak, Z. Liu , Water Behavior in Serpentine Micro-channel for Proton Exchange Membrane Fuel Cell Cathode, Journal of Power Sources 152 (2005), pp. 131-145.

[38] K. Jiao, B. Zhou, P. Quan, Liquid Water Transport in Parallel Serpentine Channels with Manifolds on Cathode Side of a PEM Fuel Cell Stack, Journal of Power Sources 154 (2006), pp. 124-137.

[39] K. Jiao, B. Zhou, P. Quan , Liquid Water Transport in Straight Micro-Parallel-Channels with Manifolds for PEM Fuel Cell Cathode, Journal of Power Sources 157 (2006), pp. 226-243.

[40] K. Jiao, B. Zhou, Innovative Gas Diffusion Layers and Their Water Removal Characteristics in PEM Fuel Cell Cathode, Journal of Power Sources 169 (2007), pp. 296314.

[41] K. Jiao, B. Zhou, Effects of electrode wettabilities on liquid water behaviours in PEM fuel cell cathode, Journal of Power Sources 175 (2008), pp. 106119.

[42] X. Zhu, P.C. Sui, N. Djilali, Dynamic behaviour of liquid water emerging from a GDL pore into a PEMFC gas flow channel, Journal of Power Sources 172 (2007), pp. 287-295.

[43] Zhu, X., P. C. Sui, N. Djilali, Numerical Simulation of Emergence of a Water Droplet from a Pore into a Microchannel Gas Stream, Microfluidics & Nanofluidics 4(6) (2008), pp. 1613.

[44] Zhu, X., P. C. Sui, N. Djilali, Three Dimensional Numerical Simulations of Water Droplet Dynamics in a PEMFC Gas Channel, Journal of Power Sources 181 (2008), pp. 101-115.

[45] Z. Zhan, J. Xiao, M. Pan, R. Yuan, Characteristics of droplet and film water motion in the flow channels of polymer electrolyte membrane fuel cells, Journal of Power Sources 160 (2006), pp. 1-9.

[46] Y. H. Cai, J. Hu, H. P. Ma, B. L. Yi, H. M. Zhang, Effects of hydrophilic/hydrophobic properties on the water behavior in the micro-channels of a proton exchange membrane fuel cell, Journal of Power Sources 161 (2006), pp. 843-848.

[47] A. Golpaygan, N. Ashgriz, Multiphase flow model to study channel flow dynamics of PEM fuel cells: deformation and detachment of water droplets, International Journal of Computation Fluid Dynamics 22 (2008), pp. 85-95.

[48] A. D. Le, B. Zhou, A General Model of Proton Exchange Membrane Fuel Cell, Journal of Power Sources 182 (2008), pp. 197222.

[49] A. D. Le, B. Zhou, Fundamental Understanding of Liquid Water Effects on the Performance of a PEMFC with Serpentine-Parallel Channels, Electrochimica Acta 54 (2009), pp. 2137-2154.

[50] A. D. Le, B. Zhou, A generalized numerical model for liquid water in a PEMFC with interdigitated design, Journal of Power Sources 193 (2009), pp. 665-683.

[51] A. D. Le, B. Zhou, Real-time numerical simulation of liquid water formation and transport in an operating Proton Exchange Membrane Fuel Cell, International Journal of Hydrogen Energy, submitted in 2009.

[52] A. Bazylak, Liquid water visualization in PEM fuel cells: A review, International Journal of Hydrogen Energy 34 (2009), pp. 3845-3857.

[53] K. Tuber, D. Pocza, C. Hebling, Visualization of Water Buildup in the Cathode of a Transparent PEM Fuel Cell, Journal of Power Sources 124 (2003), pp. 403-414.

[54] Z. Liu, Z. Mao, C. Wang, A two dimensional partial flooding model for PEMFC, Journal of Power Sources 158 (2006), pp. 1229-1239.

[55] D. Spernjak, A. K. Prasad, S. G. Advani, Experimental investigation of liquid water formation and transport in a transparent single-serpentine PEM fuel cell, Journal of Power Sources 170 (2007), pp. 334-344.

[56] S. Ge, C. Y. Wang, Liquid Water Formation and Transport in the PEFC anode, Journal of the Electrochemical Society 154(10) 2007, pp. B998-B1005.

[57] E. Kimball, T. Whitaker, Y. G. Kevrekidis, J. B. Benziger, Drops, Slugs, and Flooding in Polymer Electrolyte Membrane Fuel Cells, AIChE J. 54(5) (2008), pp.1313-1332.

[58] D. Spernjak, S. G. Advani, A. K. Prasad, Simultaneous Neutron and Optical Imaging in PEM Fuel Cells, Journal of the Electrochemical Society 156(1) (2009), pp. B109-B117.

[59] B. Gao, T. S. Steenhuisa, Y. Zevi, J. Y. Parlangea, R. N. Carter, T. A. Trabold, Visualization of unstable water flow in a fuel cell gas diffusion layer, Journal of Power Sources 190 (2009), pp. 493-498.

[60] T.A. Trabold, J.P. Owejan, D.L. Jacobson, M. Arif, P.R. Huffman, In situ investigation of water transport in an operating PEM fuel cell using neutron radiography: Part 1 Experimental method and serpentine flow field results, International Journal of Heat and Mass Transfer 49 (2006), pp. 4712-4720.

[61] J.P. Owejan, T.A. Trabold, D.L. Jacobson, D.R. Baker, D.S. Hussey, M. Arif, In situ investigation of water transport in an operating PEM fuel cell using neutron radiography: Part 2 Transient water accumulation in an interdigitated cathode flow field, International Journal of Heat and Mass Transfer 49 (2006), pp. 4721-4731.

[62] I. Manke, Ch. Hartnig, M. Grnerbel, J. Kaczerowski, W. Lehnert, N. Kardjilov, A. Hilger, J. Banhart, W. Treimer, M. Strobl, Quasi-in situ neutron tomography on polymer electrolyte membrane fuel cell stacks, Applied Physics Letters 90 184101 (2007).

[63] M. A. Hickner, N. P. Siegel, K. S. Chen, D. N. McBrayer, D. S. Hussey, D. L. Jacobson, and M. Arif, Real-Time Imaging of Liquid Water in an Operating Proton Exchange Membrane Fuel Cell, Journal of the Electrochemical Society 153 (2006), pp. A902-A908.

[64] M. A. Hickner, N. P. Siegel, K. S. Chen, D. S. Hussey, D. L. Jacobson, M. Arif, Understanding Liquid Water Distribution and Removal Phenomena in an Operating PEMFC via Neutron Radiography, Journal of the Electrochemical Society 155 (2008), pp. B294-B302.

[65] M. A. Hickner, N. P. Siegel, K. S. Chen, D. S. Hussey, D. L. Jacobson, M. Arif, In Situ High-Resolution Neutron Radiography of Cross-Sectional Liquid Water Profiles in Proton Exchange Membrane Fuel Cells, Journal of the Electrochemical Society 155(4) (2008), pp. B427-B434.

[66] J. B. Siegel, D. A. McKay, A. G. Stefanopoulou, D. S. Hussey, D. L. Jacobson, Measurement of Liquid Water Accumulation in a PEMFC with Dead-Ended Anode, Journal of the Electrochemical Society 155(11) (2008), pp. B1168-B1178

[67] J. Park, X. Li, D. Tran, T. Abdel-Baset, D.S. Hussey, D.L. Jacobson, M. Arif, Neutron imaging investigation of liquid water distribution in and the performance of a PEM fuel cell, International Journal of Hydrogen Energy 33 (2008), pp. 3373-3384.

[68] C. Hartnig, I. Manke, R. Kuhn, S. Kleinau, J. Goebbels, J. Banhart, High-resolution in-plane investigation of the water evolution and transport in PEM fuel cells, Journal of Power Sources 188 (2009), pp. 468-474.

[69] S. Tsushima , K. Teranishi, S. Hirai, Magnetic Resonance Imaging of the Water Distribution within a Polymer Electrolyte Membrane in Fuel Cells, Electrochemical and Solid-State Letters 7 (2004), pp. A269-A272.

[70] K. R. Minard, V. V. Viswanathan, P. D. Majors, L. Q. Wang, P. C. Rieke, Magnetic resonance imaging (MRI) of PEM dehydration and gas manifold flooding during continuous fuel cell operation, Journal of Power Sources 161 (2006), pp 856-863.

[71] D. Zachary, R. I. Masel, Quantitative MRI study of water distribution during operation of a PEM fuel cell using Teflon flow fields, Journal of Power Sources 171 (2007), pp. 678-687.

[72] J. Bedeta, G. Maranzana, S. Leclerc, O. Lottin, C. Moyne, D. Stemmelen, P. Mutzenhardt, D. Canet, Magnetic resonance imaging of water distribution and production in a 6cm$^2$ PEMFC under operation, International Journal of Hydrogen Energy 33 (2008), pp.3146-3149.

[73] Fluent 6.3 Manual, Fluent Inc. (2006).

[74] Colleen S. Spiegel, Designing and Building Fuel Cells, McGraw-Hill (2007).

[75] R. B. Bird, W. E. Steward, E. N. Lightfoot, Transport Phenomena, John Willey & Sons (1960).

[76] M. M. Mench, Fuel Cell Engines, J. Wiley & Sons (2008).

[77] S. Motupally, A. J. Becker and J. W. Weidner, Diffusion of Water through Nafion 115, Journal of the Electrochemical Society 147 (2000), pp. 3171-3177.

[78] D. B. Kothe, W. J. Rider, S. J. Mosso, J. S. Brock, J. I. Hochstein, Volume Tracking of Interfaces Having Surface Tension in Two and Three Dimensions, AIAA 96-0859.

[79] H. Tang, L. C. Wrobel, Z. Fan, Tracking of immiscible interfaces in multiple-material mixing process, Computational Material Sciences 29 (2004), pp. 103-118.

[80] J. Larminie, A. Dicks, Fuel Cell Systems Explained, 2nd ed., John Wiley & Sons, England (2003).

[81] H. K. Versteeg, W. Malalasekera, An Introduction to Computational Fluid Dynamics, John Wiley & Sons, (1995).

[82] F. Barbir, PEM Fuel Cells: Theory and Practice (Sustainable World Series), Elsevier Inc., (2005).

[83] Y. Shan, S.Y. Choe, and S.H. Choi, Unsteady 2D PEM fuel cell modeling for a stack emphasizing thermal effects, Journal of Power Sources 165 (2007), pp. 196-209.

[84] Z. Liu, Z. Mao, C. Wang, W. Zhuge, Y. Zhang, Numerical simulation of a mini PEMFC stack, Journal of Power Sources 160 (2006), pp. 1111-1121.

[85] C.H. Chen, S.P. Jung and S.C. Yen, Flow distribution in the manifold of PEM fuel cell stack, Journal of Power Sources 173 (2007), pp. 249-263.

[86] R. Mustata, L. Valino, F. Barreras, M. I. Gil, A. Lozano, Study of the distribution of air flow in a proton exchange membrane fuel cell stack, Journal of Power Sources 192 (2009), pp. 185-189.

[87] Y. Zhang, A. Mawardi, and R. Pitchumani, Numerical studies on an air-breathing proton exchange membrane (PEM) fuel cell stack, Journal of Power Sources 173 (2007), pp. 264-276.

[88] S. Shimpalee, M. Ohashi, J.W. Van Zee, C. Ziegler, C. Stoeckmann, C. Sadeler, C. Hebling, Experimental and numerical studies of portable PEMFC stack, Electrochimica Acta 54(10) (2009), pp. 2899-2912.

[89] Jixin Chen, Experimental Study on the Performance of a 10-cell Proton Exchange Membrane (PEM) Fuel Cell stack, Master Thesis, University of Windsor, Ontario, Canada (2007).

[90] J. Chen, B. Zhou, Diagnosis of PEM fuel cell stack dynamic behaviors, Journal of Power Sources 177 (2008), pp. 83-95.

[91] Xiaojing Liu, Liquid water removal process in the PEMFC cathode side, Master Thesis, University of Windsor, Ontario, Canada (2010).

[92] Y. A. Cengel, J. M. Cimbala, Fluid Mechanics - Fundamentals and Applications, 1st ed., McGraw-Hill, 2006.

[93] J. Berthier, Microdrops and Digital Microfluidics , William Andrew, New York, (2008).

# Vita Auctoris

Anh Dinh Le was born in 1980 in Hanoi, Vietnam. He graduated from Hanoi University of Technology in 2002 with a Bachelor of Science degree in Mechanical Engineering. From 2003 he went on to the Da-Yeh University, Taiwan where he obtained a Master of Science in Mechanical Engineering in 2005. Since 2006 he is pursuing a Ph.D. degree in Mechanical Engineering at the University of Windsor and hopes to graduate in Winter 2010.